

THE PROPERTIES AND PREVALENCE OF GALACTIC OUTFLOWS AT $z \sim 1$ IN THE EXTENDED GROTH STRIP¹

KATHERINE A. KORNEI AND ALICE E. SHAPLEY²

Department of Physics and Astronomy, University of California, Los Angeles, CA 90025, USA

CRYSTAL L. MARTIN

Physics Department, University of California, Santa Barbara, CA 93106, USA

ALISON L. COIL³

Center for Astrophysics and Space Sciences, Department of Physics, University of California, San Diego, CA 92093, USA

JENNIFER M. LOTZ

Space Telescope Science Institute, Baltimore, MD 21218, USA

DAVID SCHIMINOVICH

Department of Astronomy, Columbia University, New York, NY 10027, USA

KEVIN BUNDY

Kavli Institute for the Physics and Mathematics of the Universe
Todai Institutes for Advanced Study
University of Tokyo, Kashiwa, Japan 277-8583 (Kavli IPMU, WPI)

KAI G. NOESKE

Space Telescope Science Institute, Baltimore, MD 21218, USA

Draft version September 24, 2018

ABSTRACT

We investigate galactic-scale outflowing winds in 72 star-forming galaxies at $z \sim 1$ in the Extended Groth Strip. Galaxies were selected from the DEEP2 survey and follow-up LRIS spectroscopy was obtained covering Si II, C IV, Fe II, Mg II, and Mg I lines in the rest-frame ultraviolet. Using *GALEX*, *HST*, and *Spitzer* imaging available for the Extended Groth Strip, we examine galaxies on a per-object basis in order to better understand both the prevalence of galactic outflows at $z \sim 1$ and the star-forming and structural properties of objects experiencing outflows. Gas velocities, measured from the centroids of Fe II interstellar absorption lines, are found to span the interval $[-217, +155]$ km s⁻¹. We find that $\sim 40\%$ (10%) of the sample exhibits blueshifted Fe II lines at the 1σ (3σ) level. We also measure maximal outflow velocities using the profiles of the Fe II and Mg II lines; we find that Mg II frequently traces higher velocity gas than Fe II. Using quantitative morphological parameters derived from the *HST* imaging, we find that mergers are not a prerequisite for driving outflows. More face-on galaxies also show stronger winds than highly inclined systems, consistent with the canonical picture of winds emanating perpendicular to galactic disks. In light of clumpy galaxy morphologies, we develop a new physically-motivated technique for estimating areas corresponding to star formation. We use these area measurements in tandem with *GALEX*-derived star-formation rates to calculate star-formation rate surface densities. At least 70% of the sample exceeds a star-formation rate surface density of $0.1 M_{\odot} \text{ yr}^{-1} \text{ kpc}^{-2}$, the threshold necessary for driving an outflow in local starbursts. At the same time, the outflow detection fraction of only 40% in Fe II absorption provides further evidence for an outflow geometry that is not spherically symmetric. We see a $\sim 3\sigma$ trend between outflow velocity and star-formation rate surface density, but no significant trend between outflow velocity and star-formation rate. Higher resolution data are needed in order to test the scaling relations between outflow velocity and both star-formation rate and star-formation rate surface density predicted by theory.

¹ Based, in part, on data obtained at the W.M. Keck Observatory, which is operated as a scientific partnership among the California Institute of Technology, the University of California, and NASA, and was made possible by the generous financial support of the W.M. Keck Foundation.

² Packard Fellow.

³ Alfred P. Sloan Fellow.

1. INTRODUCTION

Far from being closed boxes, galaxies are known to affect their environment by expelling gas and metals into the intergalactic medium (IGM) via “superwinds” (e.g., Heckman et al. 1990; Steidel et al. 1996; Franx et al. 1997; Martin 1999; Pettini et al. 2000, 2001; Shapley et al. 2003; Martin 2005; Veilleux et al. 2005; Rupke et al. 2005; Tremonti et al. 2007; Weiner et al. 2009; Steidel et al. 2010; Coil et al. 2011). These outflows may contribute to the limiting of black hole and spheroid growth (possibly resulting in the correlation between black hole and bulge mass; e.g., Ferrarese & Merritt 2000; Robertson et al. 2006), the enrichment of the IGM (Oppenheimer & Davé 2006), and the regulation of star formation through the ejection of cold gas (Scannapieco et al. 2005; Croton et al. 2006). At high redshifts, winds may have played a critical role in reionization by clearing paths for ionizing radiation to escape from galaxies (Dove et al. 2000; Steidel et al. 2001; Heckman et al. 2001a; Gnedin et al. 2008).

The kinematics of interstellar absorption lines provide one of the key probes of outflowing gas in galaxies. Observations of blueshifted interstellar absorption lines at a variety of rest wavelengths and ionization states have been observed in both local and high-redshift samples (e.g., Heckman et al. 2000; Martin 2005; Pettini et al. 2002; Shapley et al. 2003; Steidel et al. 2010; Coil et al. 2011; Kulas et al. 2012; Law et al. 2012b). The presence of outflows with blueshifted velocities relative to stars and H II regions appears to be associated with objects undergoing starbursts: UV-selected star-forming galaxies at $z = 2\text{--}3$ with large star-formation rates (SFRs) (Pettini et al. 2002; Shapley et al. 2003; Steidel et al. 2010), local ULIRGs (Heckman et al. 2000; Rupke et al. 2002; Martin 2005; Rupke et al. 2005), and local dwarf starbursts (Lequeux et al. 1995; Heckman & Leitherer 1997; Heckman et al. 2001b; Schwartz & Martin 2004). Studies of X-ray and H α emission in local samples have focused on correlating outflows with spatially-resolved properties such as star-formation rate surface density (Σ_{SFR}), morphology, and galaxy inclination (e.g., Lehnert & Heckman 1996; Heckman 2002; Strickland et al. 2004). Only recently, however, have absorption-line studies of winds at higher redshifts begun similar investigations (Sato et al. 2009; Weiner et al. 2009; Rubin et al. 2010; Steidel et al. 2010; Talia et al. 2012; Law et al. 2012b). Studies of spatially-resolved properties necessitate high-resolution imaging and careful measurement of the galactic regions in which stars are forming. These studies are particularly relevant around $z \sim 1$; examining the processes regulating star formation is critical to understanding why the global star-formation rate density declines between $z \sim 1$ and $z \sim 0$ (Reddy et al. 2008).

The study of outflows in $z \sim 1$ objects to date has relied primarily on composite spectra and visual classification of galaxy morphology (e.g., Weiner et al. 2009; Rubin et al. 2010). Here, we use a sample of galaxies drawn from the $z \sim 1$ DEEP2 redshift survey (Newman et al. 2012) to examine the relationship between outflows and host galaxy properties. For these objects, we obtain observations with the Low Resolution Imaging Spectrometer (LRIS; Oke et al. 1995;

Steidel et al. 2004) on Keck I. These LRIS spectra cover a bluer wavelength range than the DEIMOS discovery spectra from the DEEP2 survey and are inclusive of a variety of rest-frame UV features from which wind kinematics can be measured (Si II $\lambda 1526$, C IV $\lambda 1549$, Fe II $\lambda 1608$, Al II $\lambda 1670$, Fe II $\lambda 2344$, Fe II $\lambda \lambda 2374/2382$, Fe II $\lambda \lambda 2587/2600$, Mg II $\lambda \lambda 2796/2803$, and Mg I $\lambda 2852$). In this paper, we focus specifically on objects in the Extended Groth Strip (EGS) field, where an extensive multiwavelength dataset enables SFR, Σ_{SFR} , morphology, inclination, and dust attenuation to be estimated and in turn correlated with outflow properties on a per-object basis. We aim to determine which, if any, of these properties most strongly drives outflows at $z \sim 1$. Furthermore, with our unique data set we can statistically probe the geometry of galactic winds.

In Section 2, we present the imaging and spectroscopic data used in our analysis, including extensive datasets of EGS observations. We discuss SFR, a new technique for estimating galaxy areas, and Σ_{SFR} in Section 3. Absorption-line modeling is reviewed in Section 4, while Section 5 is devoted to results. In Section 6, we present a discussion of the results. Our conclusions are summarized in Section 7. Throughout the paper, we assume a standard Λ CDM cosmology with $H_0 = 70$ km s $^{-1}$ Mpc $^{-1}$, $\Omega_{\text{M}} = 0.3$, and $\Omega_{\Lambda} = 0.7$. All wavelengths are measured in vacuum. At $z = 0.7$ (1.3), an angular size of $1''$ corresponds to 7.1 (8.4) kpc.

2. SAMPLE AND OBSERVATIONS

2.1. DEEP2 Survey

The objects presented here were drawn from the DEEP2 survey conducted from 2002–2005 using the DEEP Imaging Multi-Object Spectrograph (DEIMOS) on Keck II (Newman et al. 2012). With four fields totaling three square degrees, the DEEP2 survey obtained high-quality redshifts for $\sim 30,000$ galaxies at $0.7 \leq z \leq 1.5$ brighter than $R_{\text{AB}} = 24.1$ to study clustering and evolution in galactic properties out to $z \sim 1$.

The DEIMOS spectra were obtained with a 1200 lines mm $^{-1}$ grating and a $1.''0$ slit and have a resolution of $R \approx 5000$ (Newman et al. 2012). Wavelength coverage extends from $\sim 6500\text{--}9100$ Å inclusive of the [O II] $\lambda \lambda 3727/3729$ doublet, which is typically resolved. Galaxy properties, including luminosities, colors, stellar masses (M_*), and [O II] equivalent widths, have been measured (Figure 1; Bundy et al. 2006; Willmer et al. 2006). Stellar masses were calculated from SED modeling with *BRIK* photometry, assuming Bruzual & Charlot (2003) spectral templates and a Chabrier (2003) initial mass function (IMF). For our study, modeling was done with *BRI* photometry alone if objects lacked *K*-band detections (24% of the sample).

Photometric preselection based on *BRI* colors was applied in three out of the four DEEP2 fields in order to isolate galaxies at $z \geq 0.7$. In the fourth field, the EGS, no color cuts were applied and galaxies at lower redshifts were accordingly targeted for spectroscopy. The EGS dataset is unique not only for its inclusion of more local galaxies, but also for its extensive multi-wavelength coverage from the All-Wavelength Extended Groth Strip International Survey (AEGIS; Davis et al. 2007). The objects presented in this paper are all in the EGS and

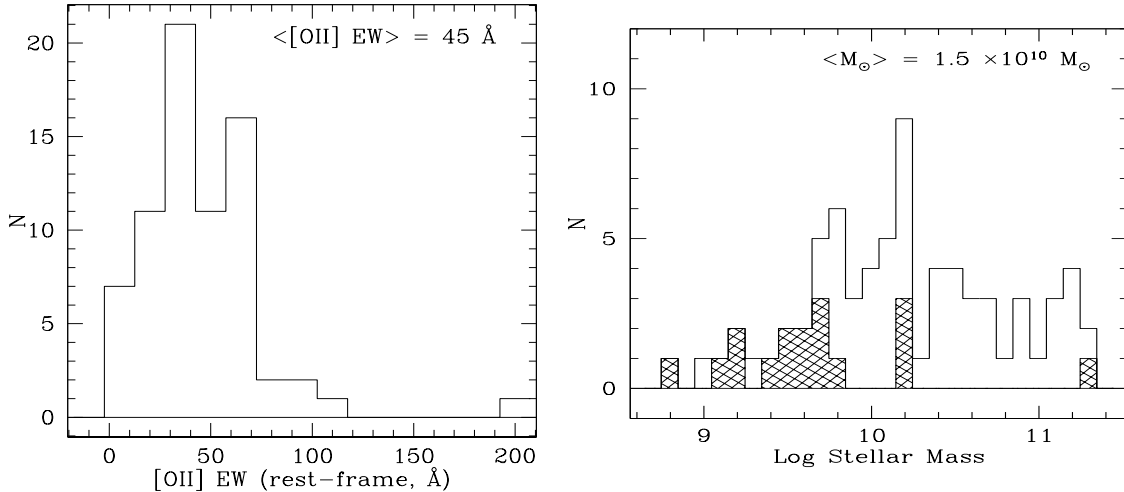


FIG. 1.— Distributions of rest-frame [O II] equivalent widths (*left*) and stellar masses (*right*) for our sample of 72 EGS objects at $0.7 < z < 1.3$. The hatched histogram in the stellar mass panel denotes galaxies without K -band detections (17 objects). Stellar masses were estimated from SED fitting using BRI (and K , when available) photometry (Bundy et al. 2006), assuming a Chabrier (2003) IMF.

consequently have, in addition to the original DEIMOS spectra, a variety of complementary data spanning from the X-ray to the radio regimes (Section 2.3).

2.2. LRIS Observations

While the DEIMOS spectra are generally dominated by nebular emission features ([O II], [Ne III], $H\gamma$, $H\delta$, $H\beta$, [O III]), the majority of low- and high-ionization interstellar absorption features tracing outflows are in the rest-frame UV and are observed at shorter wavelengths than the blue edge of the typical DEIMOS spectra in the DEEP2 survey (~ 6500 Å in the observed frame). In order to probe these outflow features (e.g., Fe II $\lambda\lambda 2344$, Fe II $\lambda\lambda 2374/2382$, Fe II $\lambda\lambda 2587/2600$, Mg II $\lambda\lambda 2796/2803$), we obtained complementary spectroscopic data for 212 objects using the LRIS spectrograph on Keck I. These observations, covering all four DEEP2 survey fields, are described in further detail in (Martin et al. 2012).

In this paper, we discuss 72 objects in the EGS, which are drawn from our larger sample of 212 spectroscopically-confirmed DEEP2 objects with LRIS follow-up (Martin et al. 2012). In Figure 2, we show the color-magnitude diagram for both the present sample of 72 objects and also the parent sample of $\sim 7,000$ spectroscopically-confirmed DEEP2 EGS objects at $0.70 < z < 1.35$. Objects with $B < 24.5$ were targeted for LRIS observations, resulting in a sample dominated by brighter, bluer galaxies. The redshift distribution of our EGS sample is presented in Figure 3, where $\langle z \rangle = 0.99 \pm 0.29$.

The LRIS data, collected in October 2007, June 2008, September 2008, and June 2009, were obtained using $1.''2$ slits on nine multi-object slitmasks targeting 20–28 objects each. The dichroic capability of LRIS was employed with the grism on the blue side and the grating on the red side. We used two set-up configurations, both with the Atmospheric Dispersion Corrector: the d680 dichroic with the 400 line mm^{-1} grism and the 800 line mm^{-1} grating (145 objects; 47 in the EGS) and the d560 dichroic with the 600 line mm^{-1} grism and the 600 line

mm^{-1} grating (67 objects; 25 in the EGS). The resolutions of the 800, 600 and 400 line mm^{-1} grisms/gratings are $R = 2000, 1100$, and 700 , respectively. Features bluer than Mg II $\lambda\lambda 2796/2803$ generally fell on the blue side while Mg II $\lambda\lambda 2796/2803$ and longer wavelength lines (e.g., [O II]) were recorded on the red side.

Continuum signal-to-noise (S/N) ratios ranged from ~ 1 –20 per pixel over the rest wavelength interval 2400–2500 Å. In Figure 4, we show several individual LRIS spectra with a range of measured S/N ratios. Integration times varied from 3–9 hours per slitmask, where objects observed with the d560 dichroic had typically shorter exposures (3–5 hours) than objects observed with the d680 dichroic (5–9 hours). The reduction procedure – flat-fielding, cosmic ray rejection, background subtraction, extraction, wavelength and flux calibration, and transformation to the vacuum wavelength frame – was completed using IRAF scripts. The spectra were continuum-normalized and composite spectra were assembled from stacks of mean-combined rest-frame spectra. For the composite spectra, we smoothed the objects obtained with the 600 line mm^{-1} grism or grating in order to account for the difference in resolution between the objects observed with the 600 line mm^{-1} and 400 line mm^{-1} setups.

2.3. AEGIS Multiwavelength Data

The 72 EGS objects presented in this paper have extensive multi-wavelength coverage from the AEGIS dataset. These data products cover observations over nine decades in wavelength, including *Chandra* X-ray, *GALEX* FUV and NUV imaging, *HST* ACS F606W (V) and F814W (I) imaging, optical CFHT and MMT observations, Palomar/WIRC J and K_s imaging, *Spitzer* IRAC and MIPS pointings, and VLA radio observations. This wealth of data permits many analyses, including the estimation of SFR, specific star-formation rate ($\text{sSFR} = \text{SFR}/M_*$), Σ_{SFR} , morphology, inclination, and dust attenuation. Here, we discuss the diffraction-limited *HST* Advanced Camera for Surveys (ACS; Ford et al. 2003) imaging that forms the backbone of our spatially-resolved analyses. In

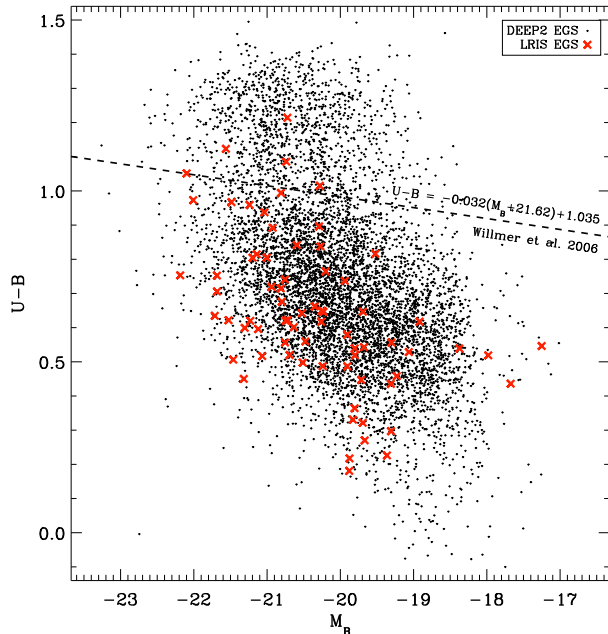


FIG. 2.— Rest-frame color-magnitude diagram with photometry corrected for Galactic extinction, assuming $H_0 = 100 \text{ km s}^{-1} \text{ Mpc}^{-1}$ (Willmer et al. 2006). Small dots show objects at $0.70 < z < 1.35$ in the EGS field of the DEEP2 survey and red crosses mark the 72 EGS objects with LRIS follow-up discussed in this paper. The red sequence and blue cloud are delineated by the dashed line (Willmer et al. 2006); we emphasize that the majority of the objects presented in this work are brighter, blue cloud galaxies.

the sample of 72 EGS objects presented here, 56 galaxies have *HST* coverage.

Reduced *HST* images (Cycle 13, Program 10134, PI Marc Davis) were drizzled from four exposures to produce final 8000×8000 pixel images with a sampling of $0.''03 \text{ pixel}^{-1}$ and a point spread function (PSF) FWHM of $\sim 0.''1$. These deep ($V = 28.75 \text{ AB } [5\sigma]$; $I = 28.10 \text{ AB } [5\sigma]$) images were used for several estimates of galaxy extent and light distribution, including the Petrosian radius, the Gini coefficient, and M_{20} . The Gini coefficient originated from the field of economics to describe the distribution of wealth in a society; the term is used in astronomy to parameterize how a galaxy’s light is distributed. Gini coefficients close to 1 indicate that a galaxy’s flux is concentrated in a few bright pixels while values closer to 0 mean that the flux is more evenly distributed over many pixels. M_{20} refers to the normalized second-order moment of the brightest 20% of a galaxy’s flux; larger M_{20} values are associated with merging systems while smaller M_{20} values describe more compact galaxies. We direct the reader to Lotz et al. (2004) for a more complete description of the Gini coefficient and M_{20} .

3. STAR-FORMATION RATES, GALAXY AREAS, AND STAR-FORMATION RATE SURFACE DENSITIES

The multi-wavelength observations of the AEGIS dataset enable detailed measurements of the star-forming properties of the sample. Based on *HST* imaging, we note that the majority of objects appear to have clumpy morphologies (Figure 5). The UV-bright clumps may be star-forming regions embedded in lower surface brightness disks (Förster Schreiber et al. 2006). We conse-

quently derive a new estimate of galaxy size inclusive of only the brightest regions likely associated with star formation and use these areas in tandem with SFR estimates in order to calculate Σ_{SFR} . We also use standard Petrosian size measurements to calculate Σ_{SFR} as well.

3.1. Star-Formation Rates

We used *Galaxy Evolution Explorer* (*GALEX*; Martin et al. 2005) and *Spitzer Space Telescope* imaging from the AEGIS dataset to estimate the SFRs of the sample. Given the significant attenuation experienced by UV radiation, SFRs inferred from *GALEX* measurements must be corrected for dust absorption. Data from *GALEX*’s FUV and NUV detectors, along with *B*-band observations (for the higher-redshift objects in the sample), were used to calculate a spectral slope, β , where the flux level over the rest-frame interval 1250–2500 Å is parametrized as $f_\lambda \propto \lambda^\beta$. Following Meurer et al. (1999), Seibert et al. (2005) derived a relationship between β and the UV attenuation, A_{UV} , based on a sample of several hundred nearby galaxies with both *GALEX* and *Infrared Astronomical Satellite* (Neugebauer et al. 1984) imaging. For the sample presented here, Schiminovich et al. (2007) used the β/A_{UV} relationship from Seibert et al. (2005) to correct *GALEX* luminosities for attenuation. The median A_{UV} value in the sample is 1.8, which corresponds to a factor of ~ 5 correction. UV SFRs corrected for dust – $\text{SFR}_{\text{UV,corr}}$ – were then calculated for a Salpeter (1955) IMF over 0.1–100 M_\odot , according to Salim et al. (2007). We converted all values to the Chabrier (2003) IMF by dividing the Salpeter (1955) values by 1.8. 54/72 objects ($\sim 75\%$) have $\text{SFR}_{\text{UV,corr}}$ measurements, where the 18 objects lacking β measurements were observed by *GALEX* but were either not significantly detected or suffered from confusion with neighboring objects⁴. The $\text{SFR}_{\text{UV,corr}}$ measurements of the sample are characterized by a median value of $12 M_\odot \text{ yr}^{-1}$ and extrema of $[1, 97] M_\odot \text{ yr}^{-1}$ (Figure 6).

These $\text{SFR}_{\text{UV,corr}}$ values are consistent with SFRs inferred from longer wavelength measurements. Robust *Spitzer* $24\mu\text{m}$ detections ($f_{24\mu\text{m}} \geq 60 \mu\text{Jy}$) were used to calculate a total infrared luminosity, L_{IR} , based on templates relating L_{IR} and $f_{24\mu\text{m}}$ (Chary & Elbaz 2001). While these templates are representative only of quiescent and starbursting galaxies – not Active Galactic Nuclei (AGN) – we note that AGN are likely a minimal contaminant in the sample given that a cross-correlation with *Chandra* X-ray catalogs yielded only 1 match for our sample above the limiting fluxes of 5.3×10^{-17} (3.8×10^{-16}) $\text{erg s}^{-1} \text{ cm}^{-2}$ in the soft (hard) bands (Laird et al. 2009). Here, soft corresponds to 0.5–2 keV and hard corresponds to 2–10 keV. At the mean redshift of our sample, $\langle z \rangle = 0.99$, these flux limits correspond to AGN luminosities of 2.7×10^{41} (1.9×10^{42}) erg s^{-1} in the soft (hard) bands. Based on bolometric corrections from Hopkins et al. (2007), the limits for both *Chandra* bands correspond to $\sim 10^{43} \text{ erg s}^{-1}$ in bolometric luminosity⁵. A SFR was then estimated from the addition of SFRs derived from L_{IR} (Kennicutt 1998) and L_{UV}

⁴ *GALEX* has a PSF of $\sim 5''\text{--}6''$ for FUV and NUV observations (Martin et al. 2005).

⁵ As we do not include the one X-ray detected object (12015320)

(Schiminovich et al. 2007), where the latter term is a UV luminosity uncorrected for dust. While only 17/72 objects presented here ($\sim 25\%$) have both UV detections and $f_{24\mu\text{m}} \geq 60 \mu\text{Jy}$, a larger sample of objects with these measurements shows a correlation between the two SFRs with a scatter of ~ 0.4 dex (Figure 7). In light of this consistency and the relative scarcity of objects with $f_{24\mu\text{m}}$ detections, we use $\text{SFR}_{\text{UV,corr}}$ (“SFR”) in all of the following analyses.

It is useful to compare the SFRs of the present sample with the SFRs of other recent outflow studies at $z \sim 1$. Weiner et al. (2009) presented an outflow survey of DEEP2 objects at $z \sim 1.4$ with 25th and 75th percentile values of SFR of 14 and $28 M_{\odot} \text{yr}^{-1}$, respectively, derived from UV measurements assuming a Kroupa (2001) IMF. Work by Rubin et al. (2010) utilized objects with smaller SFRs: 25th and 75th percentile values of SFR of 4 and $9 M_{\odot} \text{yr}^{-1}$, respectively. The Rubin et al. (2010) SFRs were also derived assuming a Kroupa (2001) IMF using UV measurements. The objects in this paper have 25th and 75th percentile values of 6 and $25 M_{\odot} \text{yr}^{-1}$, respectively, assuming a Chabrier (2003) IMF. For direct comparison with the Weiner et al. (2009) and Rubin et al. (2010) samples, these values correspond to 8 and $31 M_{\odot} \text{yr}^{-1}$, respectively, for a Kroupa (2001) IMF.

In Figure 8, we plot SFR versus stellar mass and sSFR versus stellar mass. We find a pronounced correlation between SFR and stellar mass. As this relationship is consistent with the correlation observed in the larger DEEP2 sample, the subsample of objects discussed here do not appear to have star-formation histories grossly inconsistent with other datasets.

3.2. Calculating a “Clump Area”

It has been suggested that there exists a threshold star-formation rate surface density of $\Sigma_{\text{SFR}} = 0.1 M_{\odot} \text{yr}^{-1} \text{kpc}^{-2}$ for driving an outflow in local starbursts (Heckman 2002). As estimating Σ_{SFR} requires areal information, it is important to characterize properly the extent over which star formation is occurring. While values in the literature often refer to $r = \text{half-light radius}$ or Petrosian radius (Rubin et al. 2010; Steidel et al. 2010), the clumpy morphologies of high-redshift galaxies observed in the rest-frame UV necessitate a different treatment. Rubin et al. (2010) noted that the simple approximation of πr^2 for the area of a galaxy may result in an overestimate; these authors proposed that the inclusion of only star-forming knots above a specified luminosity threshold may be the most physically motivated method for calculating a galaxy area associated with outflowing material.

As the majority of objects in our EGS sample appear to have irregular knots of star formation instead of being clearly disk-dominated (Figure 5), we used diffraction-limited *HST* *V*-band imaging to investigate appropriate areal measurements. *V*-band imaging traces rest-frame $\sim 2970 \text{\AA}$ at $z = 0.99$, the mean redshift of the sample. We began by estimating the total non-contiguous area of

in our analyses, we believe that the winds we observe are driven by star formation as opposed to AGN activity. Based on rest-frame UV spectra, the objects in our sample do not exhibit signatures of AGN activity although we acknowledge possible contributions from obscured AGN. Krug et al. (2010) note that starburst and Seyfert 2 systems show similar outflow kinematics.

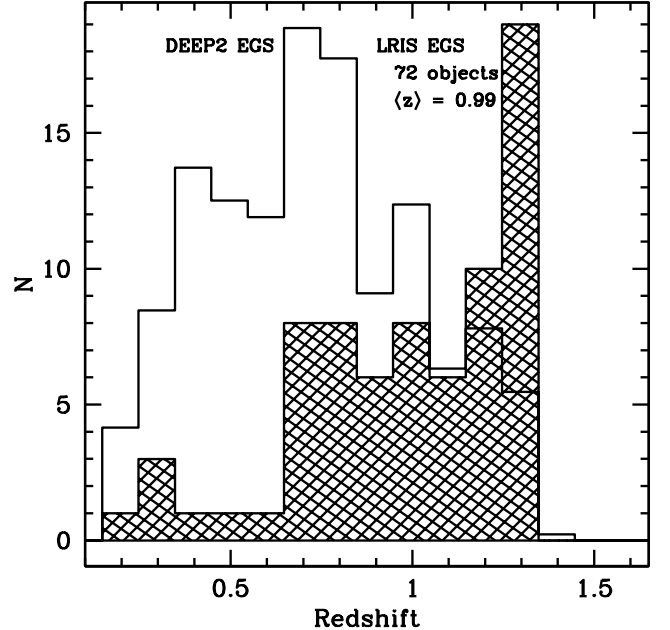


FIG. 3.— The redshift distribution of the LRIS EGS sample (hatched histogram), compared with a normalized histogram of redshifts of EGS objects in the parent DEEP2 survey. Objects at $z > 0.7$ were prioritized for LRIS follow-up, given the target wavelength coverage of $1500\text{--}2800 \text{\AA}$ in the rest-frame. The significant fraction of objects at larger redshifts reflects our heightened prioritization of galaxies at $1.19 \leq z \leq 1.35$. Observations of galaxies in this redshift interval yield simultaneous coverage of the C IV $\lambda 1549$ and Mg I $\lambda 2852$ features for the typical LRIS set-up, enabling a comparison of the kinematics of neutral, low-, and high-ionization species (Shapley et al., in prep.).

each galaxy above a certain surface brightness limit. The motivation behind this technique stemmed from flagging pixels that corresponded to some measurable physical quantity (in this case, surface brightness or, equivalently, Σ_{SFR}). Schematically, the conversion from counts per pixel in the images to Σ_{SFR} can be illustrated as follows:

$$\frac{\text{counts}}{\text{pixel}} \xrightarrow{\text{via zpt}} \frac{f_{\nu}}{\text{pixel}} \xrightarrow{\text{via } z} \frac{L_{\nu}}{\text{kpc}^2} \xrightarrow{\text{via K98}} \frac{\text{SFR}}{\text{kpc}^2} \quad (1)$$

where zpt is the *HST* *V*-band zeropoint (26.5 AB) and K98 refers to the conversion between rest-frame UV luminosity over $1500\text{--}2800 \text{\AA}$ (L_{UV}) and SFR assuming a Salpeter (1955) IMF over $0.1\text{--}100 M_{\odot}$ ($\text{SFR} = 1.4 \times 10^{-28} L_{\text{UV}}$; Kennicutt 1998). With images now in units of Σ_{SFR} , a simple Σ_{SFR} threshold can be implemented. In light of local work by Heckman (2002)⁶, we adopted the criterion $\Sigma_{\text{SFR}} = 0.1 M_{\odot} \text{yr}^{-1} \text{kpc}^{-2}$. While imposing this threshold produces areas that visually trace luminous galaxy clumps, we note two limitations to this methodology: 1) no correction for dust attenuation is applied, as estimates of the UV slope β are available for only a subset of the sample and 2) we do not account for effects of galaxy inclination i , given the uncertainties of estimating i for clumpy objects with angular sizes \sim

⁶ As the Heckman (2002) threshold is only approximate, and was calculated assuming a Salpeter (1955) IMF, we adopt the same IMF in converting from luminosity to SFR.

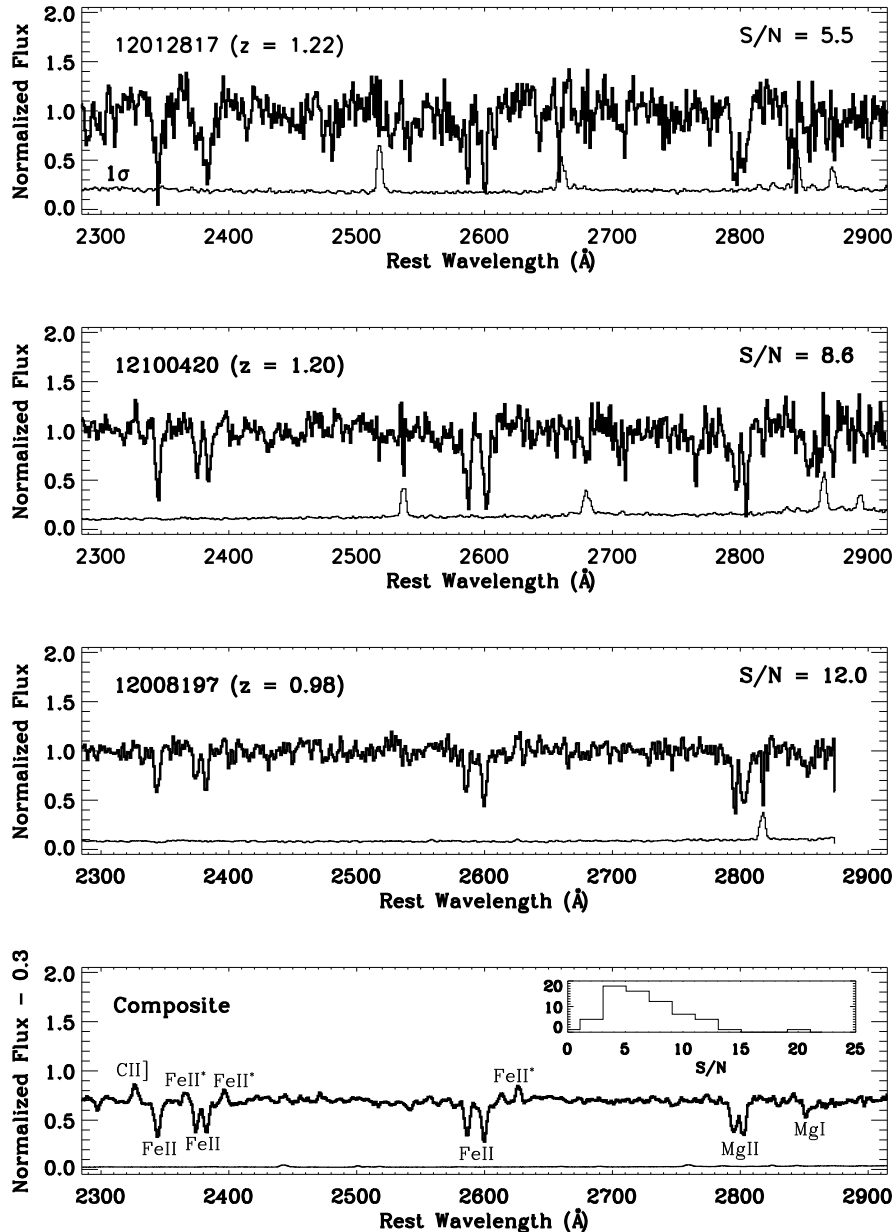


FIG. 4.— *Top three panels:* Individual LRIS spectra exhibiting a range in continuum S/N. The 1σ error spectrum is plotted for each object on the same scale. In each panel, the S/N per pixel measured over 2400–2500 Å is indicated in the upper right-hand corner. We note that Fe II and Mg II absorption lines are detected in objects with a variety of S/N values. *Bottom:* A composite spectrum assembled from all EGS spectra ($S/N = 39.1 \text{ pixel}^{-1}$), with emission and absorption lines of interest labeled. The inset shows a histogram of continuum S/N ratios, where $\langle S/N \rangle \sim 6.7 \text{ pixel}^{-1}$.

0."5. Increased dust and higher i will both act to reduce the measured luminosity.

While the unknowns of dust attenuation and inclination translate into uncertainties in the derived galaxy area (and consequently in Σ_{SFR}), there is a more fundamental limitation to adopting the aforementioned methodology: the available V -band imaging ceases to trace below rest-frame 2800 Å – the edge of the window over which the Kennicutt (1998) conversion is valid – for galaxies at lower redshifts ($z < 1.10$; 32 objects). For these comparably closer objects – comprising $\sim 60\%$ of the sample – the Kennicutt (1998) relation between L_{UV} and SFR

cannot be applied.

It was accordingly necessary to develop a new technique for estimating areas of the entire sample, irrespective of redshift. To this end, we focused on characterizing the areas of the higher redshift galaxies in the sample ($z > 1.10$; 24 objects) for which the V -band imaging *does* trace rest-frame 1500–2800 Å. For each of these objects, we noted the area calculated using the methodology described above and the threshold $0.1 M_{\odot} \text{ yr}^{-1} \text{ kpc}^{-2}$. We then sought to parametrize these physically-motivated areas as containing a simple percentage (N) of the total flux within the Petrosian radius, R_{P} . This technique

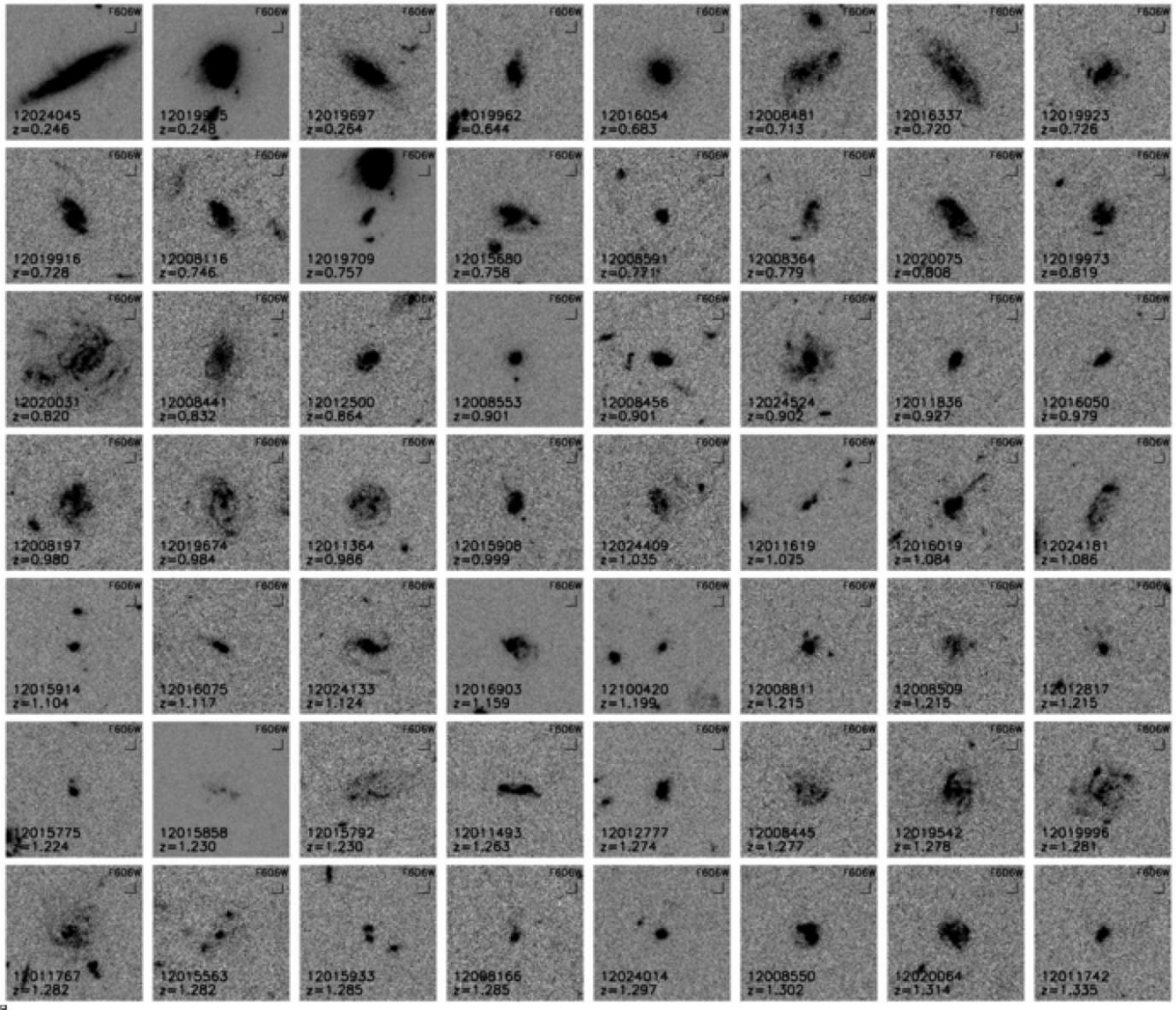


FIG. 5.— V -band thumbnails of the 56 objects with HST imaging, ordered by ascending redshift. Each postage stamp is $6''$ on a side and oriented with North up and East to the left. Note the clumpy morphologies and discrete star-forming clumps of many objects. At the mean redshift of the sample, $\langle z \rangle = 0.99$, the V -band traces $\sim 3000 \text{ \AA}$ in the rest-frame.

enabled us to estimate an average value for N and then apply this value uniformly to both the higher and lower redshift galaxies.

We found that, with the exception of several diffuse disks and extremely compact spheroids, the majority of objects required $N = [40-80]$. The median of the sample was $N = 74$; we adopted this value as representative of the fractional flux within R_P that traced regions of intense star formation. For each galaxy with HST imaging, we calculated the area derived by adding flux-ordered pixels, brightest first, until the enclosed flux was 74% of the total flux within R_P ⁷. This method permits a single, systematic area calculation (A_{74}) for each galaxy independent of redshift while still being based on the physical grounding of a surface brightness threshold. We make the implicit assumption that N does not vary sig-

nificantly over the range of look-back times probed by our sample.

We find that areas calculated using this new technique are, on average, a factor of 3.7 smaller than the areas inferred from the V -band Petrosian radii: $A_{74} \sim \pi R_P^2 / 3.7$. As seen in Figure 9, A_{74} appears to closely trace luminous clumpy regions⁸ while the Petrosian area consistently overestimates the area likely associated with star formation. We consequently favor the adoption of A_{74} over πR_P^2 , although we use both area estimates below in tandem with derived SFRs in order to calculate Σ_{SFR} . Given the strong correlation between A_{74} and πR_P^2 , we note that our primary results remain unchanged regardless of which area estimate is adopted (Section 5). While the initial motivation for calculating A_{74} was to isolate an area measurement distinct from, and uncorrelated with,

⁷ Two objects were excluded from this analysis (12008364 and 12015792), given that their surface brightness levels were too low to measure R_P .

⁸ The HST resolution, while excellent, is finite ($\text{FWHM} \sim 0.''1$), so these areas represent upper limits.

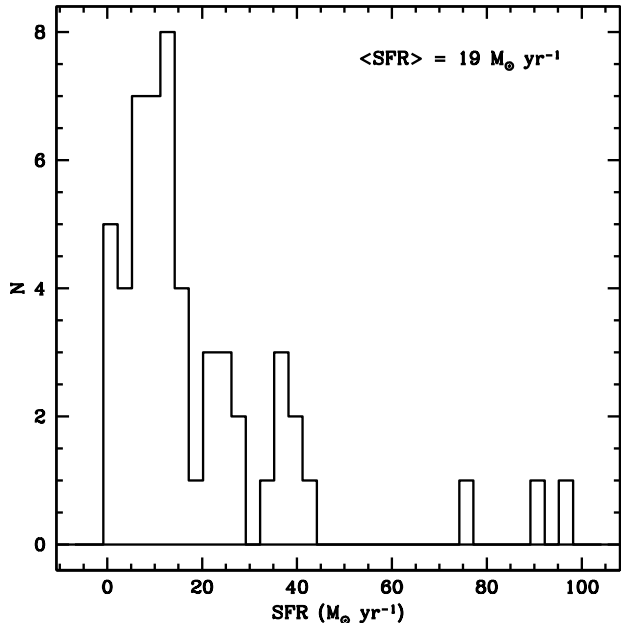


FIG. 6.— Histogram of SFRs, assuming a Chabrier (2003) IMF. The sample is characterized by a mean value of $\langle \text{SFR} \rangle = 19 M_{\odot} \text{ yr}^{-1}$.

πR_{P}^2 , our finding that these two area estimates are in fact strongly linked is evidence that the structural morphologies of the galaxies in the sample are rather similar. If the light distributions of the galaxies were widely disparate, we would not expect that galaxies with larger Petrosian areas would also have larger A_{74} areas while galaxies with smaller πR_{P}^2 would likewise have smaller clump areas. We verified that the correlation between πR_{P}^2 and clump area holds for a variety of N values.

3.3. Star-Formation Rate Surface Densities

With two estimates of galaxy area (A_{74} and πR_{P}^2) and one estimate of SFR, we calculated the star-formation rate surface densities of the sample. We define two Σ_{SFR} quantities, depending on which area measurement we adopt:

$$\Sigma_{\text{SFR}}(A_{74}) = \text{SFR}/A_{74} \quad (2)$$

$$\Sigma_{\text{SFR}}(R_{\text{P}}) = \text{SFR}/\pi R_{\text{P}}^2 \quad (3)$$

Figure 10 shows the distributions of $\Sigma_{\text{SFR}}(A_{74})$ and $\Sigma_{\text{SFR}}(R_{\text{P}})$. Irrespective of the area measurement assumed, most objects have star-formation rate surface densities above the local threshold of $0.1 M_{\odot} \text{ yr}^{-1} \text{ kpc}^{-2}$ thought to be necessary for driving an outflow (Heckman 2002). While this is by construction for $\Sigma_{\text{SFR}}(A_{74})$, the fact that greater than 70% of objects also have $\Sigma_{\text{SFR}}(R_{\text{P}}) > 0.1 M_{\odot} \text{ yr}^{-1} \text{ kpc}^{-2}$ leads to the prediction that if a threshold Σ_{SFR} is the sole requirement for driving an outflow, the majority of objects ought to exhibit blueshifted Fe II features. Of course, other factors such as local environment, halo mass, galaxy escape speed, and viewing angle, as well as the S/N of the data, may strongly influence the observed fraction of galaxies hosting winds. As discussed above, we do not correct A_{74} areas for either dust or inclination effects. We find kinematic evidence

for 1σ significant outflows based on Fe II absorption lines in 40% of the sample (Section 4.2), although we note that the Mg II features often exhibit strong blueshifts of their centroids and blue wings even when the Fe II lines do not (Section 6).

4. MODELING ABSORPTION LINES

4.1. Systemic Redshift

Spectral analysis of outflowing gas requires an accurate determination of systemic redshift, z_{sys} . Nebular emission lines such as [O II] $\lambda\lambda 3726/3729$, [O III] $\lambda\lambda 4959/5007$, and the Balmer series trace star forming regions and are consequently assumed to be at rest with respect to a galaxy’s center of mass. While both the DEIMOS and LRIS spectral datasets are inclusive of nebular features, it is preferable to calculate z_{sys} from the LRIS spectra in order to ensure constancy in both slit position angle and spatial sampling for the z_{sys} and outflow measurements. We constructed a linear, S/N-weighted sum of three template spectra – post-starburst, old stellar population absorption line, and emission line – and used the DEEP2 IDL pipeline to compare the template spectrum with each science spectrum. In the estimation of systemic redshifts, only lines with rest wavelengths longer than 3000 \AA were fit in order to exclude bluer features tracing winds. The χ^2 of the fit was minimized according to redshift, and a best-fit z_{sys} was extracted. For 63/72 objects ($\sim 90\%$), it was possible to extract z_{sys} from the LRIS spectra. For the nine objects in the sample without [O II] spectral coverage in the LRIS data, z_{sys} was calculated from the DEIMOS spectra using the same technique. In comparing measurements of z_{sys} with those given for the DEIMOS data in the DEEP2 catalogs, we find a mean discrepancy and standard deviation of $\langle \delta z \rangle = 9 \times 10^{-5}$ (16 km s^{-1}) and $\sigma_{\delta z} = 2.6 \times 10^{-4}$ (42 km s^{-1}), respectively. These results are consistent with the values obtained when considering the entire LRIS sample (Martin et al. 2012).

4.2. Fitting Lines – Fe II Centroids

Simulations of galactic winds suggest that multiple fronts of outflowing material are present along any one sightline (e.g., Fujita et al. 2009). While fitting several outflow components simultaneously would in principle provide the best diagnostic of these superimposed winds, the finite spectral resolution and S/N of observations typically limit fitting to a single wind component that is assumed to trace the integrated bulk motion of the outflow. The measurements we present here, which derive from and are discussed more fully in Martin et al. (2012), make the approximation of a single outflow velocity. Furthermore, we do not decompose the observed absorption profile into both a wind component and an absorption trough at the systemic velocity, where the latter may arise from stationary material present in stellar atmospheres or in the surrounding interstellar medium. Several recent outflow studies have modeled absorption lines as arising from the sum of wind and systemic components (Weiner et al. 2009; Chen et al. 2010; Coil et al. 2011), although the implementation of such a technique is strongly dependent on the quality of the spectroscopic data. Steidel et al. (2010) note that the limited resolution and finite S/N of typical spectroscopic observations

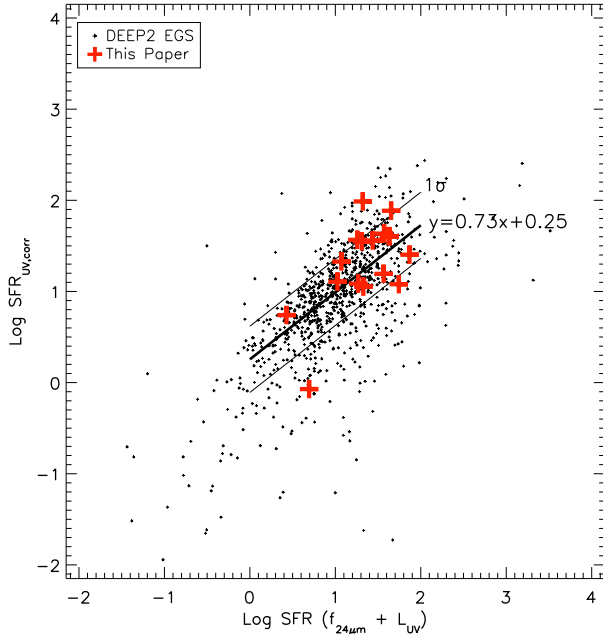


FIG. 7.— Comparison of two SFR indicators: a UV-corrected SFR ($\text{SFR}_{\text{UV,corr}}$, where the dust correction is inferred from UV colors) and a SFR inferred from the sum of $24\mu\text{m}$ data and uncorrected UV observations: $\text{SFR}(f_{24\mu\text{m}} + L_{\text{UV}})$. The units of SFR are $M_{\odot} \text{ yr}^{-1}$. The bold crosses indicate the 17 EGS objects in this paper with robust $24\mu\text{m}$ data and the smaller crosses mark objects in the larger DEEP2 EGS parent sample. Data in the interval $1 < \text{SFR}(f_{24\mu\text{m}} + L_{\text{UV}}) < 100$, the approximate range of SFRs measured in this paper, have been used to calculate the best-fit line ($y = 0.73x + 0.25$). The good agreement between $\text{SFR}_{\text{UV,corr}}$ and $\text{SFR}(f_{24\mu\text{m}} + L_{\text{UV}})$, $\sigma \sim 0.4$ dex, supports adopting $\text{SFR}_{\text{UV,corr}}$ given the relatively small number of objects with $24\mu\text{m}$ data.

at $z = 1-3$ often preclude fitting a more complex model than a single absorption profile. In light of the S/N of our data, we do not apply a correction for material at the systemic velocity⁹. The outflow velocities presented here are accordingly conservative lower limits (Martin et al. 2012).

In Martin et al. (2012), we fit a single-component model simultaneously to five resonance Fe II lines at 2249.88, 2260.78, 2344.21, 2374.46, and 2586.65 Å in the LRIS spectra. These lines trace cool ($T < 10^4$ K) gas. Upon absorbing a resonance photon at one of these five wavelengths, the Fe II ion can decay by either emitting a photon of equal wavelength as the one it just absorbed (scattering) or emitting a photon to intermediate fine-structure levels (fluorescence). The presence of these fine-structure levels ensures that the resonance absorption lines are not simply filled in with scattered re-emitted resonance photons (“emission filling”; Prochaska et al. 2011). The Fe II features at 2382.76 and 2600.17 Å are more susceptible to emission filling due to their dearth of alternate decay paths (Prochaska et al.

⁹ As the majority of the sample is composed of actively star-forming galaxies, stellar absorption in the Fe II and Mg II lines is assumed to be minimal (e.g., Bruzual & Charlot 2003). While objects with $U-B$ colors between the red sequence and the blue cloud (i.e., “Green Valley” galaxies) may experience substantial stellar Mg II absorption, we have verified that our results are qualitatively unchanged when the ten Green Valley galaxies in our sample are omitted from analyses.

2011, Martin et al. 2012b, in prep.) and we purposefully omit these lines from fitting as emission filling can shift the measured centroid of absorption lines to bluer wavelengths (e.g., Prochaska et al. 2011). The Mg II features at $\lambda\lambda 2796/2803$ are particularly affected by emission filling as these transitions have no fine-structure levels; in the absence of dust extinction, all absorbed resonance photons are re-emitted to the ground state. We accordingly do not measure the centroids of Mg II absorption but instead develop a method to parameterize the blue wing of the absorption profile (Section 4.3).

The model fit to the Fe II lines has four free parameters: Doppler shift, column density, Doppler width (b , where $b = \sqrt{2}\sigma = \text{FWHM}/2\sqrt{\ln 2}$), and covering fraction. Due to the low spectral resolution and finite S/N of the observations, the Doppler shift fit to the five Fe II lines is the primary quantity of interest; the other three parameters of the model will not be discussed in this paper. We measured velocities for 61/72 objects, where 11 objects had no significant absorption lines and therefore could not be modeled, and find velocities ranging from -217 km s^{-1} to $+155 \text{ km s}^{-1}$ with a mean of -16 km s^{-1} and a 1σ dispersion of 82 km s^{-1} (Figure 11). This range and mean are similar to the values measured for the entire LRIS sample (Martin et al. 2012). We define here the convention of employing “ V_1 ” to refer to the measured velocity shift of the deepest part of the Fe II absorption line fit, relative to a systemic reference frame defined by [O II] and Balmer emission lines. Negative V_1 values refer to blueshifts (“outflows”) while positive V_1 values correspond to redshifts (“inflows”). Fe II velocity shifts significant at the 1σ (3σ) level are observed in $\sim 40\%$ (10%) of the sample (Figure 12). Within the sample of objects with 1σ (3σ) outflows, $\langle V_1 \rangle = -93 \text{ km s}^{-1}$ (-130 km s^{-1}). We can also parameterize the sample by stating what percentage of objects exhibit outflows at a certain threshold velocity (Martin et al. 2012). The 1σ error associated with the each object’s velocity can be taken as the standard deviation of a Gaussian probability distribution for the outflow velocity of the object. Using these probability distributions, we calculated the fraction of objects in the sample having blueshifts of at least -40 km s^{-1} (i.e., the systemic redshift uncertainty; Section 4.1). We estimated errors on the outflow fraction via bootstrap resampling. We find that $40 \pm 5\%$ of objects show outflows with blueshifts of at least -40 km s^{-1} . The outflow characteristics of the EGS objects presented in this paper are consistent with the properties of the parent sample discussed in Martin et al. (2012).

While the blueshifted signature of outflowing gas has been observed at a range of look-back times and in a variety of galaxy types (e.g., Steidel et al. 1996; Franx et al. 1997; Pettini et al. 2000, 2001; Shapley et al. 2003; Martin 2005; Veilleux et al. 2005; Rupke et al. 2005; Tremonti et al. 2007; Weiner et al. 2009; Steidel et al. 2010; Coil et al. 2011), detections of redshifted interstellar absorption lines – i.e., gas inflows – are much more elusive (Coil et al. 2011; Giavalisco et al. 2011; Rubin et al. 2012). We defer a discussion of individual objects in our sample showing redshifted absorption lines to our accompanying demographics paper (Martin et al. 2012).

In objects with blueshifted Fe II profiles, we still ob-

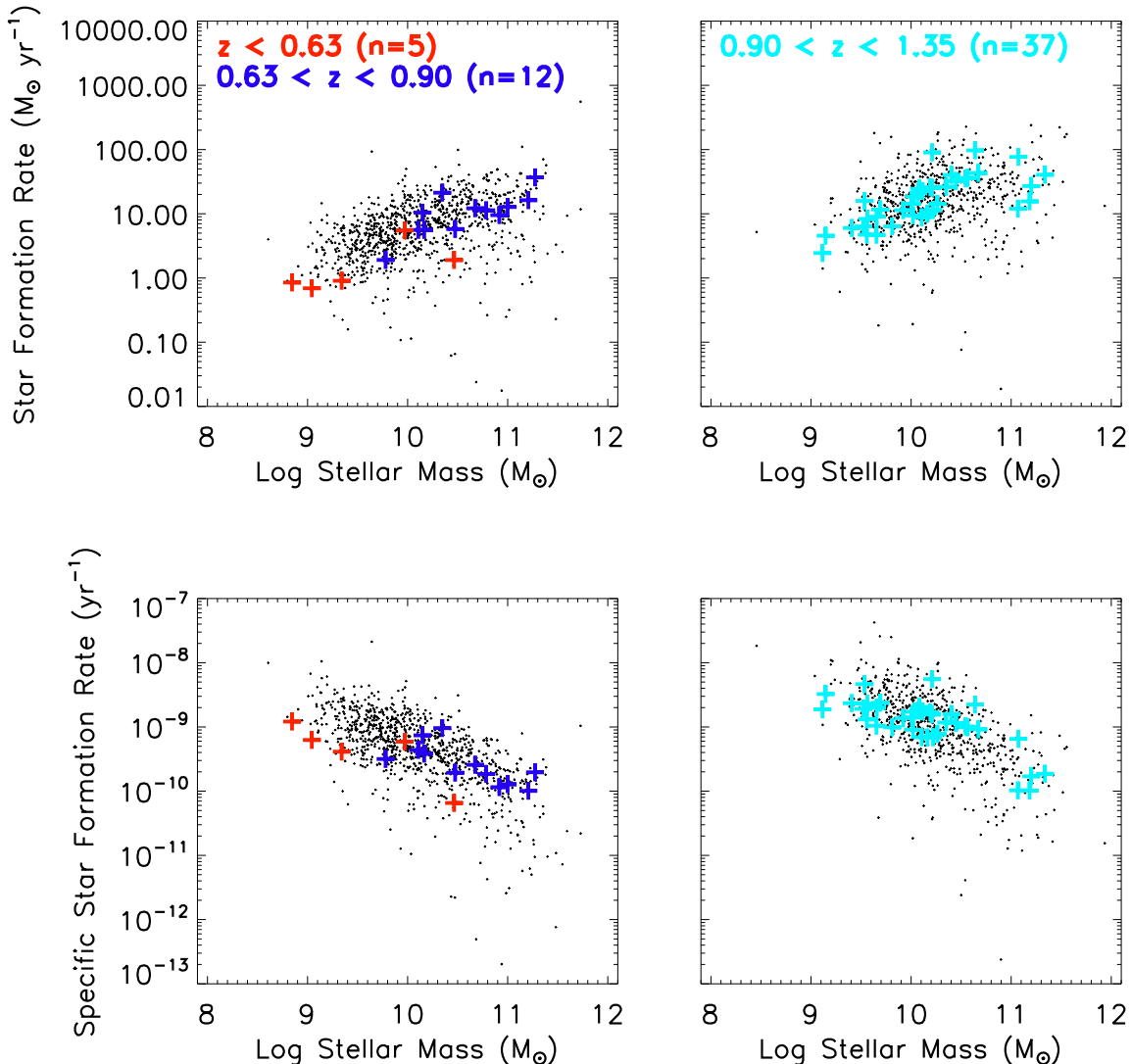


FIG. 8.— *Top left*: SFR versus stellar mass, where the small background points indicate EGS galaxies at $0.63 < z < 0.90$ without LRIS follow-up and colored crosses mark galaxies observed with LRIS, divided into two redshift bins. *Top right*: Same as the plot on the left, for the redshift interval $0.90 < z < 1.35$. We note that the data presented in this paper have stellar masses and SFRs consistent with the parent DEEP2 sample. *Bottom*: Stellar mass versus sSFR, where symbols are as above.

serve significant absorption at the systemic velocity of the galaxy. These absorption profiles are similar to those presented in Weiner et al. (2009) and Rubin et al. (2010) and are distinctly different from those appearing in Tremonti et al. (2007). The massive post-starburst galaxies at $z \sim 0.6$ in the Tremonti et al. (2007) sample exhibit Mg II velocities ranging from 500-2000 km s^{-1} , where the profiles of Mg II are blueshifted enough as to nearly eliminate any residual absorption at z_{sys} . It is evident that the systems presented in this work represent a more typical star-forming population than the galaxies discussed in Tremonti et al. (2007).

4.3. Maximal Outflow Velocity

While outflow velocities can be measured from the centroids of Fe II absorption lines, as discussed above, another complementary technique widely used for parameterizing outflow velocities utilizes the Mg II doublet features at 2796.35 and 2803.53 \AA (Weiner et al. 2009;

Giavalisco et al. 2011; Rubin et al. 2012). As the Mg II transitions are resonantly trapped – such that no decay paths exist other than the re-emission of resonance photons – these absorption lines are highly susceptible to filling from resonance emission lines. In the presence of a net outflow of gas, this filling shifts the centroid of Mg II absorption to bluer wavelengths due to the sum of blueshifted and redshifted emission preferentially filling in the absorption around the systemic velocity. The most meaningful velocity measurements of Mg II are therefore those made largely independently of the Mg II centroid. We quantify shifts in Mg II using a technique reliant on the profile of the blue side of the 2796 \AA feature; we do not use the 2803 \AA feature as it may be contaminated by emission from the 2796 \AA line. We adopt a methodology similar to the $V_{10\%}$ measurement of Weiner et al. (2009), as described in Martin et al. (2012). Firstly, we isolate the minimum of the 2796 \AA trough and proceed

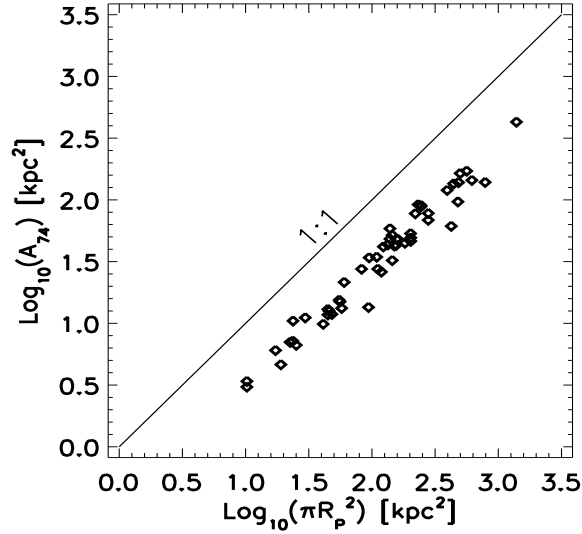
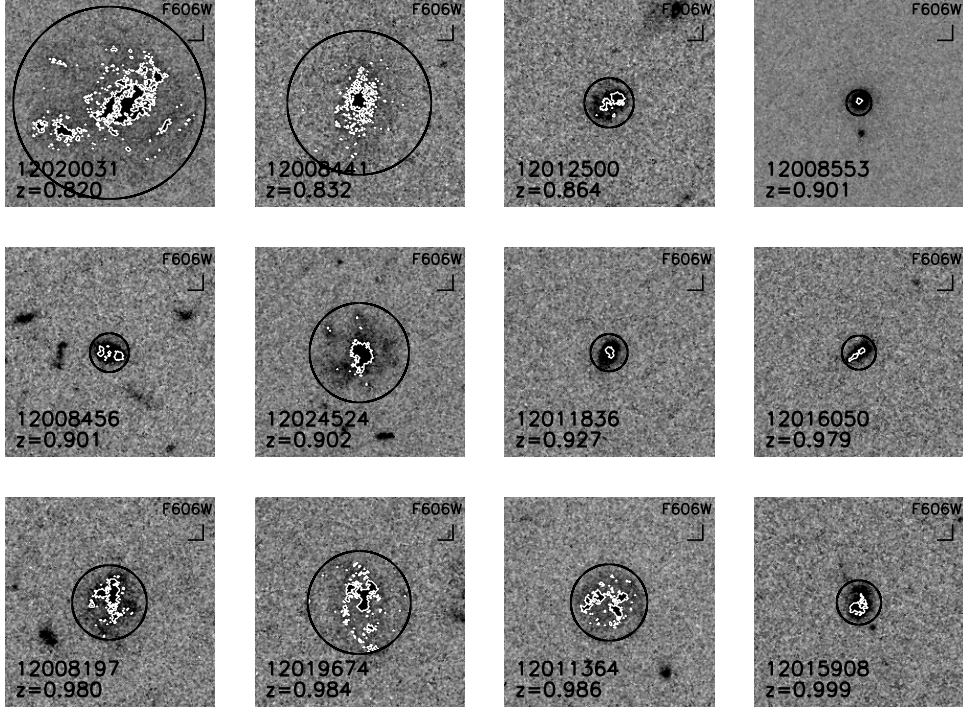


FIG. 9.— V -band HST thumbnails, $6''$ on a side, are shown for a subset of 12 objects to illustrate the A_{74} clump areas derived in Section 3. These 12 objects were chosen as representing a diversity of clump areas, from compact, contiguous areas to more diffuse, segmented areas. Petrosian radii are plotted as black circles while the clump areas are shown as white contours. The ratio between the areas — $\pi R_P^2/A_{74}$ — is indicated in the lower right of each thumbnail. The lower plot compares the πR_P^2 and A_{74} areas for the sample, where $\langle \pi R_P^2/A_{74} \rangle \sim 3.7$. We note that the strong correlation between the Petrosian area and the clump area explains the similar results obtained with the two Σ_{SFR} measurements (Section 5).

to shorter wavelengths until the sum of one pixel and its uncertainty, σ , is greater than a threshold value defined by the data’s continuum S/N: $1.0 - \frac{1.0}{S/N}$. We record the wavelength value at which this threshold is first met, perturb the science spectrum by a value drawn from a Gaussian distribution of width σ , and repeat the same procedure a total of 1000 times. We iteratively compute the average of these 1000 wavelengths excluding outliers and adopt this value as the maximal outflow velocity of Mg II, $V_{max}(\text{Mg II})$. We measure an analogous maximal

outflow velocity for the Fe II 2374 Å feature using the same technique, $V_{max}(\text{Fe II})$. We choose to utilize the 2374 Å feature over other Fe II lines given that the blue wings of other Fe II features are often contaminated by neighboring absorption lines; the only feature close to the blue side of the 2374 Å line is a fine-structure Fe II* emission line at 2365 Å (-1124 km s^{-1}).

We report maximal outflow velocities only for composite spectra, in light of the following limitations of

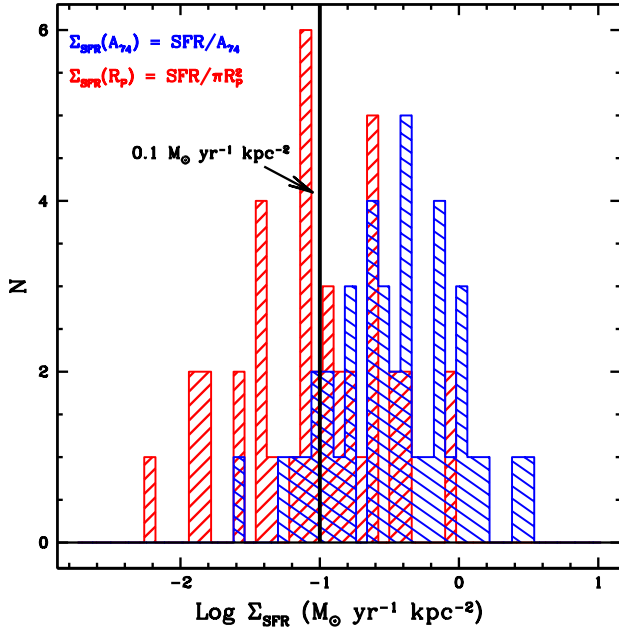


FIG. 10.— Distributions of star-formation rate surface densities $\Sigma_{\text{SFR}}(A_{74})$ and $\Sigma_{\text{SFR}}(R_P)$, where these quantities are calculated using SFR and either A_{74} or πR_P^2 . Greater than 70% of objects have $\Sigma_{\text{SFR}}(R_P) > 0.1 M_{\odot} \text{ yr}^{-1} \text{ kpc}^{-2}$, the local threshold for driving an outflow (Heckman 2002). The two objects with the highest $\Sigma_{\text{SFR}}(A_{74})$ and $\Sigma_{\text{SFR}}(R_P)$ – 12015914 and 12100420 – are both extremely compact galaxies with A_{74} (πR_P^2) areas of ~ 3 (10) kpc^2 .

the maximal outflow velocity technique. Firstly, only resolved absorption lines will yield meaningful maximal outflow velocities, given that unresolved absorption lines simply reflect the instrumental profile as opposed to the intrinsic distribution of gas kinematics. Secondly, as discussed above, maximal outflow velocities are strongly dependent on the S/N of the spectroscopic data, with higher S/N data showing more blueshifted values. The uniformly high S/N of the composite spectra ($27\text{--}39$ pixel^{-1}) ensure that the effects of differential S/N are largely mitigated. We measure $V_{\text{max}}(\text{Mg II})$ ranging from $[-605, -855]$ km s^{-1} while $V_{\text{max}}(\text{Fe II})$ varies from $[-444, -614]$ km s^{-1} . The typical FWHM of the Mg II absorption lines is 665 km s^{-1} , significantly larger than the instrumental resolution (FWHM = 435 km s^{-1}). Therefore, the Mg II lines are resolved and yield meaningful $V_{\text{max}}(\text{Mg II})$ measurements.

5. RESULTS

With measurements of the star-forming and structural properties of the sample, we now turn to examining the correlations between these parameters and outflow velocity. We focus here on galaxy properties inferred from the ancillary data of the EGS (morphology, inclination, SFR, sSFR, Σ_{SFR} , etc.). A discussion of how outflows relate to galaxy parameters such as stellar mass, color, redshift, and luminosity measured for all objects in the parent DEEP2 sample appears in Martin et al. (2012). A comparison of the kinematics of lines tracing high- and low-ionization interstellar features will also be presented in an upcoming paper (Shapley et al., in prep.).

We adopt two complementary techniques when pre-

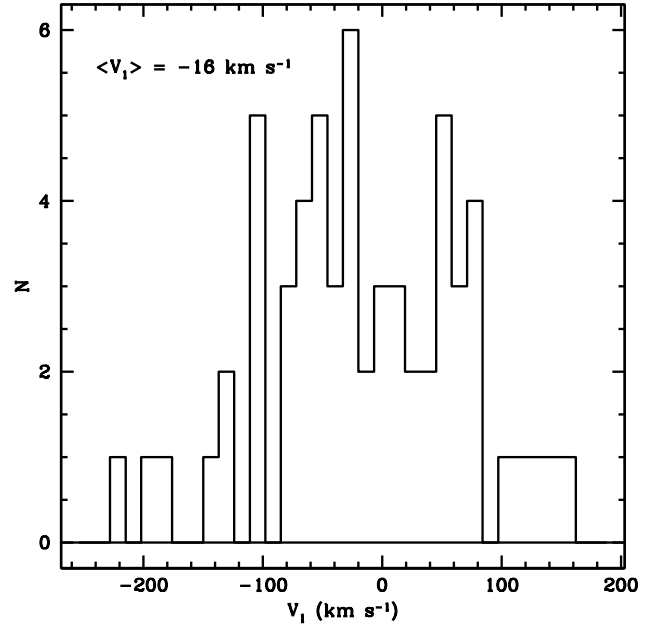


FIG. 11.— Histogram of outflow velocities measured from fitting Fe II interstellar absorption lines. Outflows (negative V_1 values) are seen at the 1σ level in $\sim 40\%$ of the sample. A non-negligible fraction of objects ($\sim 25\%$) show positive Fe II velocities at the 1σ level. The sample as a whole is characterized by $\langle V_1 \rangle \sim -16 \text{ km s}^{-1}$, with a 1σ scatter of 82 km s^{-1} .

sending the data: 1) direct comparison of individual outflow velocities with galaxy properties and 2) the construction of composite spectra based on subsamples of objects exhibiting similar star-forming or structural characteristics. These methods are both useful in that the former enables ones to draw conclusions about specific objects while the latter produces high S/N spectra from which global, averaged trends can be inferred across the sample as a function of a single property. In Table 1, we present a summary of the data including redshift, luminosity, color, stellar mass, SFR, dust attenuation, areal measurements, and outflow velocity. Summaries of outflow velocities and correlation coefficients appear in Tables 2 and 3.

We focus on results from the resonance Fe II and Mg II absorption features, using outflow velocities measured from both the centroids and blue wings of these lines. At the end of this section, we present basic analyses of the strength of Mg II absorption. Forthcoming papers will include a more thorough discussion of both Mg II and fine-structure Fe II* emission (Kornei et al. 2012b, in prep. and Martin et al. 2012b, in prep.).

5.1. Star Formation and Outflows

The relationship between SFR and outflow velocity is one of the most commonly investigated correlations in the study of outflows (e.g., Martin 2005; Sato et al. 2009; Weiner et al. 2009; Rubin et al. 2010). Martin (2005) compiled data from a variety of local ULIRGs, LIRGs, and starburst dwarfs spanning four decades in SFR and showed that outflow velocity is related to SFR as $V \propto \text{SFR}^{0.35}$. While this trend is consistent with the canonical picture of galactic-scale outflows arising from the combined effects of stellar and supernovae winds

(Leitherer & Heckman 1995; Veilleux et al. 2005), recent studies probing more limited ranges in SFR have often failed to reproduce the Martin (2005) correlation (Rupke et al. 2005; Steidel et al. 2010; Law et al. 2012b). As the $V \propto \text{SFR}^{0.35}$ relation flattens for galaxies with SFRs $\gtrsim 10\text{--}100 M_{\odot} \text{ yr}^{-1}$ (Martin 2005) – the very interval probed by most investigations – Rupke et al. (2005) propose that the bulk of studies simply do not span a large enough SFR interval to unambiguously detect a trend. The inclusion of low-SFR dwarf galaxies with low outflow velocities may be necessary for detecting a correlation between outflow velocity and SFR (Heckman et al. 2011). Weiner et al. (2009) examined the Mg II doublet in a sample of DEEP2 galaxies at $z = 1.4$ and found a dependence of outflow velocity on SFR consistent with the result from Martin (2005). This result is surprising given that the Weiner et al. (2009) sample spans a much more limited SFR interval ($\sim 7\text{--}180 M_{\odot} \text{ yr}^{-1}$) than the $0.1\text{--}1000 M_{\odot} \text{ yr}^{-1}$ range of Martin (2005). Weiner et al. (2009) employed two different techniques to parametrize the velocity of outflowing Mg II: a “median velocity” containing 50% of the absorption and a “maximal velocity” where the outflow crosses 10% or 25% absorption. The median velocity method is most akin to the centroid technique used in this paper and in other recent studies of outflows (Rubin et al. 2010; Steidel et al. 2010; Krug et al. 2010; Law et al. 2012b) while the maximal velocity is similar to our $V_{max}(\text{Mg II})$ measurement. Relying on composite spectra, Weiner et al. (2009) found that SFR was correlated with the 10% maximal velocity of Mg II such that $V \propto \text{SFR}^{0.38}$. These authors did not find a significant trend between SFR and the Mg II median velocity. In the analyses below, we employ the Spearman ρ correlation test to examine how well variables are correlated. We report the Spearman rank-order correlation coefficient, r_S , and the number of standard deviations from the null hypothesis that the quantities are uncorrelated.

5.1.1. Individual Measurements

In the left panel of Figure 13, we plot V_1 versus SFR. We do not find a significant correlation ($r_S = -0.17$; 1.2σ from the null hypothesis) between SFR and V_1 across the sample, although this is not unexpected given the limited range in SFR probed by the data ($\sim 1\text{--}97 M_{\odot} \text{ yr}^{-1}$; Rupke et al. 2005; Steidel et al. 2010; Law et al. 2012b), the small sample size, the S/N of the data, and the fitting method used for measuring outflow velocities (centroid fitting of Fe II). The three objects with the highest SFRs ($> 75 M_{\odot} \text{ yr}^{-1}$) show small Fe II blueshifts ($V_1 > -65 \text{ km s}^{-1}$); we propose that the sample’s small dynamic range in SFR, the limited number of objects considered, the lack of high-resolution spectroscopy, and the methodology of employing centroid measurements of Fe II may all contribute to this result.

We observe a weak correlation between sSFR and V_1 outflow velocity (Figure 13, *right*): $r_S = -0.33$; 2.3σ from the null hypothesis. As sSFR is a ratio between SFR (where higher values should produce stronger winds) and stellar mass (where larger values should hinder winds, assuming that the gravitational potential energy of a system increases with increasing stellar mass), one would expect that sSFR is a tracer of both the energetics and

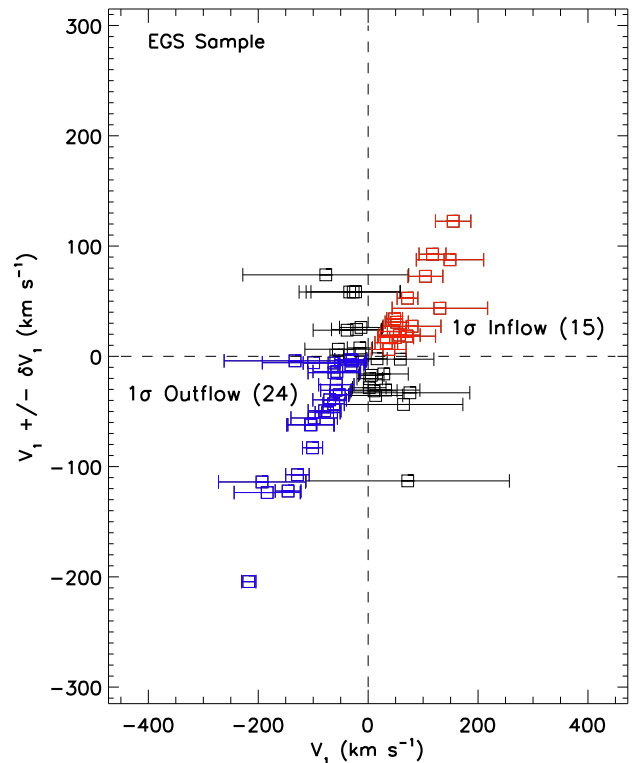


FIG. 12.— A graphical representation of outflows and inflows, for the 61 objects with measured velocities. The y-axis is the measured Fe II outflow velocity modulated by its 1σ uncertainty, where the uncertainty was added to the velocity for objects showing outflows ($V_1 < 0 \text{ km s}^{-1}$) and subtracted from objects exhibiting inflows ($V_1 > 0 \text{ km s}^{-1}$). With the Fe II outflow velocity as the x-axis, the plot divides into quadrants: objects with significantly detected outflows cluster in the lower left (blue points) and galaxies with significantly detected inflows appear in the upper right (red points).

gravitational potential of a galaxy and should therefore correlate with the observed velocity of winds. While Chen et al. (2010) do not find a trend between sSFR and either outflow velocity or the equivalent width of the outflow component in a large sample of Sloan Digital Sky Survey (SDSS; York et al. 2000) galaxies at $z \sim 0.1$, these authors hypothesize that the lack of correlation with the strength of the outflow component may be due to the effects of dust shielding on the particular atomic species used to trace winds at low redshift. Rubin et al. (2010) also fail to find a trend between sSFR and outflow velocity at $z \sim 1.4$, although these authors draw their conclusions solely based on co-added spectra¹⁰. While Prochaska et al. (2011) caution that stacked spectra show only a smeared version of the original emission and absorption features present in the component spectra, we find that the composite spectra discussed below reflect the trends of the individual measurements. Therefore, the fact that Rubin et al. (2010) do not observe a trend between sSFR and outflow velocity is more likely a result of the low S/N of their data rather than a direct consequence of relying on co-added spectra.

We find the strongest trend with V_1 outflow velocity when SFR is normalized by a representative galaxy area.

¹⁰ These stacked spectra have typical S/N values of 6.0 per pixel, comparable to our individual spectra (Figure 4).

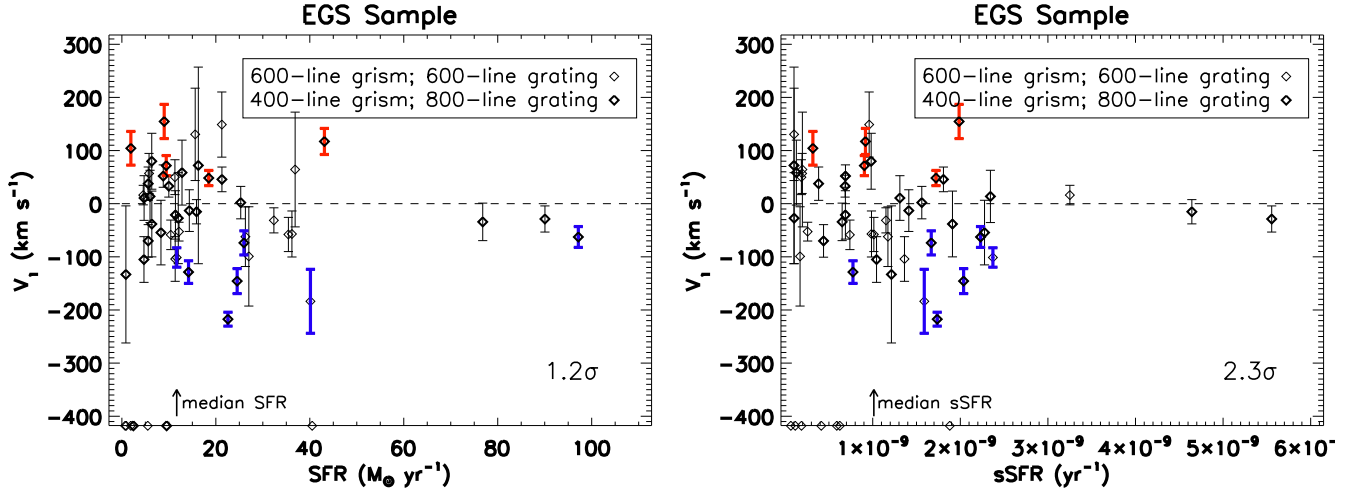


FIG. 13.— *Left*: V_1 outflow velocity versus SFR. Objects with 3σ detected outflows and inflows are indicated in blue and red, respectively. The grism and grating pair used in the LRIS observations is noted and the SFRs of objects without measured velocities (due to poor spectral signal-to-noise) appear along the x-axis. In the lower right, we indicate the significance level of the correlation. There is not a strong trend between SFR and outflow velocity in our sample, possibly due to the limited range in SFR probed by the data ($\sim 1\text{--}100 M_\odot \text{yr}^{-1}$; Rupke et al. 2005; Steidel et al. 2010; Law et al. 2012b). *Right*: V_1 outflow velocity versus sSFR, where a correlation is observed between V_1 and sSFR at the 2.3σ ($r_S = -0.33$) level. Symbols are the same as in the V_1 versus SFR plot.

Star-formation rate surface densities – both $\Sigma_{\text{SFR}}(A_{74})$ and $\Sigma_{\text{SFR}}(R_P)$ – exhibit pronounced trends with V_1 outflow velocity (Figure 14). Both $\Sigma_{\text{SFR}}(A_{74})$ and V_1 and $\Sigma_{\text{SFR}}(R_P)$ and V_1 are correlated at the 2.4σ level with $r_S = -0.40$. Omitting two extremely compact galaxies with uncertain area measurements yields 3.1σ measurements from the null hypothesis and correlation coefficients of $r_S = -0.54$ for both $\Sigma_{\text{SFR}}(A_{74})$ and $\Sigma_{\text{SFR}}(R_P)$. Such strong trends have not yet been reported in the literature at high redshift; Rubin et al. (2010) noted only a 1σ correlation in a sample of 468 galaxies at $0.7 < z < 1.5$, Steidel et al. (2010) also found a 1σ correlation for 81 galaxies at $z \simeq 2$, and Law et al. (2012b) reported a 2.1σ correlation for 35 optically-selected star-forming galaxies at $z = 1.5\text{--}3.6$. However, the galaxy areas employed in the Σ_{SFR} calculations of Rubin et al. (2010), Steidel et al. (2010), and Law et al. (2012b) correspond to half-light radii at rest-frame $\sim 2200 \text{ \AA}$, the extent of $H\alpha$ emission, and circularized effective radii, respectively. Given the clumpy distribution of star formation in distant galaxies (Lotz et al. 2008; Law et al. 2012b), these areas may be overestimates of the regions corresponding to star-formation (Rubin et al. 2010)¹¹. Furthermore, the Steidel et al. (2010) measurements are from ground-based data which are seeing-limited. The Law et al. (2012b) observations, while probing the bulk of the stellar mass with H -band (rest-frame optical) HST imaging, approximated the areas of clumpy galaxies by adopting the circularized effective radius of the brightest clump as representative of the size of the entire galaxy. This technique results in overestimates of Σ_{SFR} , given that the areas of fainter clumps are neglected. In a more local sample of SDSS galaxies at $z \sim 0.1$, Chen et al. (2010) found no correlation between outflow velocity and

Σ_{SFR} . These authors note that the small dynamic range of their data (outflow speed = $[120\text{--}160] \text{ km s}^{-1}$) may obscure trends. When we limit our sample to only objects showing outflows ($V_1 < 0 \text{ km s}^{-1}$), we find that star-formation rate surface density and V_1 are correlated at the $\sim 1\sigma$ level (for both area measurements). We propose that inflows and outflows represent a continuum of gas cycling and therefore correlations with galaxy properties should be investigated inclusive of both redshifted and blueshifted gas. While SFR and $\Sigma_{\text{SFR}}(A_{74})$ are weakly correlated, at the $\sim 2.3\sigma$ level ($r_S = 0.37$), we suggest that the scatter in the V_1 versus $\Sigma_{\text{SFR}}(A_{74})$ relation prevents a similar correlation from being seen in the plot of V_1 versus SFR. All objects with 3σ detections of outflows have $\Sigma_{\text{SFR}}(R_P) > 0.1 M_\odot \text{yr}^{-1} \text{ kpc}^{-2}$, in agreement with the Σ_{SFR} threshold proposed by Heckman (2002). These objects with secure detections of outflows furthermore all have $\text{SFR} > 10 M_\odot \text{yr}^{-1}$, although we hypothesize that the Σ_{SFR} threshold is more fundamental given the stronger correlation of outflow velocity with Σ_{SFR} than with SFR. The trend between outflow velocity and star-formation rate surface density supports the theory that the shifts of absorption lines are due to gas flows as opposed to galactic rotation. The observation that the kinematic shear of $[\text{O II}]$ emission is systematically smaller than the shifts observed in the resonance Fe II lines lends further credence to the assertion that gas flows are primarily responsible for the observed absorption line shifts.

Using the outflow fraction methodology discussed in Section 4.2, we find that $26 \pm 8\%$ of the low- $\Sigma_{\text{SFR}}(A_{74})$ sample shows outflows with blueshifts of at least -40 km s^{-1} . In contrast, $48 \pm 9\%$ of the high- $\Sigma_{\text{SFR}}(A_{74})$ shows outflows at the same level. When the two galaxies with uncertain area measurements are removed from the high- $\Sigma_{\text{SFR}}(A_{74})$ sample, the outflow fraction increases to $54 \pm 9\%$. The significant difference in outflow fraction between the low- and high- $\Sigma_{\text{SFR}}(A_{74})$ samples is consistent

¹¹ Simply overestimating galaxy areas is not sufficient to negate a trend with outflow velocity, however, since we find equally strong correlations with outflow velocity utilizing both $\Sigma_{\text{SFR}}(A_{74})$ and $\Sigma_{\text{SFR}}(R_P)$.

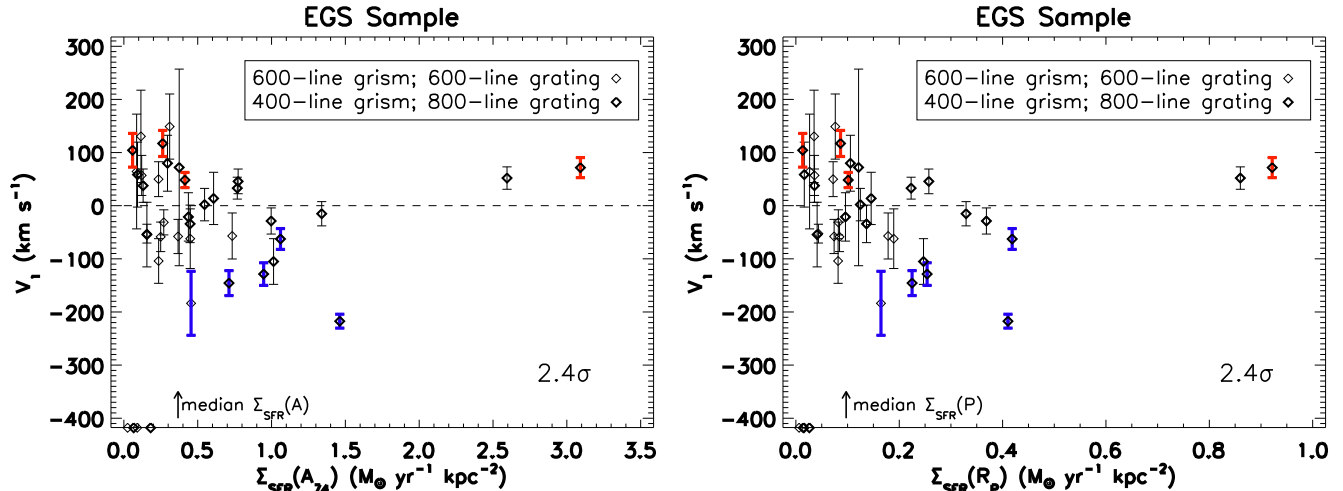


FIG. 14.— *Left*: V_1 outflow velocity versus $\Sigma_{\text{SFR}}(A_{74})$, where symbols are as in Figure 13. A correlation at the 2.4σ level ($r_S = -0.40$) is observed between V_1 and $\Sigma_{\text{SFR}}(A_{74})$, where objects with larger Σ_{SFR} show larger blueshifts in their Fe II lines. *Right*: V_1 outflow velocity versus $\Sigma_{\text{SFR}}(R_P)$. All objects with 3σ detections of outflows have $\Sigma_{\text{SFR}}(R_P) > 0.1 M_\odot \text{ yr}^{-1} \text{ kpc}^{-2}$, in agreement with the Σ_{SFR} threshold proposed by Heckman (2002). A 2.4σ correlation ($r_S = -0.40$) is observed between V_1 and $\Sigma_{\text{SFR}}(R_P)$. When the two outliers at the highest Σ_{SFR} are removed from the sample – objects 12015914 and 12100420 with extremely compact morphologies – trends at the 3.1σ level ($r_S = -0.54$) are observed for both Σ_{SFR} estimates. Law et al. (2012b) observed a 2.1σ correlation between outflow velocity and Σ_{SFR} in a sample of 35 star-forming galaxies at $z \sim 2$, although other authors have noted weaker correlations (Rubin et al. 2010; Steidel et al. 2010).

both with the measurements from individual objects presented above and our findings based on composite spectra, discussed below.

5.1.2. Composite Spectra

We constructed composite spectra from the binary division of data sorted according to SFR, sSFR, $\Sigma_{\text{SFR}}(A_{74})$, $\Sigma_{\text{SFR}}(R_P)$, A_{UV} , and i . We measured the shifts of the Fe II interstellar absorption lines in the composites using the same techniques employed for the individual spectra (Section 4.2). We also measured maximal outflow velocities in both Mg II and Fe II for these composites. While the robustness of the velocity measurements benefit from the increased S/N of the stacked composites, it is important to remember that relying on composite spectra only reveals the global, averaged trends across the sample.

Below, we discuss three measurements for each composite spectrum: V_1 , $V_{\text{max}}(\text{Mg II})$, and $V_{\text{max}}(\text{Fe II})$. While the magnitudes of the V_1 shifts are not large, we emphasize that it is the *difference* in V_1 between composite spectra that is primary interest; the apparent detections of inflows and outflows in individual composites may be spurious given the velocity uncertainties of the LRIS data. The results implied by V_1 and $V_{\text{max}}(\text{Fe II})$ are corroborated by $V_{\text{max}}(\text{Mg II})$, where shifts in the Mg II lines are often visually obvious in the data.

In the top row of Figure 15, we compare high- and low-SFR composites and focus on the wavelength intervals around Fe II and Mg II (2370–2400, 2570–2650, and 2760–2840 Å). The strengths of the Fe II features are similar in both composites, although we find that the high-SFR composite ($\langle \text{SFR} \rangle = 32 M_\odot \text{ yr}^{-1}$; extrema of $[12, 97] M_\odot \text{ yr}^{-1}$) exhibits a V_1 blueshift of $-24 \pm 9 \text{ km s}^{-1}$ while the low-SFR composite ($\langle \text{SFR} \rangle = 7 M_\odot \text{ yr}^{-1}$; extrema of $[1, 11] M_\odot \text{ yr}^{-1}$) is best-fit with a model of redshifted gas with positive velocity $29 \pm 11 \text{ km s}^{-1}$. These

results are in the same sense as the trend of vigorously star-forming objects showing more pronounced outflows than lower SFR systems (Martin 2005). The SFR composites differ significantly in Mg II strength, with larger SFR objects showing deeper absorption on average. The centroids of the Mg II features are blueshifted in both the high- and low-SFR composites, so systemic absorption is not likely responsible for the difference in Mg II strength. Furthermore, the red wings of the 2803 Å features are remarkably similar between the two composites, so it is not immediately apparent that emission filling is affecting one spectrum more than the other. Since SFR and stellar mass are correlated (Figure 8), Mg II strength may depend on stellar mass. We investigate the correlation between Mg II and stellar mass in Section 5.3. Higher metallicities are expected for more vigorously star-forming objects (Tremonti et al. 2004; Noeske et al. 2007; Elbaz et al. 2007), although we note that because the Fe II and Mg II lines are saturated in our study (based on the differences between the observed lines ratios and those expected according to atomic theory) it is difficult to determine if metallicity is the driving factor behind absorption line strength. The kinematics of Mg II are similar in both composites; the high (low) SFR composite has $V_{\text{max}}(\text{Mg II}) = -748 \pm 94$ (-614 ± 83) km s^{-1} . The composites have $V_{\text{max}}(\text{Fe II})$ measurements of -514 ± 84 (-453 ± 104) km s^{-1} .

We compare sSFR composite spectra in the bottom row of Figure 15. As with the SFR composites, there is minimal variation in the strength of the Fe II resonance features between the high- and low-sSFR composites. Likewise, we find differences in the Fe II kinematics between the two composites that are similar to the shifts seen in the SFR composites: objects with high sSFR ($\langle \text{sSFR} \rangle = 1.9 \times 10^{-9} \text{ yr}^{-1}$; extrema of $[1.0 \times 10^{-9}, 5.6 \times 10^{-9}] \text{ yr}^{-1}$) exhibit an average blueshift of $-34 \pm 9 \text{ km s}^{-1}$ while low sSFR objects ($\langle \text{sSFR} \rangle = 4.1$

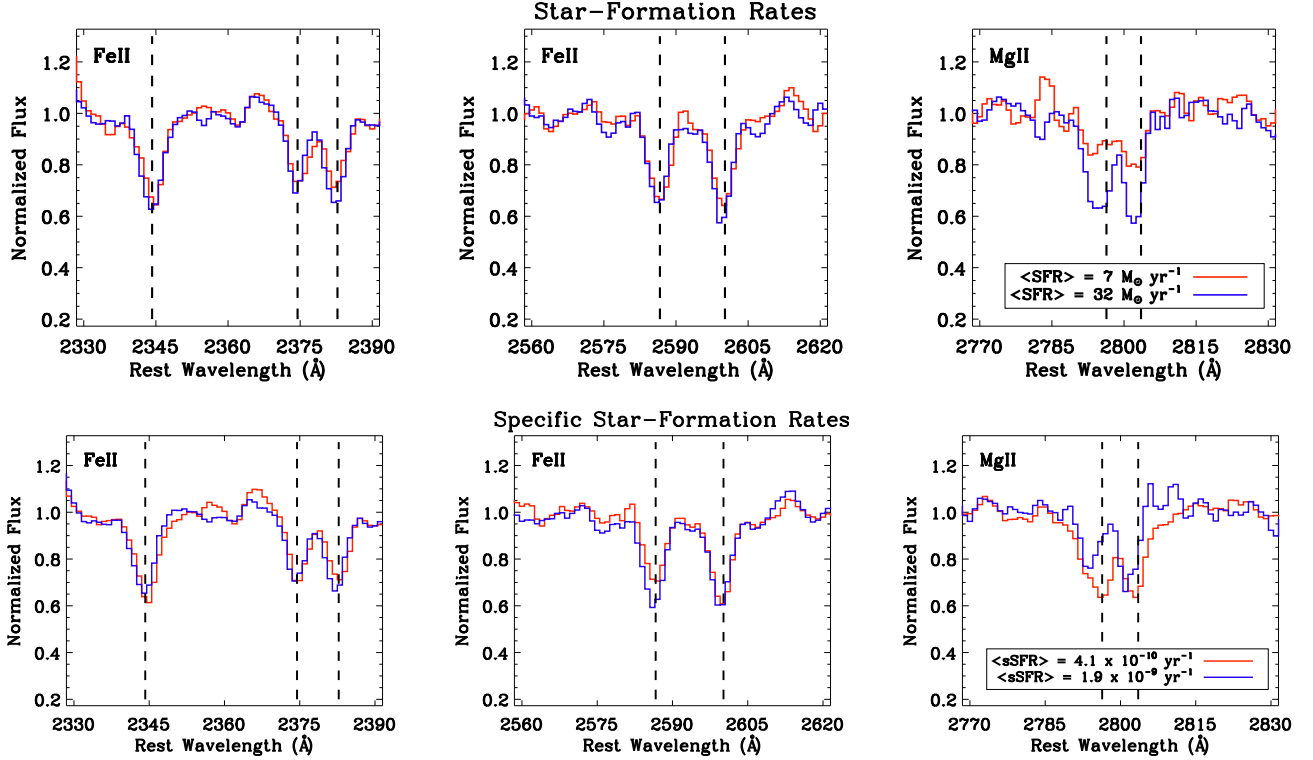


FIG. 15.— *Top*: Composites of high and low SFR objects, where the dashed vertical lines indicate the rest-frame wavelengths of resonance Fe II and Mg II features. We measure V_1 values of -24 ± 9 km s $^{-1}$ for the high-SFR composite (blue line) and 29 ± 11 km s $^{-1}$ for the low-SFR composite (red line). The most pronounced spectral differences between the composites are observed around the Mg II feature at ~ 2800 Å, where higher SFR objects exhibit deeper Mg II absorption troughs on average. *Bottom*: Same as above, for composite spectra assembled from high and low sSFR objects. We measure V_1 values of -34 ± 9 km s $^{-1}$ for the high sSFR composite (blue line) and 27 ± 11 km s $^{-1}$ for the low sSFR composite (red line). As with the SFR composites, the largest spectral differences are seen around Mg II. Objects with high sSFR have bluer Mg II centroids and less Mg II absorption than low sSFR objects. A full discussion of Mg II will appear in forthcoming papers (Kornei et al. 2012b, in prep. and Martin et al. 2012b, in prep.).

$\times 10^{-10}$ yr $^{-1}$; extrema of $[6.5 \times 10^{-11}, 9.6 \times 10^{-10}]$ yr $^{-1}$) are globally characterized by a Fe II shift of 27 ± 11 km s $^{-1}$. The larger blueshifts seen in higher sSFR objects supports the correlation observed in individual galaxies (Figure 13). The sSFR composites are comparable in Mg II strength but not in kinematics: the high (low) sSFR composite has $V_{max}(\text{Mg II}) = -605 \pm 80$ (-834 ± 148) km s $^{-1}$. The composites are characterized by $V_{max}(\text{Fe II})$ measurements of -556 ± 94 (-456 ± 86) km s $^{-1}$. While the sense of the $V_{max}(\text{Mg II})$ measurements is contrary to both the V_1 and $V_{max}(\text{Fe II})$ results – i.e., objects with larger sSFRs show smaller $V_{max}(\text{Mg II})$ blueshifts than objects with lower sSFRs – we note that the $V_{max}(\text{Mg II})$ measurements of the high- and low-sSFR composites are consistent at roughly the 1σ level. The large blueshift of $V_{max}(\text{Mg II})$ for the low-sSFR composite may be explained by high-mass objects preferentially populating the low-sSFR composite. High-mass objects exhibit deeper and broader Mg II absorption profiles than low-mass objects (Martin et al. 2012b, in prep.). Stellar Mg II absorption and emission filling may also affect the observed profiles; the large differences in the red wings of the 2803 Å features and the blueshift seen in the Mg II centroids of the high-sSFR composite argue that emission filling may be present in the high-sSFR composite.

In Figure 16, we plot composite spectra assembled ac-

cording to Σ_{SFR} . Kinematic shifts between the high- and low- Σ_{SFR} composites are visually evident and persist irrespective of which galaxy area measurement is employed. Quantitatively, we find V_1 shifts of -31 ± 7 and -25 ± 6 km s $^{-1}$ for the high $\Sigma_{\text{SFR}}(\text{A}_{74})$ and $\Sigma_{\text{SFR}}(\text{RP})$ composites, respectively. In contrast, the low- Σ_{SFR} composites are best-fit with models having shifts of 44 ± 15 and 33 ± 13 km s $^{-1}$. These results, consistent with the $\sim 3\sigma$ trends observed between outflow velocity and $[\Sigma_{\text{SFR}}(\text{A}_{74}), \Sigma_{\text{SFR}}(\text{RP})]$ on a per-object basis (Figure 14), are in agreement with theoretical predictions that a higher density of star formation should lead to stronger outflows (Leitherer & Heckman 1995; Veilleux et al. 2005; Murray et al. 2011). However, the most striking difference between the Σ_{SFR} composites are the blue wings of the Mg II 2796 Å features. We find visually-obvious shifts in the Mg II doublet between the high- and low- Σ_{SFR} composites, where objects with larger star-formation rate surface densities show more blueshifted Mg II absorption. Furthermore, the entire blue wing of the 2796 Å feature is offset in the composites, suggestive of actual kinematic differences as opposed to centroid shifting from emission filling. The composites of high- Σ_{SFR} objects are characterized by $V_{max}(\text{Mg II}) = -855 \pm 66$ km s $^{-1}$ and -862 ± 69 km s $^{-1}$, respectively. Conversely, the low- Σ_{SFR} composites have measured $V_{max}(\text{Mg II})$ values of -640 ± 117 km s $^{-1}$ and

$-668 \pm 105 \text{ km s}^{-1}$, respectively. The corresponding $V_{max}(\text{Fe II})$ measurements for the high- Σ_{SFR} composites are $-611 \pm 103 \text{ km s}^{-1}$ and $-614 \pm 97 \text{ km s}^{-1}$, respectively. The low- Σ_{SFR} composites have $V_{max}(\text{Fe II})$ values of $-451 \pm 86 \text{ km s}^{-1}$ and $-444 \pm 87 \text{ km s}^{-1}$, respectively. The kinematic differences between the high- and low- Σ_{SFR} composites are among the largest observed for any pair of composites ($\Delta V_{max}(\text{Mg II}) = 215 \pm 134 \text{ km s}^{-1}$ and $194 \pm 126 \text{ km s}^{-1}$; $\Delta V_{max}(\text{Fe II}) = 160 \pm 134 \text{ km s}^{-1}$ and $170 \pm 130 \text{ km s}^{-1}$).

The kinematic differences between Fe II and Mg II in the $\Sigma_{\text{SFR}}(A_{74})$ composites are highlighted in Figure 17. On the left, the Fe II 2374 Å and Mg II 2796 Å lines of the high- $\Sigma_{\text{SFR}}(A_{74})$ composite are overplotted in velocity space. The profiles of Fe II and Mg II absorption are clearly disparate, with the extended blue wing of Mg II indicative of high-velocity gas not traced by Fe II. On the right side of Figure 17, the same Fe II and Mg II transitions are shown for the low- $\Sigma_{\text{SFR}}(A_{74})$ composite. In the regime of low-intensity star formation, the profiles of Fe II and Mg II are much more similar and Mg II does not exhibit an extended blue wing. These results support the association of high star-formation rate surface densities with high-velocity gas, and Mg II is observed to be better tracer of high-velocity gas than Fe II. In order to better study the trend between outflow velocity and Σ_{SFR} , we constructed composite spectra from three bins of $\Sigma_{\text{SFR}}(A_{74})$. We find that the V_1 , $V_{max}(\text{Fe II})$, and $V_{max}(\text{Mg II})$ measurements are all correlated with $\Sigma_{\text{SFR}}(A_{74})$, where objects characterized by higher intensities of star formation have larger centroid and maximal outflow velocities (Figure 18). We observe that $V_{max}(\text{Fe II})$ is a smooth function of $\Sigma_{\text{SFR}}(A_{74})$, while $V_{max}(\text{Mg II})$ appears to reach a maximum at $\Sigma_{\text{SFR}}(A_{74}) = 0.4 \text{ M}_{\odot} \text{ yr}^{-1} \text{ kpc}^{-2}$. The relatively coarse pixel sampling of the composite spectra $\sim 100 \text{ km s}^{-1}$ is likely responsible for the plateau of $V_{max}(\text{Mg II})$ values. From the composite spectra, it is evident that the equivalent width of blueshifted Mg II absorption steadily increases with increasing $\Sigma_{\text{SFR}}(A_{74})$.

As previous observations have shown stronger interstellar absorption lines with increasing dust attenuation (Shapley et al. 2003), indicative of an association between absorbing outflow material and dust, we investigated the relationship between A_{UV} and outflow velocity. In composite spectra assembled on the basis of A_{UV} (Figure 19), we find that objects with higher dust attenuation exhibit marginally stronger Fe II absorption lines (especially in the 2344 Å feature) and significantly stronger Mg II absorption. These results support the correlation found by Shapley et al. (2003), where these authors observed that more attenuated Lyman Break Galaxies (LBGs) at $z \sim 3$ showed deeper interstellar absorption lines. We find that objects with a variety of attenuation levels exhibit similar Fe II kinematics (Figure 19); the centroids of the Fe II lines in the high- A_{UV} composite ($\langle A_{\text{UV}} \rangle = 2.7$; extrema = [1.7, 4.2]) are best-fit with a velocity shift of $-3 \pm 10 \text{ km s}^{-1}$ while the low- A_{UV} composite ($\langle A_{\text{UV}} \rangle = 1.1$; extrema = [0.0, 1.7]) shows a shift of $-10 \pm 9 \text{ km s}^{-1}$. These measurements are both consistent with no velocity shift. The $V_{max}(\text{Fe II})$ measurements of the composites are consistent with each other

within their 1σ errors ($-497 \pm 88 \text{ km s}^{-1}$ for the high- A_{UV} composite and $-522 \pm 91 \text{ km s}^{-1}$ for the low- A_{UV} composite). Law et al. (2012b) find only a 0.7σ correlation between outflow velocity and E(B-V) in a sample of 35 star-forming galaxies at $z \sim 2$. Within a sample of local SDSS galaxies, Chen et al. (2010) also find no evidence that attenuation level is linked to outflow velocity.

While the Fe II features of the two A_{UV} composites show only minimal variation in strength and kinematics, the Mg II features are strikingly different between the high- and low- A_{UV} composites. We find that more attenuated objects have deeper Mg II absorption troughs (consistent with a relative lack of emission filling or stronger absorption in dusty galaxies), Mg II centroids roughly consistent with the systemic velocity, and $V_{max}(\text{Mg II}) = -732 \pm 71 \text{ km s}^{-1}$ while objects with lower A_{UV} have weaker absorption profiles, more strongly blueshifted centroids, and $V_{max}(\text{Mg II}) = -652 \pm 89 \text{ km s}^{-1}$. Prochaska et al. (2011) proposed outflow models in which dust has a pronounced effect on observed wind profiles: resonantly trapped photons (i.e., those arising from the Mg II transitions at 2796 and 2803 Å) have an increased probability of being absorbed by dust given their longer path lengths. Our observations support this hypothesis that Mg II should show more variation with changing A_{UV} levels than the Fe II transitions that are not resonantly trapped. However, Prochaska et al. (2011) note that extreme levels of extinction ($\tau_{\text{dust}} \sim 10$) are necessary in order to measure qualitative changes in line profiles, although we see this effect at significantly lower attenuation levels ($\tau_{\text{dust}} \sim 2$).

5.2. Trends with Inclination and Morphology

Observations of local starbursts have shown extraplanar outflows emanating perpendicular to galaxy disks (e.g., Heckman et al. 1990; Lehnert & Heckman 1996; Cecil et al. 2001; Strickland & Heckman 2009). If this geometry persists at higher redshifts, one would expect the measured outflow velocities in the sample to depend strongly on inclination as the wind becomes increasingly oriented toward the observer. Studies to date have primarily focused on testing this hypothesis in local samples, given the advantages of apparent magnitude and spatial resolution. Chen et al. (2010) used a sample of $\sim 150,000$ SDSS galaxies and assembled stacks of the Na D absorption lines on the basis of galaxy inclination measured from two dimensional de Vaucouleurs (1948) fits to *ugriz* data. These authors found a striking correlation of increasing outflow velocity with decreasing inclination, consistent with the physical picture of winds escaping perpendicular to galaxy disks. Similarly, Heckman et al. (2000) observed 18 local starbursts in the Na D lines and measured an increase in the fraction of objects exhibiting outflows when the sample was restricted to objects with $i \leq 60^\circ$. In the high-redshift regime, Weiner et al. (2009) examined 118 galaxies at $z = 1.4$ with *HST I*-band imaging and extracted minor-to-major axis ratios (b/a) using SExtractor (Bertin & Arnouts 1996). These authors did not find a correlation between axis ratio and wind strength or outflow velocity; Weiner et al. (2009) propose that the uncertainties on the axis ratios of small, irregular galaxies imaged in the rest-frame *U*-band may be substantial. Law et al. (2012b) looked at 35 optically-

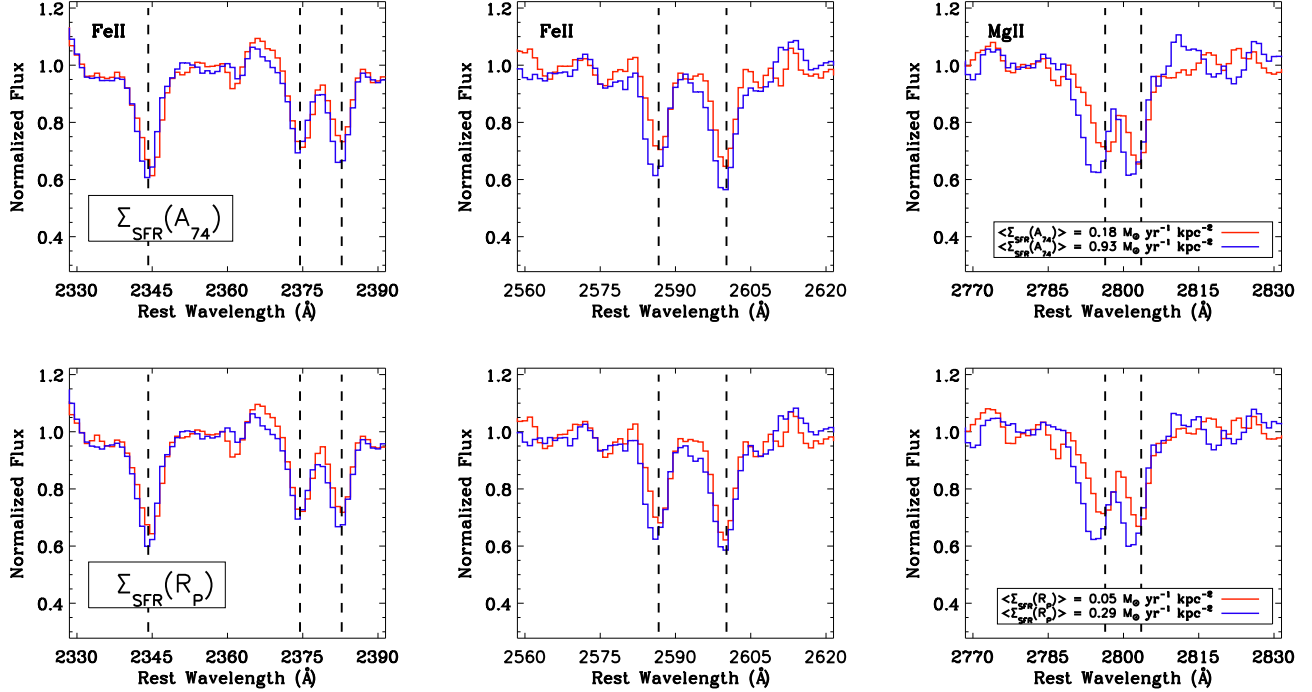


FIG. 16.— *Top*: Composite spectra assembled on the basis of $\Sigma_{\text{SFR}}(A_{74})$. Kinematic shifts between the two composites in the Fe II resonance lines are evident visually; we find a V_1 outflow velocity of $-31 \pm 7 \text{ km s}^{-1}$ for the high- $\Sigma_{\text{SFR}}(A_{74})$ composite (blue line) and $44 \pm 15 \text{ km s}^{-1}$ for the low- $\Sigma_{\text{SFR}}(A_{74})$ composite (red line). These pronounced differences are consistent with the strong trend observed between $\Sigma_{\text{SFR}}(A_{74})$ and V_1 on a per-object basis (Figure 14). The Mg II features show a strong kinematic shift between the composites, with objects characterized by larger Σ_{SFR} exhibiting more blueshifted Mg II absorption. *Bottom*: Same as above, for $\Sigma_{\text{SFR}}(R_P)$ composites. The high- $\Sigma_{\text{SFR}}(R_P)$ composite is best-fit with a V_1 outflow velocity of $-25 \pm 6 \text{ km s}^{-1}$ while the low- $\Sigma_{\text{SFR}}(R_P)$ composite yields an outflow velocity of $33 \pm 13 \text{ km s}^{-1}$. Objects with higher $\Sigma_{\text{SFR}}(R_P)$ also show more strongly blueshifted Mg II features. These results are in the same sense as the trends seen in the $\Sigma_{\text{SFR}}(A_{74})$ composites, unsurprising given the multiplicative offset between the A_{74} and πR_P^2 areas (Figure 9).

selected star-forming galaxies at $z = 1.5\text{--}3.6$ with b/a estimated from GALFIT (Peng et al. 2002, 2010) modeling of *HST* F160W imaging and also found no correlation between outflow velocity and b/a . It is important to note that these results at high redshift are much more uncertain than the Chen et al. (2010) and Heckman et al. (2000) findings, given the very different spatial resolutions achievable at $z = 0$ and $z \sim 2$. Furthermore, while b/a and inclination are often presumed to be related by $i = \cos^{-1}[b/a]$ (Tully & Fisher 1977), Law et al. (2012b) caution that this conversion relies on the thin-disk approximation which may not be valid for star-forming galaxies with significant vertical velocity dispersions (Law et al. 2009; Förster Schreiber et al. 2009). However, in the absence of a significant sample of high-redshift galaxies for which spatially-resolved velocity dispersions have been measured, this simple conversion continues to be employed. As some of the objects in our sample furthermore resemble local star-forming disks more closely than the clumpy, irregular galaxies at $z \sim 2$ with large vertical velocity dispersions, the thin-disk approximation may not be a gross assumption here.

We investigate the relationship between galaxy inclination and outflow velocity using inclinations estimated from SExtractor (Bertin & Arnouts 1996) axial measurements of summed *HST* $V+I$ detection images. In Figure 20, we plot outflow velocity versus inclination. While inclination estimates for individual objects are likely uncertain by $\sim 10^\circ$ due to measurement error in the rest-frame

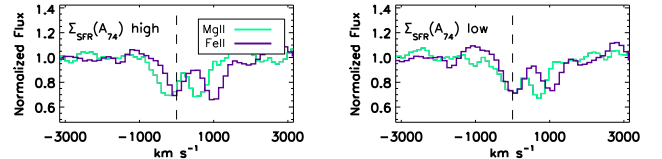


FIG. 17.— Comparison of Fe II 2374 and Mg II 2796 profiles in velocity space, for the high and low $\Sigma_{\text{SFR}}(A_{74})$ composite spectra. Note the pronounced variation between the blue wings of the features in the high $\Sigma_{\text{SFR}}(A_{74})$ composite; $V_{\text{max}}(\text{Mg II})$ is $-855 \pm 66 \text{ km s}^{-1}$ while $V_{\text{max}}(\text{Fe II})$ is $-611 \pm 103 \text{ km s}^{-1}$. High $\Sigma_{\text{SFR}}(A_{74})$ systems show gas at high velocity, and this gas is better traced by Mg II than by Fe II (Section 6). The absorption features at $\sim +770$ and $\sim +1000 \text{ km s}^{-1}$ are Mg II 2803 and Fe II 2382, respectively.

UV, highlighting the objects showing $\geq 3\sigma V_1$ outflows reveals that all such five objects have $i < 45^\circ$. When we make a simple division of the data at $i = 45^\circ$, we additionally find that the sample of more edge-on systems has $\langle V_1 \rangle = 4 \pm 15 \text{ km s}^{-1}$ while the sample of predominantly face-on systems is characterized by $\langle V_1 \rangle = -28 \pm 20 \text{ km s}^{-1}$. These results are consistent with the physical picture of a biconical wind profile where outflowing material preferentially emanates perpendicular to the galactic disk. Weiner et al. (2009) investigated the relationship between outflow velocity and galaxy inclination at $z \sim 1.4$ using *HST* imaging, although these authors relied on observations in a single band (I). The Weiner et al. (2009) imaging data are accordingly shallower than ours by a factor $\sim \sqrt{2}$, although we propose that the main

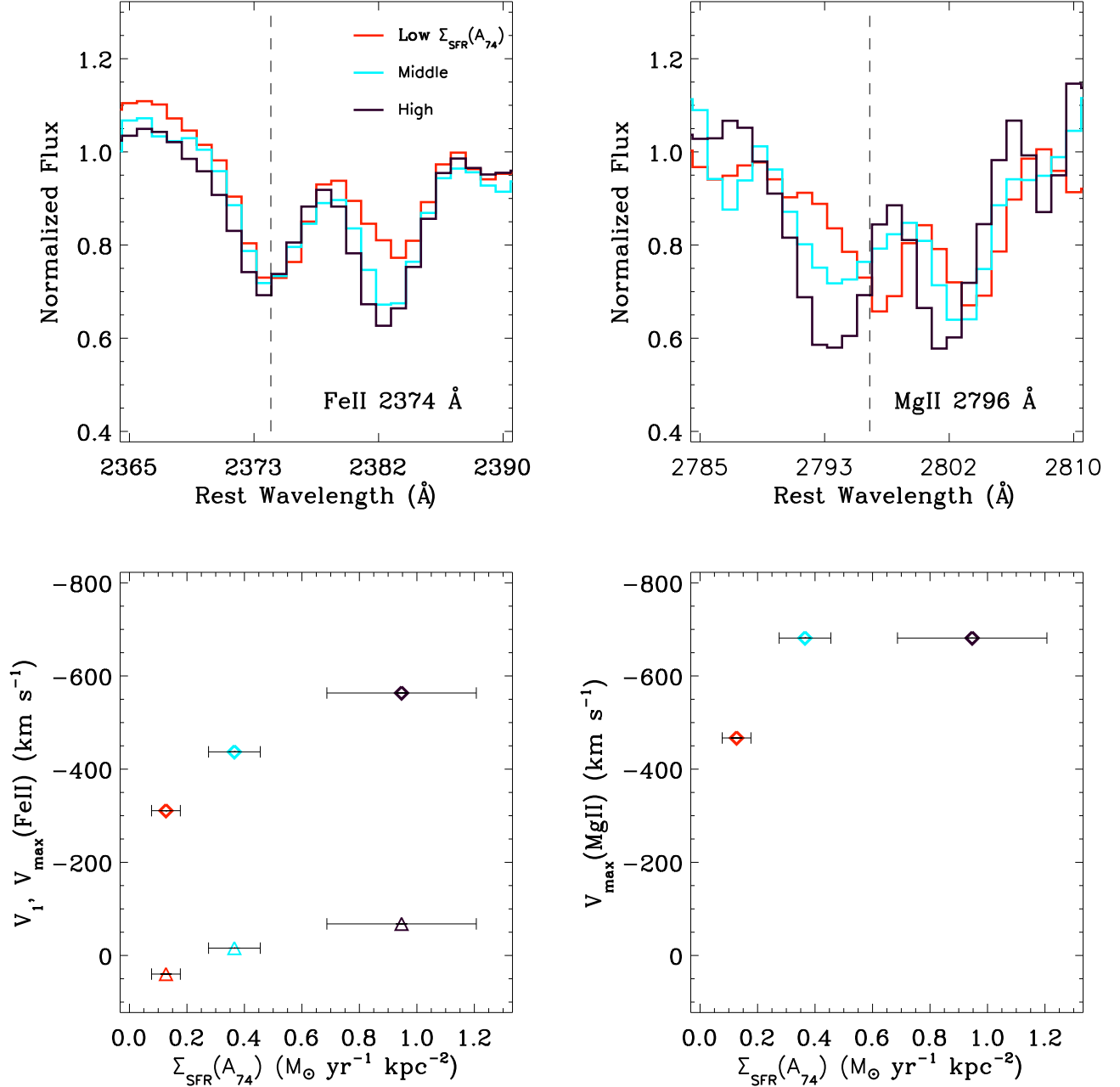


FIG. 18.— *Top*: The regions around Fe II 2374 Å and Mg II 2796 Å are shown for three composite spectra assembled from data ordered by $\Sigma_{\text{SFR}}(A_{74})$. With increasing Σ_{SFR} , the blue wings of both the Fe II and Mg II features extend to larger velocities. This is evidence of the increasing prevalence of high velocity gas with larger Σ_{SFR} . *Bottom*: We quantify the blue wings of Fe II and Mg II with $V_{\text{max}}(\text{Fe II})$ and $V_{\text{max}}(\text{Mg II})$ measurements. The left panel shows $V_{\text{max}}(\text{Fe II})$ (diamonds) and V_1 (triangles) versus $\Sigma_{\text{SFR}}(A_{74})$, where the error bars on $\Sigma_{\text{SFR}}(A_{74})$ indicate the 1σ dispersion in each bin. The right panel shows the relationship between $V_{\text{max}}(\text{Mg II})$ and $\Sigma_{\text{SFR}}(A_{74})$. In all cases, more extended wing profiles tracing higher velocity gas are seen in systems with larger star-formation rate surface densities.

reason we find a correlation between inclination and outflow velocity while Weiner et al. (2009) do not lies in the relative S/N ratios of our respective spectroscopic data. The individual spectra used by Weiner et al. (2009) have a S/N of ~ 1 per resolution element near 2820 Å. Conversely, the spectra presented in this paper have a S/N of ~ 11 per resolution element in the vicinity of the Fe II lines. The co-added spectra employed by Weiner et al. (2009) for the majority of their analyses (although not inclination) have S/N of 16–28 per resolution element,

while the spectral stacks used in this paper have S/N of 49–68 per resolution element.

We also utilized the statistical power of our sample in assembling composite spectra of high- and low-inclination objects, where $\langle i \rangle = 58^\circ$ and 38° , respectively. In Figure 21, we compare these composite spectra and show thumbnails of the ten highest (lowest) inclination objects below (above) the composite spectra for visual reference. While the magnitude of the shifts with respect to systemic velocity are small in both cases, we do find

that galaxies with lower inclinations exhibit bluer Fe II absorption troughs ($V_1 = -19 \pm 9 \text{ km s}^{-1}$) than more inclined galaxies ($V_1 = 28 \pm 11 \text{ km s}^{-1}$), qualitatively consistent with the results of Chen et al. (2010). Similarly, objects with lower inclinations show more blueshifted Mg II lines ($V_{max}(\text{Mg II}) = -811 \pm 140 \text{ km s}^{-1}$) than more edge-on systems ($-692 \pm 95 \text{ km s}^{-1}$). Likewise, the composite of lower (higher) inclination systems are characterized by $V_{max}(\text{Fe II}) = -557 \pm 101$ (-464 ± 77) km s^{-1} .

The morphology of star-forming galaxies hosting outflows has only recently been investigated (Martin 2005; Sato et al. 2009; Weiner et al. 2009; Rubin et al. 2010; Law et al. 2012b). In the local universe, there is an implicit bias toward concluding that outflows are preferentially hosted by mergers. As systems with large SFRs are more likely to exhibit outflows (Martin 2005; Rupke et al. 2005) and local galaxies with vigorous star formation are often characterized by disrupted morphologies indicative of either major or minor mergers (e.g., Sanders & Mirabel 1996), an association between mergers and outflows naturally develops. In a study by Martin (2005) of 18 ULIRGs at $0.04 < z < 0.16$ characterized by merger signatures, these authors found evidence for neutral gas outflows in 15 systems ($> 80\%$), consistent with Rupke et al. (2005). At larger redshifts, where vigorous star formation and merger morphology appear to be decoupled (Law et al. 2007; Swinbank et al. 2010), Sato et al. (2009) still found that outflows traced by Na D were preferentially hosted by galaxies undergoing mergers.

We use our sample of $z \sim 1$ objects to study the prevalence of outflows in systems with large star-formation rates but a wide range of morphologies. We use quantitative morphological parameters from Lotz et al. (2004) to investigate the light distributions of galaxies hosting outflows. We employ the Gini coefficient (G) and the second order moment of the brightest 20% of each galaxy’s flux, M_{20} . Figure 22 shows how objects in (G , M_{20}) space divide into classical early-type (E/S0/Sa), late-type (Sb–Irr), and merger candidates (Lotz et al. 2008). We find that objects exhibiting outflows and inflows span (G , M_{20}) morphological parameter space; systems classified as mergers do not appear to drive winds any more frequently than galaxies classified as E/S0/Sa or Sb–Irr. Objects with G , M_{20} values indicative of mergers, in fact, qualitatively host a relative dearth of outflows and inflows compared with other morphological classes. Both Weiner et al. (2009) and Rubin et al. (2010) also found no trend between morphology and outflows in populations of star-forming galaxies.

Law et al. (2012b) studied the prevalence of outflows with galaxy size. These authors parameterized size using both the half-light radius along the semi-major axis (r) and the circularized effective radius ($r_e = r\sqrt{b/a}$). Law et al. (2012b) found a $> 2\sigma$ correlation with both size estimates, where the smallest galaxies exhibited the largest interstellar blueshifts with respect to the systemic frame defined by $H\alpha$. In Figure 23, we use our data to plot outflow velocity versus two size estimates: Petrosian radius and $(A_{74}/\pi)^{1/2}$ (the “radius” of the A_{74} area). We show the best-fit line derived by Law et al. (2012b), $V = 77r - 342 \text{ km s}^{-1}$, for reference, but note that only

$\sim 40\%$ of our sample has Petrosian radii falling in the same range as the Law et al. (2012b) data. We find no evidence for a correlation between outflow velocity and either Petrosian radius or $(A_{74}/\pi)^{1/2}$.

5.3. Mg II Equivalent Width & Kinematics

Motivated by the range of Mg II absorption strengths observed in the sample, we investigated the primary driver of Mg II equivalent width. We estimated the equivalent width of Mg II by summing flux over the interval 2788–2810 Å, thereby encompassing both features of the Mg II doublet. We tested the correlation between Mg II equivalent width and SFR, stellar mass, sSFR, A_{UV} , $U-B$ color, $\Sigma_{\text{SFR}}(A_{74})$, $\Sigma_{\text{SFR}}(R_P)$, and inclination, respectively (Figure 24). Consistent with Martin et al. (2012), we find that stellar mass and Mg II equivalent width are the most strongly correlated, at the 4.5σ level ($r_S = 0.61$). Bordoloi et al. (2011) also note the correlation between Mg II equivalent width and stellar mass in a sample of COSMOS galaxies at $0.5 < z < 0.9$. Stellar Mg II absorption may be present in objects with large stellar masses; population modeling is necessary in order to definitively address the contribution of stellar absorption.

Among the SFR, sSFR, and A_{UV} composite spectra, we find two families based on the strength and kinematics of Mg II. The low-SFR, high-sSFR, and low- A_{UV} composite spectra exhibit weaker, blueshifted Mg II features with little absorption in the red wings of the lines. On the other hand, the low-sSFR and high- A_{UV} composite spectra show stronger Mg II absorption at roughly the systemic velocity, with substantial absorption in the lines’ red wings. The high-SFR composite spectrum, with its strong, blueshifted Mg II absorption, is anomalous in that appears to be included in both families. We note that the differences in the Mg II profiles of these SFR, sSFR, and A_{UV} composite spectra are mainly limited to the red wings of the lines and are distinct from the shifting of the blue wings and centroids observed in the $\Sigma_{\text{SFR}}(A_{74})$ and $\Sigma_{\text{SFR}}(R_P)$ composite spectra. We propose that objects in the low-SFR, high-sSFR, and low- A_{UV} composite spectra are dominated by emission filling while the galaxies populating the low-sSFR and high- A_{UV} composite spectra experience significant systemic absorption. Furthermore, since stellar mass is correlated with SFR, sSFR, and A_{UV} , the variation in Mg II properties seen in the SFR, sSFR, and A_{UV} composite spectra may reflect the primary correlation between stellar mass and Mg II equivalent width. Accordingly, the low-SFR, high-sSFR, and low- A_{UV} composite spectra are preferentially populated with low-mass objects with weaker Mg II absorption (Martin et al. 2012). Higher mass objects may have more absorption and also less emission filling. Lower levels of emission filling indicate attenuation by dust, which may be more prevalent in higher mass objects. Future work involving modeling of the stellar component of Mg II absorption will help illuminate the connection between Mg II and stellar populations.

6. DISCUSSION

In this section, we present a discussion and interpretation of our results. We observe the strongest trend between outflow velocity and Σ_{SFR} , a finding that is supported both by theoretical work and also by observations

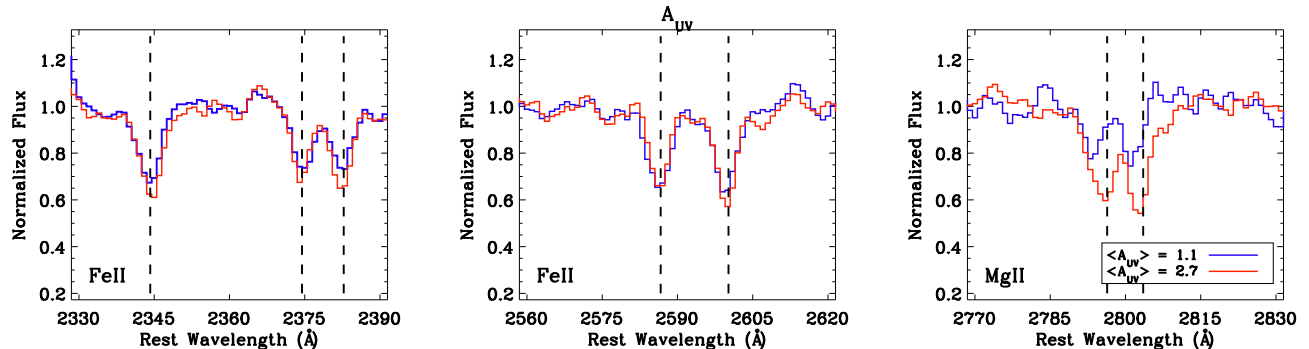


FIG. 19.— Composite spectra assembled on the basis of A_{UV} . Fitting the Fe II resonance absorption lines yields a V_1 outflow velocity of -3 ± 10 km s $^{-1}$ for the high- A_{UV} composite (red line) and -10 ± 9 km s $^{-1}$ for the low- A_{UV} composite (blue line). Mg II strength and kinematics are clearly correlated with A_{UV} , where less attenuated objects show shallower Mg II absorption troughs and more blueshifted features. In dusty objects, the lack of emission filling in the Mg II features likely contributes to the observed absorption depth. These results are consistent with the trends observed for individual objects (Figure 24).

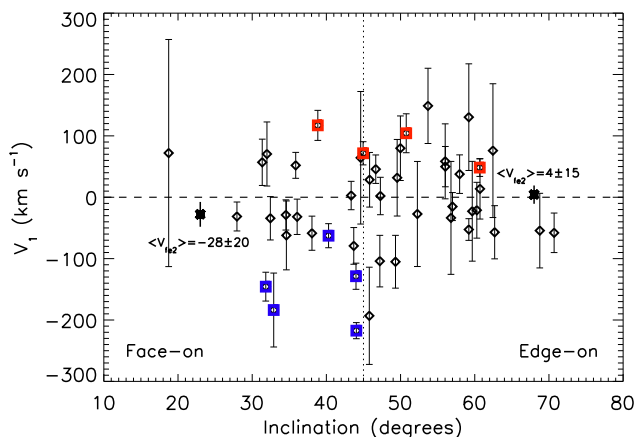


FIG. 20.— V_1 outflow velocity versus galaxy inclination, where inclination was estimated from axial ratios: $i = \cos^{-1}[b/a]$ (Tully & Fisher 1977). Significant detections of outflows or inflows at the 3σ level are highlighted in blue and red, respectively. While individual inclination measurements are likely uncertain by $\sim 10^\circ$ due to measurement error in the rest-frame UV, we note that a simple division of the sample at $i = 45^\circ$ yields a subgroup of more face-on galaxies with $\langle V_1 \rangle = -28 \pm 20$ km s $^{-1}$ and a set of more inclined galaxies with $\langle V_1 \rangle = 4 \pm 15$ km s $^{-1}$. These findings are in the same sense as the results of Chen et al. (2010), who observed a correlation between outflow velocity and inclination in a sample of $\sim 150,000$ local SDSS (York et al. 2000) galaxies such that more face-on systems showed a stronger outflow component.

at lower redshifts. We discuss the prevalence of outflows in the sample and consider the uncertainties of using different tracer species and measurement diagnostics to parameterize a single characteristic outflow velocity.

6.1. Outflow Velocity and the Star-Formation Rate Surface Density

Our finding of a strong correlation between outflow velocity and the *concentration* of star formation – as opposed to the global SFR – is consistent with previous observations. In a sample of star-forming galaxies at $z = 1.5$ – 3.6 , Law et al. (2012b) reported a 2.1σ correlation between outflow velocity and Σ_{SFR} . At a comparable redshift, Genzel et al. (2011) used SINFONI observations of five galaxies to measure a higher incidence of broad H α profiles in star-forming clumps with larger H α surface brightnesses. Since broad wings are indica-

tive of gas moving at high velocities and larger H α surface brightnesses can be directly linked to larger star-formation rate surface densities, these authors posit that their results may be evidence for galactic winds being modulated by the intensity of star formation. The lack of broad H α components in fainter interclump regions of the Genzel et al. (2011) sample furthermore suggests that winds may require some threshold Σ_{SFR} . Similarly, in a sample of ~ 50 galaxies at $z = 1.2$ – 2.6 with high H α surface brightnesses, Le Tiran et al. (2011) found that systems with the highest star-formation rate surface densities were more likely to exhibit a broad H α component. In searching for a physical explanation for the incidence of broad H α kinematics, which are interpreted as arising in outflowing gas, Le Tiran et al. (2011) used the ratio of [S II] 6716 / [S II] 6731 to infer electron densities (Osterbrock 1989). Based on conversions between electron density and thermal pressure, these authors found that the systems with the highest star-formation intensities were characterized by pressures similar to the values found in local starbursts exhibiting galactic winds (e.g., Lehnert & Heckman 1996). Le Tiran et al. (2011) accordingly proposed that thermal pressure may modulate the incidence of galactic winds.

In addition to thermal pressure arising from the hot gas expelled by supernovae, radiation pressure on dust grains is also commonly invoked as a mechanism for driving galactic winds (e.g., Socrates et al. 2008; Murray et al. 2011). When dust grains experience a force from impinging photons, the cool gas that is coupled to the dust is also accelerated. Several authors have examined the relative contributions of thermal and radiation pressure in driving galactic winds. Murray et al. (2011) propose that radiation pressure is the primary driver lofting gas clouds above the galactic disk in the first ~ 4 Myr before supernovae explode. These authors hypothesize that a critical gas surface density is required to provide the initial radiation pressure to accelerate the gas cloud above the galactic disk. Once a bubble of gas is sufficiently separated from the galactic plane, ram pressure from the hot winds of later generations of supernovae accelerates the gas (with a force comparable to the force from radiation pressure; Murray et al. 2005) above the galactic disk. The predicted scaling relation between outflow velocity and the SFR due to ram pressure alone is shallow: $V \propto \text{SFR}^{1/5}$ (Ferrara & Ricotti 2006) or V

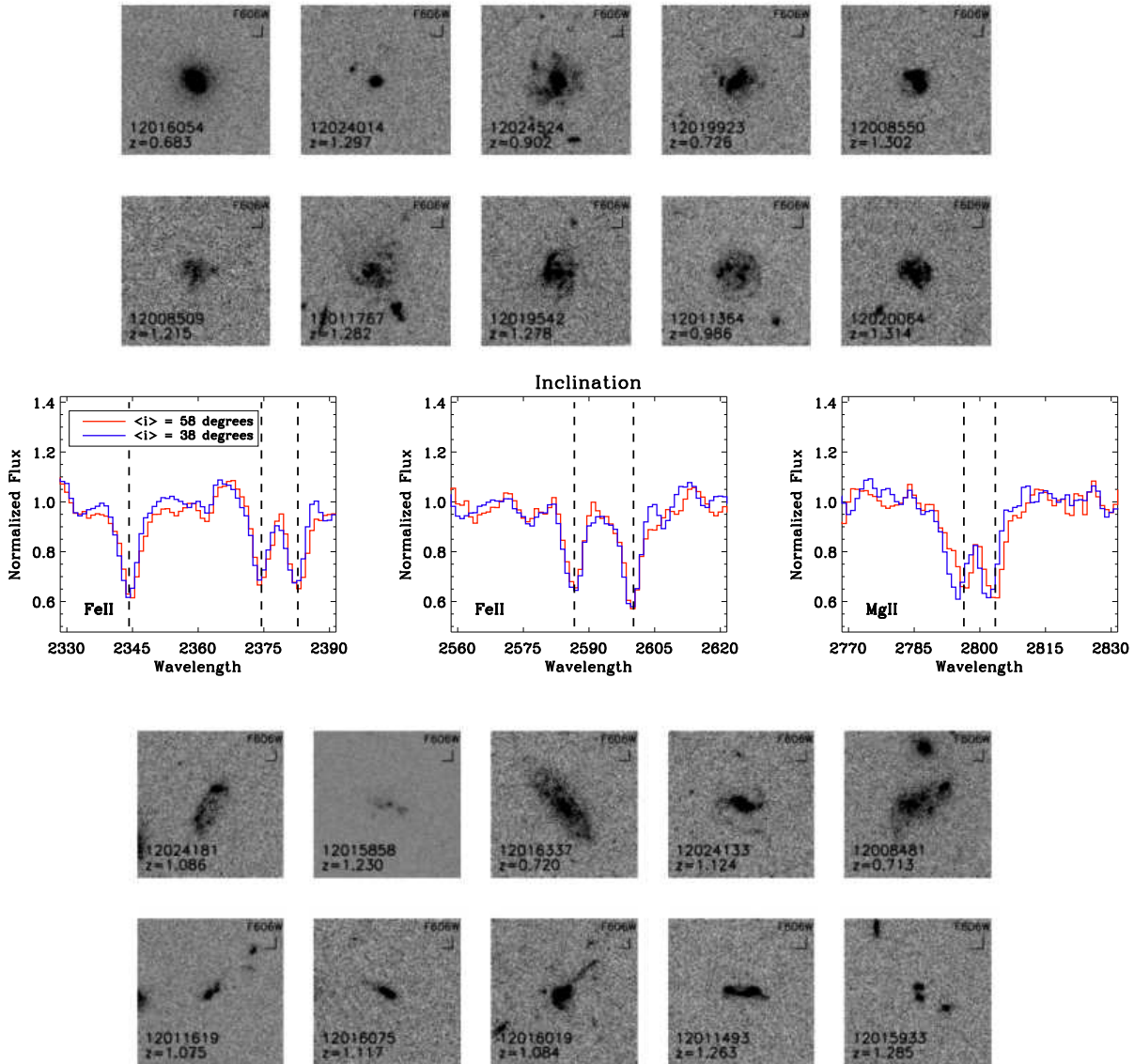


FIG. 21.— Composite spectra assembled from objects with high and low inclinations, respectively, where inclinations were estimated from *HST* *V+I* band imaging assuming intrinsic circular disks: $i = \cos^{-1}[b/a]$ (Tully & Fisher 1977). We find that the composite spectrum composed of high inclination objects (red line) is best-fit with $V_1 = 28 \pm 11 \text{ km s}^{-1}$ while the composite spectrum assembled from low inclination galaxies (blue line) has a V_1 outflow velocity of $-19 \pm 9 \text{ km s}^{-1}$. Even though the overall shifts of each composite from 0 km s^{-1} are small in magnitude, the kinematic difference between the two composites is significant. These results are consistent with the trend of stronger blueshifts with decreasing inclination, as noted by Chen et al. (2010) for a local sample of SDSS galaxies. *V*-band thumbnails of the ten lowest and highest inclination objects are shown above and below the composite spectra, respectively.

$\propto \text{SFR}^{1/4}$ (Heckman et al. 2000). On the other hand, for a purely radiatively driven wind, the outflow velocity is expected to scale roughly linearly with the SFR (Sharma & Nath 2012). Using data from the $z \sim 3$ LBG study of Shapley et al. (2003), Ferrara & Ricotti (2006) find a scaling relation between SFR and outflow velocity of the form $V \propto \text{SFR}^{2/3}$. However, these authors make the assumption that outflow velocity can be calculated from the velocity difference between interstellar absorption lines and $\text{Ly}\alpha$ emission. As $\text{Ly}\alpha$ is resonantly scattered and often observed to be redshifted by several hundred km s^{-1} relative to the systemic velocity frame defined by $\text{H}\alpha$ emission (Steidel et al. 2010), the outflow velocities employed by Ferrara & Ricotti (2006)

may very well be overestimates. Indeed, analysis of the Shapley et al. (2003) data reveals that composite spectra differing in SFR have nearly identical gas kinematics as traced by interstellar absorption lines alone. The Ferrara & Ricotti (2006) conclusion that outflow velocity and SFR are related via the form $V \propto \text{SFR}^{2/3}$ is primarily driven by kinematic changes in $\text{Ly}\alpha$ as opposed to true variation in the interstellar species tracing the wind. The Shapley et al. (2003) data suggest that outflow velocity varies much more weakly, if at all, with SFR. Observations by Martin (2005) ($V \propto \text{SFR}^{0.35}$) are not grossly inconsistent with the $\text{SFR}^{1/5}$ scaling predicted by Ferrara & Ricotti (2006) for acceleration by ram pressure alone, although various authors have suggested that

galactic winds are likely accelerated by a combination of radiative and ram pressures (Sharma & Nath 2012; Murray et al. 2011). We do not find a significant trend of outflow velocity with SFR, although we note that the relatively low resolution of our data paired with the limited range of SFRs probed may preclude a robust measurement of a trend, particularly if the scaling is shallow.

As discussed in Genzel et al. (2011), the efficiency of radiation pressure in driving galactic winds can be linked to the surface density of star formation (i.e., Σ_{SFR}) via simple heuristic arguments. Environments with higher star-formation rate surface densities have higher gas surface densities (Kennicutt 1998). Gas surface density, in turn, is correlated with the dust surface density and, analogously, the dust opacity. The radiation force on dust grains, \dot{p}_{rad} , is more efficient in dustier environments ($\dot{p}_{\text{rad}} \propto \tau L/c$, where τ is the optical depth to radiation, L is the bolometric luminosity, and c is the speed of light; Veilleux et al. 2005). As systems with higher star-formation rate surface densities will produce more radiation to begin with (having a larger concentration of star formation), it is expected that the combination of higher radiation levels and the efficient radiative coupling found in high Σ_{SFR} environments – due to larger concentrations of dust – will translate into effective driving of galactic winds. In the sample discussed here, however, we do not find that dustier systems show stronger outflows; the high- and low- A_{UV} composite spectra have V_1 , $V_{\text{max}}(\text{Fe II})$, and $V_{\text{max}}(\text{Mg II})$ values consistent at the 1σ level. This null result may indicate that radiation pressure does not dominate the acceleration of galactic winds, or that our dataset is simply too limited in size and S/N to unambiguously detect a trend between A_{UV} and outflow velocity.

Several authors have estimated the form of the scaling relation between Σ_{SFR} and outflow velocity. In the context of outflows being driven from disrupted giant molecular clouds, Murray et al. (2011) parameterize the ejection velocity of gas due to radiation pressure as proportional to the square of the gas surface density, Σ_g :

$$v_{ej} \propto \frac{R_d^2 \Sigma_g^2}{v_c^2} \quad (4)$$

where v_{ej} is the ejection velocity (assumed to be analogous to the outflow velocity), R_d is the galaxy disk radius, and v_c is the galaxy circular velocity. Assuming the Kennicutt-Schmidt (1998) star-formation law has the form $\Sigma_{\text{SFR}} \propto \frac{\Sigma_g}{\tau_{\text{dyn}}}$, where τ_{dyn} is the dynamical timescale (R_d/v_c), Murray et al. (2011) alternatively express v_{ej} as proportional to the square of the star-formation rate surface density:

$$v_{ej} \propto \frac{R_d^4 \Sigma_{\text{SFR}}^2}{v_c^4}. \quad (5)$$

The additional terms corresponding to R_d and v_c may translate into scatter in the $v_{ej} - \Sigma_{\text{SFR}}$ relation; using our estimates of the Petrosian radius and the width of the [OII] emission feature as proxies for R_d and v_c , respectively, we find that τ_{dyn} spans a factor of ~ 30 in our sample. Murray et al. (2011) also derive a critical surface density of star formation required to launch a galactic

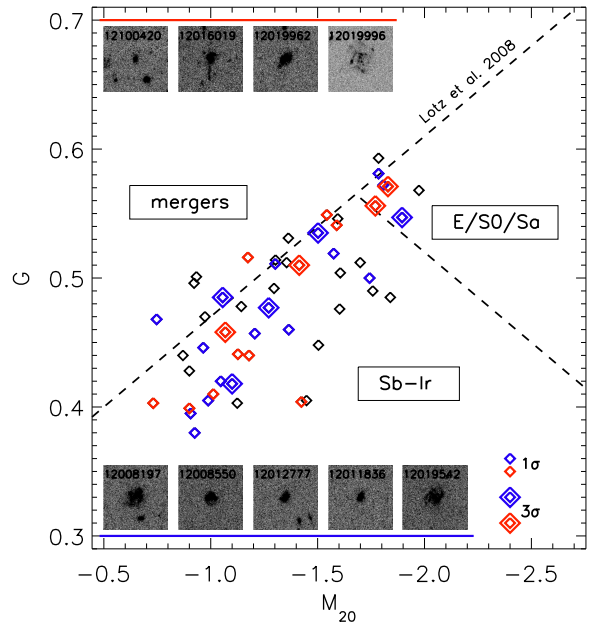


FIG. 22.— Outflow demographics as a function of the quantitative morphological parameters G and M_{20} , where parameter space can be partitioned into regions encompassing the classical morphological groups – mergers, ellipticals, and spirals/irregulars (Lotz et al. 2008). We highlight in blue (red) objects showing blueshifted (redshifted) Fe II resonance absorption lines, reserving small diamonds for 1σ significant V_1 velocities and larger diamonds for 3σ significant V_1 measurements. *HST* V-band thumbnails are shown for the nine objects with 3σ velocity detections. Both inflows and outflows occur in galaxies spanning a variety of morphologies; merging systems do not preferentially host winds. These results are consistent with the findings of Law et al. (2012b) at higher redshift, although Sato et al. (2009) noted that outflows were preferentially seen in merger candidates at $0.11 < z < 0.54$.

wind by imposing the criterion that $v_{ej} > v_c$. These authors find that this critical density is dependent on both R_d and v_c ; a local L_* galaxy has $\Sigma_{\text{SFR}}^{\text{crit}} \approx 0.06 M_{\odot} \text{ yr}^{-1} \text{ kpc}^{-2}$. This result is consistent with the observationally-motivated Σ_{SFR} threshold derived by Heckman (2002): $\Sigma_{\text{SFR}}^{\text{crit}} \approx 0.1 M_{\odot} \text{ yr}^{-1} \text{ kpc}^{-2}$.

Strickland et al. (2004) suggest an alternative scaling relation between outflow velocity and Σ_{SFR} assuming winds are driven by thermal pressure and that hot gas blows out of the galaxy three scale heights above the disk:

$$v_{ej} \propto \left(\frac{\Sigma_{\text{SFR}}}{\rho_0} \right)^{1/3} \quad (6)$$

where ρ_0 is the gas density. Following Chen et al. (2010), the above relation can be equivalently expressed using the Kennicutt-Schmidt (1998) law and the approximation that the gas density is proportional to the gas surface density divided by the scale height of the disk, H_z :

$$v_{ej} \propto \Sigma_{\text{SFR}}^{2/21} H_z^{1/3} \quad (7)$$

Strickland et al. (2004) adopt $\Sigma_{\text{SFR}} \propto \Sigma_g^{1.4}$ as the form of the Kennicutt-Schmidt (1998) law. If one instead uses the same functional form of the Kennicutt-Schmidt (1998) law employed by Murray et al. (2011), one finds that v_{ej} is independent of Σ_{SFR} . Equation 7 is consistent with the shallow scaling between outflow velocity

and Σ_{SFR} recorded by Chen et al. (2010), although it is important to note that the small dynamic range of the Chen et al. (2010) data ($120 \text{ km s}^{-1} < v_{ej} < 160 \text{ km s}^{-1}$) may obscure trends. However, as mentioned above, Chen et al. (2010) do find a significant correlation between Σ_{SFR} and the equivalent width of the Na D outflow component. The equivalent width of the outflow component is dependent on the velocity spread, covering fraction, and optical depth of the absorbing gas.

The power-law relations discussed above can be generalized as being of the form $v_{ej} \propto \Sigma_{\text{SFR}}^\alpha$, where $\alpha = 2.0$ or 0.1 . We use our V_1 and $\Sigma_{\text{SFR}}(A_{74})$ data with the IDL routine MPFITFUN (Markwardt 2009) to fit a power law of the form $V_1 = A\Sigma_{\text{SFR}}(A_{74})^\alpha + B$, where A , α , and B are free parameters. We choose to include only objects exhibiting outflows ($V_1 < 0 \text{ km s}^{-1}$) and we furthermore impose the prior that the additive term of the power law, B , is 0 (i.e., V_1 converges to 0 as $\Sigma_{\text{SFR}}(A_{74})$ goes to 0). When we fit a power law with $\alpha = 2.0$ or 0.1 to our data, we find a better fit with $\alpha = 2.0$ (although the χ^2 values per degree of freedom are large in both cases: 6.3, 7.5). Removing any priors on the slope, we recover a best-fit α of 0.8. However, we caution that the relatively large errors on our outflow velocities prevent a robust discrimination of α .

We can also bin the data in order to reduce the uncertainties on the velocity measurements. We divided the individual data points into three groups according to $\Sigma_{\text{SFR}}(A_{74})$ and fit a power law of the same form as discussed above to the average V_1 and $\Sigma_{\text{SFR}}(A_{74})$ values in each bin. We recover a best-fit slope of 0.3. When we bin all the data, including the objects showing apparent inflows but still excluding the two outliers at $\Sigma_{\text{SFR}}(A_{74}) > 2.0$, we find a best-fit slope of 1.6. As these various fits do not converge on a slope, it is clear that a larger sample of measurements is needed, ideally over a wider dynamic range in $\Sigma_{\text{SFR}}(A_{74})$. Outflow velocities derived from higher resolution data will be furthermore beneficial for drawing meaningful conclusions about the slope of the power law relating outflow velocity and star-formation rate surface density.

6.2. Prevalence of Winds

In the sample discussed here – 72 objects in the EGS, representing a subset of the data discussed in Martin et al. (2012), – we find 1σ significant detections of blueshifted Fe II absorption in $\sim 40\%$ of the sample. Likewise, $40 \pm 5\%$ of objects show outflows with blueshifts of at least -40 km s^{-1} . This 40% detection rate is a lower limit due to the incompleteness of measuring winds in low S/N spectra (Martin et al. 2012). In stating that blueshifts are seen in $\sim 40\%$ of the sample, it is important to remember that the detection rate can be explained by degenerate assumptions about the Fe II gas covering fraction and the percentage of galaxies hosting winds. If one assumes that the winds are isotropic with a covering fraction of 100%, we can conclude that $\sim 40\%$ of galaxies host winds. On the other hand, 100% of the sample could in fact host outflows if the Fe II absorbing gas covers only $\sim 40\%$ of each galaxy. We favor the latter scenario – in which winds are present in a majority of galaxies and yet observable only in a fraction of sources due to an average covering fraction less than unity – as our work supports the collimation of winds:

$\sim 70\%$ of the sample has star-formation rate surface densities above the threshold level predicted for driving outflows while only $\sim 40\%$ of objects show blueshifted Fe II absorption lines. Other authors have also suggested that winds are collimated (Rupke et al. 2005; Chen et al. 2010; Bordoloi et al. 2011). Imaging observations of winds in local starburst galaxies also reveal that outflows preferentially escape perpendicular to galactic disks (e.g., Heckman et al. 1990; De Young & Heckman 1994; Shopbell & Bland-Hawthorn 1998) and therefore do not cover the entirety of galaxies. We caution, however, that as high-redshift galaxies look less and less disk-dominated (Lotz et al. 2004; Law et al. 2007, 2012a), the interpretation of outflows emanating particular to a presumed disk is complicated. Galactic winds appear to be ubiquitous in samples of clumpy, unresolved galaxies at $z = 2-3$ (e.g., Shapley et al. 2003). The galaxies in our $z \sim 1$ sample, while generally not grand-design spirals, do not show the preponderance of disturbed morphologies characteristic of $z \geq 2$ samples (e.g., Law et al. 2007).

Our outflow detection frequency of 40% is similar to the detection frequency reported for the parent sample of objects observed with LRIS (Martin et al. 2012), indicative that the EGS and parent samples do not differ significantly in outflow properties. We also find that our outflow detection frequency is consistent with observations based on absorption lines in both local samples (Rupke et al. 2005) and at $z \sim 1.4$ (Weiner et al. 2009). Based on the absorption depth of Mg II in a co-added spectrum of galaxies, these authors inferred that at least half of the galaxies in their sample exhibit outflows of cool, low-ionization gas. We note that the kinematics and absorption strength of the Mg II lines in the Weiner et al. (2009) composite spectrum are similar to those seen in our composite spectrum after accounting for the different spectral resolutions of our respective data (Martin et al. 2012). This similarity is suggestive that the galactic winds probed by Mg II are fundamentally alike in both our sample and the Weiner et al. (2009) sample.

While the kinematics of Mg II in our composite spectrum are similar to those of the Weiner et al. (2009) composite (i.e., offset from the systemic velocity by several hundred km s^{-1}), we find no blueshift in the Fe II lines in our composite spectrum ($V_1 = -5 \pm 6 \text{ km s}^{-1}$). The spread of both positive and negative V_1 velocities observed for individual objects (Figure 11) is consistent with a global average velocity close to 0 km s^{-1} , but the negligible blueshift of Fe II lines in the composite spectrum may also be due to the smaller dynamic range of gas velocities probed by Fe II than Mg II (Rubin et al. 2010; Prochaska et al. 2011). We discuss potential explanations for this decreased dynamic range below.

6.3. Diagnostics of Winds

Outflowing galactic winds can be measured using a variety of samples: background quasars probing galactic halos along the line-of-sight, galaxy-galaxy pairs, and isolated galaxies in which the stellar disk provides a continuum for absorption by foreground interstellar gas. Even considering only the last technique – which we employ in this paper – a range of outflow velocity measurements will be obtained for a galaxy depending on which inter-

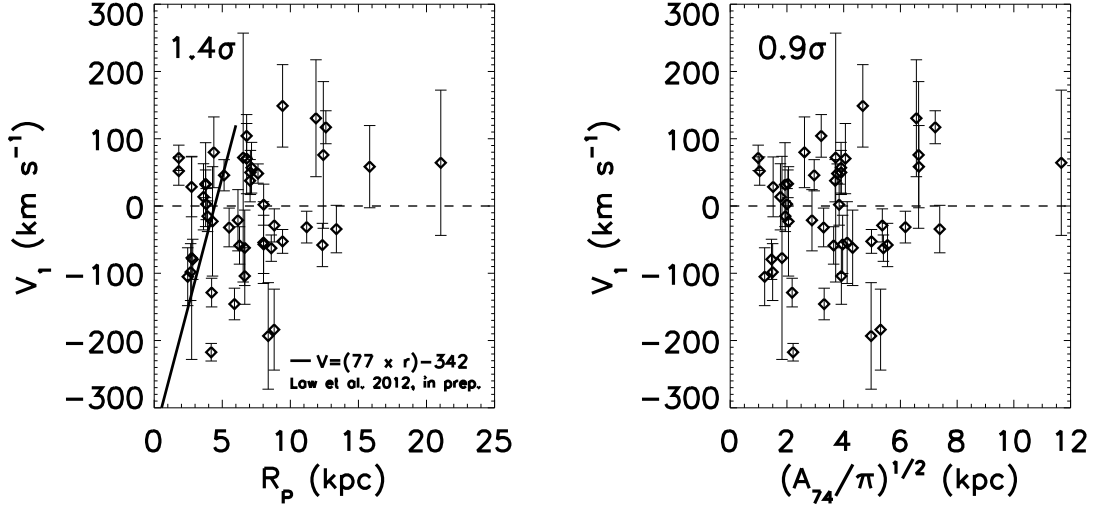


FIG. 23.— *Left*: Outflow velocity versus Petrosian radius. We overplot the relation from Law et al. (2012b), where these authors found a strong correlation between outflow velocity and size in a sample of galaxies at $z = 1.5$ – 3.6 . The Law et al. (2012b) objects have semi-major axes $r < 6$ kpc, while our sample is characterized by $\langle R_p \rangle = 7.1$ kpc. We find no statistical evidence in our sample that Petrosian radius and outflow velocity are correlated. *Right*: Outflow velocity versus the “radius” of the A_{74} area: $(A_{74}/\pi)^{1/2}$. As with the Petrosian radius, we find no evidence indicating a relation between outflow velocity and $(A_{74}/\pi)^{1/2}$.

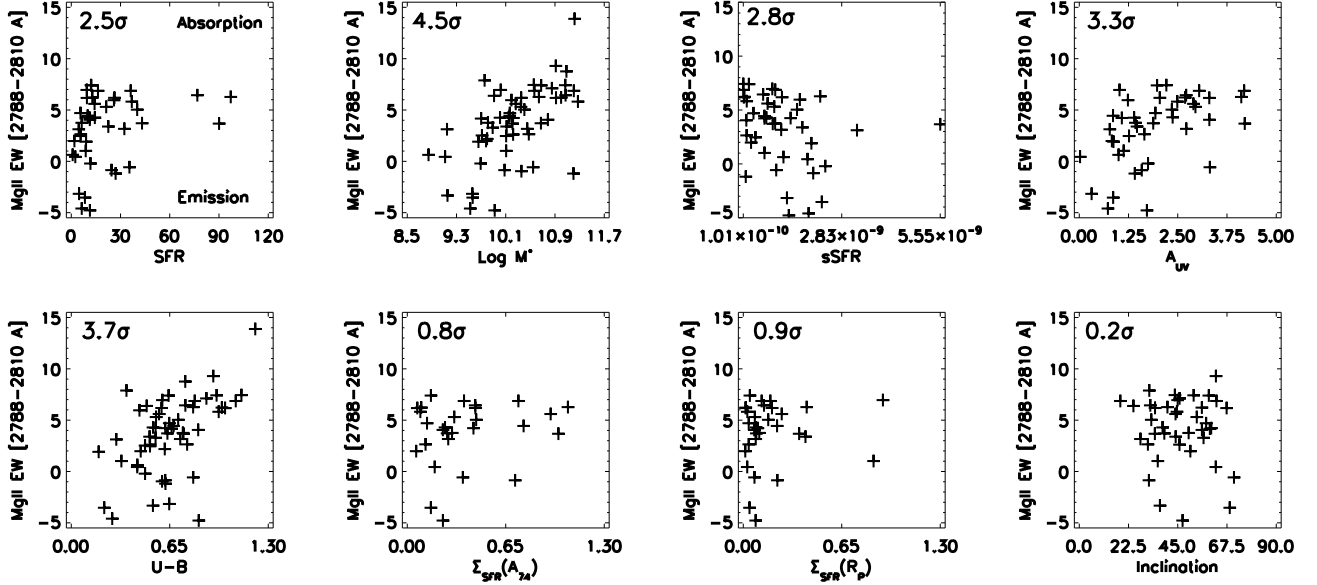


FIG. 24.— Scatter plots of various galaxy properties versus Mg II equivalent width, for galaxies in the EGS. The strength of Mg II was estimated from a simple summation of flux over the interval 2788–2810 Å encompassing both features of the doublet. We find that the strongest correlation, at 4.5σ ($r_S = 0.61$), is observed between Mg II equivalent width and stellar mass. A thorough discussion of Mg II will appear in Kornei et al. 2012b, in prep. and Martin et al. 2012b, in prep.

stellar tracer species are used and which parameterizations of absorption line kinematics are adopted.

From the extensive literature of galactic winds published to date, it is evident that a range of tracer elements are used in tandem with a variety of measurement techniques to parametrize the velocity of outflowing gas. Before we discuss how the choices of tracer elements and line-fitting methods may strongly affect the derived outflow velocity and its scaling with galaxy properties, it is important to acknowledge the intrinsic uncertainty of extracting a single representative outflow velocity from a

physical system characterized by many interacting clouds and shells of gas at a range of radii accelerated by a population of supernovae and massive stars injecting energy and momentum over a long timescale (> 100 Myr). In the absence of extremely high resolution and high S/N spectroscopy, the kinematics extracted from the centroids of absorption lines must be thought of as tracing only the gross average of multiple fronts of outflowing gas. With this limitation in mind, we now turn to a discussion of how the choice of tracer species may impact the measured properties of the outflows.

Absorption line studies are necessarily affected by the choice of absorption line probe. Authors often rely on relatively abundant species whose transitions are redshifted into the optical window of optimized detector sensitivity. Local studies typically employ Na D while investigations of higher redshift populations may use transitions of Si II, C II, Al II, Fe II, Mg II, or Mg I in the rest-frame UV. As these species differ in abundance, ionization potential, susceptibility to emission filling, and (perhaps) spatial distribution, it is unsurprising that their associated outflow velocities differ as well. For instance, Na D stellar absorption is known to be stronger in older stellar populations; if the outflow and stellar components are not separated by means of modeling, the outflow velocity can be significantly underestimated and trends between galaxy properties and winds can become skewed or lost (e.g., Chen et al. 2010; Coil et al. 2011). The different ionization energies of Na I, Fe II, Mg II, and Mg I (5.1, 16.1, 15.0, and 7.6 eV, respectively) result in these species tracing different populations of gas: Na I and Mg I, with low ionization potentials, require dense, shielded gas in order to survive while Fe II and Mg II are less easily ionized and therefore survive in more widespread environments. Emission filling affects particular transitions of species to a differing degree depending on the relative availability and oscillator strengths of transitions decaying to excited ground states. The Mg II doublet presents a particularly extreme case of emission filling. The doublet energy levels are such that these transitions are trapped; the absorption of a resonance photon necessarily results in the re-emission of another resonance photon. The Mg II doublet is therefore strongly susceptible to emission filling and measurements of the centroids of these transitions may yield different kinematic information (i.e., larger blueshifts) relative to that derived from features less affected by emission filling (Martin et al. 2012). The coincidental presence of additional spectral features adjacent to absorption lines of interest may also contaminate outflow signatures (e.g., He I $\lambda 5876 \sim 15 \text{ \AA}$ blueward of Na D).

Differences in oscillator strengths also likely impact derived outflow velocities. In the case of comparing velocities measured from Fe II and Mg II transitions, the larger oscillator strength of the Mg II line at 2796 \AA ($f_{12} = 0.60$) compared with the oscillator strengths of the Fe II lines at 2344 , 2374 , and 2587 \AA used in our analyses ($f_{12} = 0.04\text{--}0.11$) means that Mg II is optically thick at lower column densities than Fe II. Mg II is a better probe of rarefied gas than Fe II simply due to its larger cross-section for absorption. Bordoloi et al. (2011) found that Mg II equivalent widths decrease with increasing distance from galaxies. If equivalent width is a proxy for gas column density (neglecting the effects of saturation) then one can conclude that Mg II gas column density decreases with increasing distance from galaxies. Given that Mg II is an effective tracer of low-density gas, and presuming that low-density gas is found far from galaxies, the larger outflow velocities inferred for Mg II compared with Fe II (Figure 25; Rubin et al. 2010; Prochaska et al. 2011) are suggestive that the speed of galactic winds increases with increasing galactocentric radius. This inference that galactic winds are accelerating is consistent with recent work by Martin & Bouché (2009) and

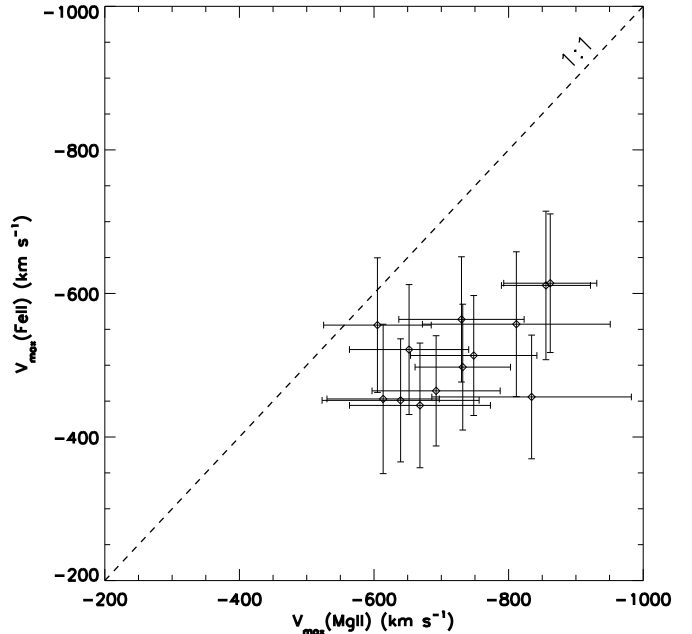


FIG. 25.— $V_{max}(\text{Mg II})$ versus $V_{max}(\text{Fe II})$, for the 13 composite spectra discussed in this paper. $V_{max}(\text{Mg II})$ is systematically more blueshifted than $V_{max}(\text{Fe II})$, as discussed in Section 6.

Steidel et al. (2010). Martin & Bouché (2009) studied a sample of ULIRGs at $z \sim 0.25$ and concluded that winds are accelerating based on the assumption of a spherical outflow and measurements of how gas covering fractions vary with velocity. These authors found that gas covering fractions decreased with increasing outflow velocity. Pairing this observation with the prediction that a spherical outflow will suffer geometrical dilution (i.e., reduction of its covering fraction) as it breaks up and expands to larger galactocentric radii, Martin & Bouché (2009) concluded that outflowing gas is accelerating. Steidel et al. (2010) showed that models of an accelerating wind provided the best match to observations at $z \sim 2\text{--}3$ of interstellar absorption lines arising from a range of galaxy impact parameters ($b \sim 0\text{--}200 \text{ kpc}$). Simulations also suggest that higher velocity gas may be located at larger galactocentric radii simply due to differences in travel time (e.g., Dalla Vecchia & Schaye 2012). Observations of decreasing gas column densities with increasing outflow velocity seen in the gravitationally-lensed Lyman Break Galaxy cB58 (Pettini et al. 2002) provide further evidence of the connection between low-density gas, large galactocentric distances, and large outflow velocities.

The effects discussed above are all dependent on the choice of tracer species. We now examine a more tangible aspect of the data analysis: how do different measurements of outflow velocity impact the derived velocities and subsequent scaling relations with galaxy properties? Two techniques feature prominently in the literature for quantifying the blueshift of an absorption line tracing an outflow. Some authors rely on fitting the centroid of an absorption line; i.e., measuring the wavelength at which the bulk of the absorption occurs and assuming that this velocity characterizes the outflowing gas (Shapley et al. 2003; Martin 2005; Rubin et al. 2012; Coil et al. 2011;

Law et al. 2012b). Other authors parameterize a maximal outflow velocity by measuring the blue shoulder of an absorption line at some fractional level of the continuum (e.g., 90%, Weiner et al. 2009; Coil et al. 2011).

These two techniques, measuring different characteristics of the outflow, are complementary and both methods have associated uncertainties. In the case of the centroid measurement, one is susceptible to mistakenly attributing the entire absorption profile to an outflow when in fact the profile should be decomposed into both an outflow signature and a stellar absorption (or stationary ISM) component. Failing to correct for the gas not entrained in the outflow will yield an underestimate of the derived outflow velocity (Weiner et al. 2009; Coil et al. 2011), although such a correction is difficult and highly uncertain for low-resolution, low-S/N data (Steidel et al. 2010). In our sample, the Fe II absorption centroid that we measure is unlikely to be significantly contaminated by stellar absorption due to the young, star-forming nature of the majority of our galaxies; stellar Fe II absorption is more prevalent in older populations (e.g., Bruzual & Charlot 2003). The maximal outflow velocity method is dependent on resolved absorption lines; low spectral resolution data of unresolved absorption lines will merely reflect the instrumental profile and therefore measurements of a supposed wing profile will be meaningless. Furthermore, maximal outflow velocity measurements are strongly dependent on spectroscopic S/N (Section 4.3). We mitigate this effect in our present work by limiting our analyses of maximal outflow velocities to measurements from the composite spectra which have largely uniform S/N.

7. SUMMARY AND CONCLUSIONS

We utilized spectroscopic and imaging observations to investigate the properties and prevalence of outflowing galactic winds in a sample of 72 objects at $0.7 < z < 1.3$ in the Extended Groth Strip. These data are part of a larger study discussed in Martin et al. (2012). We used LRIS spectroscopy to study interstellar absorption lines in the rest-frame UV, including transitions of Fe II and Mg II. With *GALEX*, *HST*, and *Spitzer* imaging from the AEGIS dataset, we employed two complementary analysis techniques to investigate how galaxy properties are correlated with the prevalence and strength of winds: 1) direct comparison of individual outflow velocities with galaxy properties and 2) construction of composite spectra based on subsamples of objects exhibiting similar star-forming or structural characteristics. We provide below a numbered list of our main conclusions in summary and expand on these points in the following paragraphs.

1. Approximately 40% of the sample exhibits $> 1\sigma$ outflows in Fe II.
2. We find a 3.1σ trend between outflow velocity and Σ_{SFR} .
3. Outflow velocity and SFR are only weakly correlated.
4. There is no apparent link between outflowing gas and host galaxy morphological type.
5. Face-on galaxies exhibit more blueshifted Fe II centroids than edge-on galaxies.
6. The kinematics of Fe II and Mg II gas are often discrepant, with Mg II preferentially tracing higher velocity

gas.

The sample includes objects exhibiting Fe II Doppler shifts ranging from -217 km s^{-1} to $+155 \text{ km s}^{-1}$, where approximately 40% of the sample exhibits $> 1\sigma$ outflows in Fe II. We find that $40 \pm 5\%$ of the sample is characterized by Fe II blueshifts of at least -40 km s^{-1} ; this outflow fraction is consistent with that of the parent sample discussed in Martin et al. (2012). We used SFRs inferred from *GALEX* imaging in tandem with galaxy area estimates to measure Σ_{SFR} . Given the clumpy morphologies of star-forming galaxies at $z \sim 1$, we developed a new technique to estimate the area of only UV-bright clumps. Using these new “clump areas” and also galaxy areas corresponding to Petrosian radii, we measured Σ_{SFR} . The majority of objects have $\Sigma_{\text{SFR}} > 0.1 \text{ M}_{\odot} \text{ yr}^{-1} \text{ kpc}^{-2}$, yet we observe significant Fe II blueshifts in only a minority of the sample. The lower fraction of objects showing outflows relative to that meeting the Σ_{SFR} threshold for driving a wind is evidence that winds are collimated and therefore observable only over a limited range of inclinations. We find a strong ($\sim 3\sigma$) trend between outflow velocity and Σ_{SFR} such that objects with higher star-formation rate surface densities show more blueshifted Fe II absorption. Composite spectra assembled on the basis of Σ_{SFR} also support this correlation, with V_1 , $V_{\text{max}}(\text{Fe II})$, and $V_{\text{max}}(\text{Mg II})$ all varying toward more blueshifted values with increasing Σ_{SFR} . At the same time, outflow velocity and SFR are only weakly correlated. We propose that the data span too narrow a range in SFR (roughly two orders of magnitude) to show a trend. While the range of Σ_{SFR} is similarly limited ($0.03 \lesssim \Sigma_{\text{SFR}}(A_{74}) \lesssim 3.0$), the trend between outflow velocity and Σ_{SFR} may be more fundamental and therefore recoverable over a smaller dynamic range.

Based on quantitative morphological analyses of $V+I$ *HST* imaging, we do not find any link between outflowing gas and galaxy structure. Rather, galaxies experiencing winds appear to span the classical morphological regimes from disks to spheroidals to mergers. We estimated galaxy inclinations from axis ratios in the *HST* imaging and found that face-on systems exhibit stronger Fe II blueshifts than edge-on galaxies. This result lends credence to the canonical picture of outflowing winds emanating perpendicular to galactic disks. Motivated by recent results of faster outflows in smaller galaxies, we investigated the relationship between outflow velocity and size, but found no evidence for a trend.

Quantifying the prevalence of outflows requires an understanding of the physical processes affecting the absorption lines tracing winds. Different elemental tracer species often yield discrepant outflow velocities, for reasons including emission filling, differences in oscillator strengths, and perhaps simply intrinsic variations in gas cloud kinematics. Furthermore, the variety of techniques available for quantifying the speed of galactic winds (centroid fitting, maximal velocity measurements from a blue wing, etc.) complicate the parameterization of a single outflow velocity. Future studies utilizing higher resolution spectroscopic data and complementary spatially-resolved imaging to determine galaxy morphologies and the spatial extent of winds will be crucial for better understanding the link between galactic outflows and their host galaxies at a range of redshifts.

We appreciate the referee for his or her helpful comments that improved the quality of this paper. We thank Ben Weiner for providing measurements of [OII] widths and his composite spectrum of star-forming galaxies. K.A.K. is grateful for support from a Dissertation Year Fellowship at UCLA. A.E.S. acknowledges support from the David and Lucile Packard Foundation. A.L.C. has been supported by the Alfred P. Sloan Foundation and NSF CAREER award AST-1055081. This study was supported in part by the NSF under contract AST-0909182 (CLM). A portion of this work was completed at the Aspen Center for Physics (CLM). This study makes use of data from AEGIS, a multiwavelength sky survey conducted with the Chandra, GALEX, Hubble, Keck, CFHT, MMT, Subaru, Palomar, Spitzer, VLA, and other telescopes and supported in part by the NSF, NASA, and the STFC. We also wish to recognize and acknowledge the very significant cultural role and reverence that the summit of Mauna Kea has always had within the indigenous Hawaiian community. We are most fortunate to have the opportunity to conduct observations from this mountain.

REFERENCES

- Bertin, E., & Arnouts, S. 1996, *A&AS*, 117, 393
- Bordoloi, R., Lilly, S. J., Knobel, C., Bolzonella, M., Kampczyk, P., Carollo, C. M., Iovino, A., Zucca, E., Contini, T., Kneib, J.-P., Le Fevre, O., Mainieri, V., Renzini, A., Scodreggio, M., Zamorani, G., Balestra, I., Bardelli, S., Bongiorno, A., Caputi, K., Cucciati, O., de la Torre, S., de Ravel, L., Garilli, B., Kovač, K., Lamareille, F., Le Borgne, J.-F., Le Brun, V., Maier, C., Mignoli, M., Pello, R., Peng, Y., Perez Montero, E., Presotto, V., Scarlata, C., Silverman, J., Tanaka, M., Tasca, L., Tresse, L., Vergani, D., Barnes, L., Cappi, A., Cimatti, A., Coppa, G., Diener, C., Franzetti, P., Koekemoer, A., López-Sanjuan, C., McCracken, H. J., Moresco, M., Nair, P., Oesch, P., Pozzetti, L., & Welikala, N. 2011, *ApJ*, 743, 10
- Bruzual, G., & Charlot, S. 2003, *MNRAS*, 344, 1000
- Bundy, K., Ellis, R. S., Conselice, C. J., Taylor, J. E., Cooper, M. C., Willmer, C. N. A., Weiner, B. J., Coil, A. L., Noeske, K. G., & Eisenhardt, P. R. M. 2006, *ApJ*, 651, 120
- Cecil, G., Bland-Hawthorn, J., Veilleux, S., & Filippenko, A. V. 2001, *ApJ*, 555, 338
- Chabrier, G. 2003, *PASP*, 115, 763
- Chary, R., & Elbaz, D. 2001, *ApJ*, 556, 562
- Chen, Y.-M., Tremonti, C. A., Heckman, T. M., Kauffmann, G., Weiner, B. J., Brinchmann, J., & Wang, J. 2010, *AJ*, 140, 445
- Coil, A. L., Weiner, B. J., Holz, D. E., Cooper, M. C., Yan, R., & Aird, J. 2011, *ApJ*, 743, 46
- Croton, D. J., Springel, V., White, S. D. M., De Lucia, G., Frenk, C. S., Gao, L., Jenkins, A., Kauffmann, G., Navarro, J. F., & Yoshida, N. 2006, *MNRAS*, 365, 11
- Dalla Vecchia, C., & Schaye, J. 2012, *MNRAS*, accepted (astro-ph/1203.5667)
- Davis, M., Guhathakurta, P., Konidaris, N. P., Newman, J. A., Ashby, M. L. N., Biggs, A. D., Barmby, P., Bundy, K., Chapman, S. C., Coil, A. L., Conselice, C. J., Cooper, M. C., Croton, D. J., Eisenhardt, P. R. M., Ellis, R. S., Faber, S. M., Fang, T., Fazio, G. G., Georgakakis, A., Gerke, B. F., Goss, W. M., Gwyn, S., Harker, J., Hopkins, A. M., Huang, J., Ivison, R. J., Kassin, S. A., Kirby, E. N., Koekemoer, A. M., Koo, D. C., Laird, E. S., Le Floch, E., Lin, L., Lotz, J. M., Marshall, P. J., Martin, D. C., Metevier, A. J., Moustakas, L. A., Nandra, K., Noeske, K. G., Papovich, C., Phillips, A. C., Rich, R. M., Rieke, G. H., Rigopoulou, D., Salim, S., Schiminovich, D., Simard, L., Smail, I., Small, T. A., Weiner, B. J., Willmer, C. N. A., Willner, S. P., Wilson, G., Wright, E. L., & Yan, R. 2007, *ApJ*, 660, L1
- de Vaucouleurs, G. 1948, *Annales d'Astrophysique*, 11, 247
- De Young, D. S., & Heckman, T. M. 1994, *ApJ*, 431, 598
- Dove, J. B., Shull, J. M., & Ferrara, A. 2000, *ApJ*, 531, 846
- Elbaz, D., Daddi, E., Le Borgne, D., Dickinson, M., Alexander, D. M., Chary, R.-R., Starck, J.-L., Brandt, W. N., Kitzbichler, M., MacDonald, E., Nonino, M., Popesso, P., Stern, D., & Vanzella, E. 2007, *A&A*, 468, 33
- Ferrara, A., & Ricotti, M. 2006, *MNRAS*, 373, 571
- Ferrarese, L., & Merritt, D. 2000, *ApJ*, 539, L9
- Ford, H. C., Clampin, M., Hartig, G. F., Illingworth, G. D., Sirianni, M., Martel, A. R., Meurer, G. R., McCann, W. J., Sullivan, P. C., Bartko, F., Benitez, N., Blakelee, J., Bouwens, R., Broadhurst, T., Brown, R. A., Burrows, C. J., Campbell, D., Cheng, E. S., Feldman, P. D., Franx, M., Golimowski, D. A., Gronwall, C., Kimble, R. A., Krist, J. E., Lesser, M. P., Magee, D., Miley, G., Postman, M., Rafal, M. D., Rosati, P., and Sparks, W. B., Tran, H. D., Tsvetanov, Z. I., Volmer, P., White, R. L., & Woodruff, R. A. 2003, in Presented at the Society of Photo-Optical Instrumentation Engineers (SPIE) Conference, Vol. 4854, Society of Photo-Optical Instrumentation Engineers (SPIE) Conference Series, ed. J. C. Blades & O. H. W. Siegmund, 81–94
- Förster Schreiber, N. M., Genzel, R., Bouché, N., Cresci, G., Davies, R., Buschkamp, P., Shapiro, K., Tacconi, L. J., Hicks, E. K. S., Genel, S., Shapley, A. E., Erb, D. K., Steidel, C. C., Lutz, D., Eisenhauer, F., Gillessen, S., Sternberg, A., Renzini, A., Cimatti, A., Daddi, E., Kurk, J., Lilly, S., Kong, X., Lehnert, M. D., Nesvadba, N., Verma, A., McCracken, H., Arimoto, N., Mignoli, M., & Onodera, M. 2009, *ApJ*, 706, 1364
- Förster Schreiber, N. M., Genzel, R., Lehnert, M. D., Bouché, N., Verma, A., Erb, D. K., Shapley, A. E., Steidel, C. C., Davies, R., Lutz, D., Nesvadba, N., Tacconi, L. J., Eisenhauer, F., Abuter, R., Gilbert, A., Gillessen, S., & Sternberg, A. 2006, *ApJ*, 645, 1062
- Franx, M., Illingworth, G. D., Kelson, D. D., van Dokkum, P. G., & Tran, K. 1997, *ApJ*, 486, L75+
- Fujita, A., Martin, C. L., Mac Low, M., New, K. C. B., & Weaver, R. 2009, *ApJ*, 698, 693
- Genzel, R., Newman, S., Jones, T., Förster Schreiber, N. M., Shapiro, K., Genel, S., Lilly, S. J., Renzini, A., Tacconi, L. J., Bouché, N., Burkert, A., Cresci, G., Buschkamp, P., Carollo, C. M., Ceverino, D., Davies, R., Dekel, A., Eisenhauer, F., Hicks, E., Kurk, J., Lutz, D., Mancini, C., Naab, T., Peng, Y., Sternberg, A., Vergani, D., & Zamorani, G. 2011, *ApJ*, 733, 101
- Gialalisco, M., Vanzella, E., Salimbeni, S., Tripp, T. M., Dickinson, M., Cassata, P., Renzini, A., Guo, Y., Ferguson, H. C., Nonino, M., Cimatti, A., Kurk, J., Mignoli, M., Tang, Y., & . 2011, *ApJ*, 743, 95
- Gnedin, N. Y., Kravtsov, A. V., & Chen, H.-W. 2008, *ApJ*, 672, 765
- Heckman, T. M. 2002, in ASP Conf. Ser. 254: Extragalactic Gas at Low Redshift, 292
- Heckman, T. M., Armus, L., & Miley, G. K. 1990, *ApJS*, 74, 833
- Heckman, T. M., Borthakur, S., Overzier, R., Kauffmann, G., Basu-Zych, A., Leitherer, C., Sembach, K., Martin, D. C., Rich, R. M., Schiminovich, D., & Seibert, M. 2011, *ApJ*, 730, 5
- Heckman, T. M., Lehnert, M. D., Strickland, D. K., & Armus, L. 2000, *ApJS*, 129, 493
- Heckman, T. M., & Leitherer, C. 1997, *AJ*, 114, 69
- Heckman, T. M., Sembach, K. R., Meurer, G. R., Leitherer, C., Calzetti, D., & Martin, C. L. 2001a, *ApJ*, 558, 56
- Heckman, T. M., Sembach, K. R., Meurer, G. R., Strickland, D. K., Martin, C. L., Calzetti, D., & Leitherer, C. 2001b, *ApJ*, 554, 1021
- Hopkins, P. F., Richards, G. T., & Hernquist, L. 2007, *ApJ*, 654, 731
- Kennicutt, Jr., R. C. 1998, *ARA&A*, 36, 189
- Kroupa, P. 2001, *MNRAS*, 322, 231
- Krug, H. B., Rupke, D. S. N., & Veilleux, S. 2010, *ApJ*, 708, 1145
- Kulas, K. R., Shapley, A. E., Kollmeier, J. A., Zheng, Z., Steidel, C. C., & Hainline, K. N. 2012, *ApJ*, 745, 33
- Laird, E. S., Nandra, K., Georgakakis, A., Aird, J. A., Barmby, P., Conselice, C. J., Coil, A. L., Davis, M., Faber, S. M., Fazio, G. G., Guhathakurta, P., Koo, D. C., Sarajedini, V., & Willmer, C. N. A. 2009, *ApJS*, 180, 102
- Law, D. R., Steidel, C. C., Erb, D. K., Larkin, J. E., Pettini, M., Shapley, A. E., & Wright, S. A. 2009, *ApJ*, 697, 2057
- Law, D. R., Steidel, C. C., Erb, D. K., Pettini, M., Reddy, N. A., Shapley, A. E., Adelberger, K. L., & Simenc, D. J. 2007, *ApJ*, 656, 1
- Law, D. R., Steidel, C. C., Shapley, A. E., Nagy, S. R., Reddy, N. A., & Erb, D. K. 2012a, *ApJ*, 745, 85
- . 2012b, *ApJ*, submitted (astro-ph/1206.6889)
- Le Tiran, L., Lehnert, M. D., van Driel, W., Nesvadba, N. P. H., & Di Matteo, P. 2011, *A&A*, 534, L4
- Lehnert, M. D., & Heckman, T. M. 1996, *ApJ*, 462, 651
- Leitherer, C., & Heckman, T. M. 1995, *ApJS*, 96, 9
- Lequeux, J., Kunth, D., Mas-Hesse, J. M., & Sargent, W. L. W. 1995, *A&A*, 301, 18
- Lotz, J. M., Davis, M., Faber, S. M., Guhathakurta, P., Gwyn, S., Huang, J., Koo, D. C., Le Floch, E., Lin, L., Newman, J., Noeske, K., Papovich, C., Willmer, C. N. A., Coil, A., Conselice, C. J., Cooper, M., Hopkins, A. M., Metevier, A., Primack, J., Rieke, G., & Weiner, B. J. 2008, *ApJ*, 672, 177
- Lotz, J. M., Primack, J., & Madau, P. 2004, *AJ*, 128, 163
- Markwardt, C. B. 2009, in Astronomical Society of the Pacific Conference Series, Vol. 411, Astronomical Data Analysis Software and Systems XVIII, ed. D. A. Bohlender, D. Durand, & P. Dowler, 251
- Martin, C. L. 1999, *ApJ*, 513, 156
- . 2005, *ApJ*, 621, 227
- Martin, C. L., & Bouché, N. 2009, *ApJ*, 703, 1394

- Martin, C. L., Shapley, A. E., Coil, A. L., Kornei, K. A., Bundy, K., Weiner, B. J., Noeske, K. G., & Schiminovich, D. 2012, *ApJ*, submitted (astro-ph/1206.5552)
- Martin, D. C., Fanson, J., Schiminovich, D., Morrissey, P., Friedman, P. G., Barlow, T. A., Conroy, T., Grange, R., Jelinsky, P. N., Milliard, B., Siegmund, O. H. W., Bianchi, L., Byun, Y., Donas, J., Forster, K., Heckman, T. M., Lee, Y., Madore, B. F., Malina, R. F., Neff, S. G., Rich, R. M., Small, T., Surber, F., Szalay, A. S., Welsh, B., & Wyder, T. K. 2005, *ApJ*, 619, L1
- Meurer, G. R., Heckman, T. M., & Calzetti, D. 1999, *ApJ*, 521, 64
- Murray, N., Ménard, B., & Thompson, T. A. 2011, *ApJ*, 735, 66
- Murray, N., Quataert, E., & Thompson, T. A. 2005, *ApJ*, 618, 569
- Neugebauer, G., Habing, H. J., van Duinen, R., Aumann, H. H., Baud, B., Beichman, C. A., Beintema, D. A., Boggess, N., Clegg, P. E., de Jong, T., Emerson, J. P., Gautier, T. N., Gillett, F. C., Harris, S., Hauser, M. G., Houck, J. R., Jennings, R. E., Low, F. J., Marsden, P. L., Miley, G., Olmon, F. M., Pottasch, S. R., Raimond, E., Rowan-Robinson, M., Soifer, B. T., Walker, R. G., Wesselius, P. R., & Young, E. 1984, *ApJ*, 278, L1
- Newman, J. A., Cooper, M. C., Davis, M., Faber, S. M., Coil, A. L., Guhathakurta, P., Koo, D. C., Phillips, A. C., Conroy, C., Dutton, A. A., Finkbeiner, D. P., Gerke, B. F., Rosario, D. J., Weiner, B. J., Willmer, C. N. A., Yan, R., Harker, J. J., Kassin, S. A., Konidaris, N. P., Lai, K., Madgwick, D. S., Noeske, K. G., Wirth, G. D., Connolly, A. J., Kaiser, N., Kirby, E. N., Lemaux, B. C., Lin, L., Lotz, J. M., Luppino, G. A., Marinoni, C., Matthews, D. J., Metevier, A., & Schiavon, R. P. 2012, *ApJ*, submitted (astro-ph/1203.3192)
- Noeske, K. G., Weiner, B. J., Faber, S. M., Papovich, C., Koo, D. C., Somerville, R. S., Bundy, K., Conselice, C. J., Newman, J. A., Schiminovich, D., Le Floch, E., Coil, A. L., Rieke, G. H., Lotz, J. M., Primack, J. R., Barmby, P., Cooper, M. C., Davis, M., Ellis, R. S., Fazio, G. G., Guhathakurta, P., Huang, J., Kassin, S. A., Martin, D. C., Phillips, A. C., Rich, R. M., Small, T. A., Willmer, C. N. A., & Wilson, G. 2007, *ApJ*, 660, L43
- Oke, J. B., Cohen, J. G., Carr, M., Cromer, J., Dingizian, A., Harris, F. H., Labrecque, S., Lucinio, R., Schaal, W., Epps, H., & Miller, J. 1995, *PASP*, 107, 375
- Oppenheimer, B. D., & Davé, R. 2006, *MNRAS*, 373, 1265
- Osterbrock, D. E. 1989, *Astrophysics of gaseous nebulae and active galactic nuclei*, ed. Osterbrock, D. E.
- Peng, C. Y., Ho, L. C., Impey, C. D., & Rix, H.-W. 2002, *AJ*, 124, 266
- . 2010, *AJ*, 139, 2097
- Pettini, M., Rix, S. A., Steidel, C. C., Adelberger, K. L., Hunt, M. P., & Shapley, A. E. 2002, *ApJ*, 569, 742
- Pettini, M., Shapley, A. E., Steidel, C. C., Cuby, J., Dickinson, M., Moorwood, A. F. M., Adelberger, K. L., & Giavalisco, M. 2001, *ApJ*, 554, 981
- Pettini, M., Steidel, C. C., Adelberger, K. L., Dickinson, M., & Giavalisco, M. 2000, *ApJ*, 528, 96
- Prochaska, J. X., Kasen, D., & Rubin, K. 2011, *ApJ*, 734, 24
- Reddy, N. A., Steidel, C. C., Pettini, M., Adelberger, K. L., Shapley, A. E., Erb, D. K., & Dickinson, M. 2008, *ApJS*, 175, 48
- Robertson, B., Hernquist, L., Cox, T. J., Di Matteo, T., Hopkins, P. F., Martini, P., & Springel, V. 2006, *ApJ*, 641, 90
- Rubin, K. H. R., Prochaska, J. X., Koo, D. C., & Phillips, A. C. 2012, *ApJ*, 747, L26
- Rubin, K. H. R., Weiner, B. J., Koo, D. C., Martin, C. L., Prochaska, J. X., Coil, A. L., & Newman, J. A. 2010, *ApJ*, 719, 1503
- Rupke, D. S., Veilleux, S., & Sanders, D. B. 2002, *ApJ*, 570, 588
- . 2005, *ApJS*, 160, 115
- Salim, S., Rich, R. M., Charlot, S., Brinchmann, J., Johnson, B. D., Schiminovich, D., Seibert, M., Mallery, R., Heckman, T. M., Forster, K., Friedman, P. G., Martin, D. C., Morrissey, P., Neff, S. G., Small, T., Wyder, T. K., Bianchi, L., Donas, J., Lee, Y., Madore, B. F., Milliard, B., Szalay, A. S., Welsh, B. Y., & Yi, S. K. 2007, *ApJS*, 173, 267
- Salpeter, E. E. 1955, *ApJ*, 121, 161
- Sanders, D. B., & Mirabel, I. F. 1996, *ARA&A*, 34, 749
- Sato, T., Martin, C. L., Noeske, K. G., Koo, D. C., & Lotz, J. M. 2009, *ApJ*, 696, 214
- Scannapieco, E., Silk, J., & Bouwens, R. 2005, *ApJ*, 635, L13
- Schiminovich, D., Wyder, T. K., Martin, D. C., Johnson, B. D., Salim, S., Seibert, M., Treyer, M. A., Budavári, T., Hoopes, C., Zamojski, M., Barlow, T. A., Forster, K. G., Friedman, P. G., Morrissey, P., Neff, S. G., Small, T. A., Bianchi, L., Donas, J., Heckman, T. M., Lee, Y., Madore, B. F., Milliard, B., Rich, R. M., Szalay, A. S., Welsh, B. Y., & Yi, S. 2007, *ApJS*, 173, 315
- Schwartz, C. M., & Martin, C. L. 2004, *ApJ*, 610, 201
- Seibert, M., Martin, D. C., Heckman, T. M., Buat, V., Hoopes, C., Barlow, T., Bianchi, L., Byun, Y., Donas, J., Forster, K., Friedman, P. G., Jelinsky, P., Lee, Y., Madore, B. F., Malina, R., Milliard, B., Morrissey, P., Neff, S., Rich, R. M., Schiminovich, D., Morrissey, P., Neff, S., Rich, R. M., Schiminovich, D., & Wyder, T. K. 2005, *ApJ*, 619, L55
- Shapley, A. E., Steidel, C. C., Pettini, M., & Adelberger, K. L. 2003, *ApJ*, 588, 65
- Sharma, M., & Nath, B. B. 2012, *ApJ*, 750, 55
- Shobell, P. L., & Bland-Hawthorn, J. 1998, *ApJ*, 493, 129
- Socrates, A., Davis, S. W., & Ramirez-Ruiz, E. 2008, *ApJ*, 687, 202
- Steidel, C. C., Erb, D. K., Shapley, A. E., Pettini, M., Reddy, N., Bogosavljević, M., Rudie, G. C., & Rakic, O. 2010, *ApJ*, 717, 289
- Steidel, C. C., Giavalisco, M., Pettini, M., Dickinson, M., & Adelberger, K. L. 1996, *ApJ*, 462, L17+
- Steidel, C. C., Pettini, M., & Adelberger, K. L. 2001, *ApJ*, 546, 665
- Steidel, C. C., Shapley, A. E., Pettini, M., Adelberger, K. L., Erb, D. K., Reddy, N. A., & Hunt, M. P. 2004, *ApJ*, 604, 534
- Strickland, D. K., & Heckman, T. M. 2009, *ApJ*, 697, 2030
- Strickland, D. K., Heckman, T. M., Colbert, E. J. M., Hoopes, C. G., & Weaver, K. A. 2004, *ApJ*, 606, 829
- Swinbank, A. M., Smail, I., Chapman, S. C., Borys, C., Alexander, D. M., Blain, A. W., Conselice, C. J., Hainline, L. J., & Ivison, R. J. 2010, *MNRAS*, 405, 234
- Talia, M., Mignoli, M., Cimatti, A., Kurk, J., Berta, S., Bolzonella, M., Cassata, P., Daddi, E., Dickinson, M., Franceschini, A., Halliday, C., Pozzetti, L., Renzini, A., Rodighiero, G., Rosati, P., & Zamorani, G. 2012, *A&A*, 539, A61
- Tremonti, C. A., Heckman, T. M., Kauffmann, G., Brinchmann, J., Charlot, S., White, S. D. M., Seibert, M., Peng, E. W., Schlegel, D. J., Uomoto, A., Fukugita, M., & Brinkmann, J. 2004, *ApJ*, 613, 898
- Tremonti, C. A., Moustakas, J., & Diamond-Stanic, A. M. 2007, *ApJ*, 663, L77
- Tully, R. B., & Fisher, J. R. 1977, *A&A*, 54, 661
- Veilleux, S., Cecil, G., & Bland-Hawthorn, J. 2005, *ARA&A*, 43, 769
- Weiner, B. J., Coil, A. L., Prochaska, J. X., Newman, J. A., Cooper, M. C., Bundy, K., Conselice, C. J., Dutton, A. A., Faber, S. M., Koo, D. C., Lotz, J. M., Rieke, G. H., & Rubin, K. H. R. 2009, *ApJ*, 692, 187
- Willmer, C. N. A., Faber, S. M., Koo, D. C., Weiner, B. J., Newman, J. A., Coil, A. L., Connolly, A. J., Conroy, C., Cooper, M. C., Davis, M., Finkbeiner, D. P., Gerke, B. F., Guhathakurta, P., Harker, J., Kaiser, N., Kassin, S., Konidaris, N. P., Lin, L., Luppino, G., Madgwick, D. S., Noeske, K. G., Phillips, A. C., & Yan, R. 2006, *ApJ*, 647, 853

York, D. G., Adelman, J., Anderson, Jr., J. E., Anderson, S. F., Annis, J., Bahcall, N. A., Bakken, J. A., Barkhouser, R., Bastian, S., Berman, E., Boroski, W. N., Bracker, S., Briegel, C., Briggs, J. W., Brinkmann, J., Brunner, R., Burles, S., Carey, L., Carr, M. A., Castander, F. J., Chen, B., Colestock, P. L., Connolly, A. J., Crocker, J. H., Csabai, I., Czarapata, P. C., Davis, J. E., Doi, M., Dombeck, T., Eisenstein, D., Ellman, N., Elms, B. R., Evans, M. L., Fan, X., Federwitz, G. R., Fiscelli, L., Friedman, S., Frieman, J. A., Fukugita, M., Gillespie, B., Gunn, J. E., Gurbani, V. K., de Haas, E., Haldeman, M., Harris, F. H., Hayes, J., Heckman, T. M., Hennessy, G. S., Hindsley, R. B., Holm, S., Holmgren, D. J., Huang, C.-h., Hull, C., Husby, D., Ichikawa, S.-I., Ichikawa, T., Ivezić, Ž., Kent, S., Kim, R. S. J., Kinney, E., Klaene, M., Kleinman, A. N., Kleinman, S., Knapp, G. R., Korienek, J., Kron, R. G., Kunszt, P. Z., Lamb, D. Q., Lee, B., Leger, R. F., Limmongkol, S., Lindenmeyer, C., Long, D. C., Loomis, C., Loveday, J., Lucinio, R., Lupton, R. H., MacKinnon, B., Mannery, E. J., Mantsch, P. M., Margon, B., McGehee, P., McKay, T. A., Meiksin, A., Merelli, A., Monet, D. G., Munn, J. A., Narayanan, V. K., Nash, T., Neilsen, E., Neswold, R., Newberg, H. J., Nichol, R. C., Nicinski, T., Nonino, M., Okada, N., Okamura, S., Ostriker, J. P., Owen, R., Pauls, A. G., Peoples, J., Peterson, R. L., Petravick, D., Pier, J. R., Pope, A., Pordes, R., Prosapio, A., Rechenmacher, R., Quinn, T. R., Richards, G. T., Richmond, M. W., Rivetta, C. H., Rockosi, C. M., Ruthmansdorfer, K., Sandford, D., Schlegel, D. J., Schneider, D. P., Sekiguchi, M., Sergey, G., Shimasaku, K., Siegmund, W. A., Smee, S., Smith, J. A., Snedden, S., Stone, R., Stoughton, C., Strauss, M. A., Stubbs, C., SubbaRao, M., Szalay, A. S., Szapudi, I., Szokoly, G. P., Thakar, A. R., Tremonti, C., Tucker, D. L., Uomoto, A., Vanden Berk, D., Vogeley, M. S., Waddell, P., Wang, S.-i., Watanabe, M., Weinberg, D. H., Yanny, B., & Yasuda, N. 2000, *AJ*, 120, 1579

TABLE 1
 SAMPLE PARAMETERS^a

ID	RA ^b (J2000)	Dec ^c (J2000)	z_{sys}	M_B	$U-B$	M_* (log M_\odot)	SFR ^d ($M_\odot \text{ yr}^{-1}$)	A_{UV} ^e	A_{74} ^f (kpc ²)	πR_P^2 ^g (kpc ²)	$V_1 \pm \delta V_1$ ^h (km s ⁻¹)
12008116	14 17 25.67	52 30 25.19	0.74664	-19.69	0.64	10.1	5	1.9	43	155	37 ± 31
12008166	14 17 21.59	52 28 03.62	1.28545	-19.69	0.32	9.7	...	0	11	44	31 ± 62
12008197	14 17 21.84	52 29 19.62	0.98022	-21.19	0.80	10.6	97	4.1	91	232	-62 ± 19
12008364 ⁱ	14 17 09.44	52 29 08.95	0.77957	-19.30	0.55	9.8	...	0	0	0	-33 ± 92
12008441	14 17 16.76	52 28 39.59	0.83273	-20.81	0.99	10.9	12	2.6	138	786	58 ± 61
12008445	14 17 04.91	52 27 48.85	1.27739	-20.69	0.51	10.2	...	0	77	220	-193 ± 79
12008456	14 17 10.67	52 30 11.63	0.90230	-19.93	0.73	9.8	6	1.4	21	60	79 ± 52
12008481	14 17 10.04	52 28 39.45	0.71341	-21.03	0.93	10.9	...	0	138	484	75 ± 109
12008509	14 17 03.23	52 30 33.13	1.21577	-19.80	0.36	9.7	...	0	51	144	70 ± 52
12008550	14 16 56.74	52 29 52.48	1.30249	-21.22	0.62	10.0	24	1.5	34	109	-145 ± 23
12008553	14 17 02.57	52 29 38.86	0.90156	-21.56	1.12	10.5	...	0	6	25	-79 ± 29
12008591	14 17 14.74	52 27 57.13	0.77192	-18.37	0.53	9.1	...	0	11	29	...
12008811	14 16 55.32	52 30 24.91	1.21556	-20.79	0.67	10.1	9	0.8	13	44	33 ± 20
12011364	14 18 28.46	52 33 16.22	0.98642	-20.75	0.74	10.2	90	4.2	90	244	-28 ± 24
12011428	14 18 28.35	52 31 47.76	1.28408	-19.87	0.18	9.6	9	0.8	154 ± 32
12011493	14 18 27.94	52 33 39.53	1.26377	-20.74	0.62	10.2	11	1	26	118	-21 ± 45
12011600	14 18 25.03	52 31 08.95	0.43665	-17.67	0.43	8.8	0	0.9	-133 ± 129
12011619	14 18 24.68	52 32 48.66	1.07449	-19.30	0.43	9.1	2	0	13	93	...
12011742	14 18 16.19	52 32 16.77	1.33578	-20.81	0.71	10.2	...	0	12	45	2 ± 23
12011767	14 18 24.75	52 32 55.43	1.28170	-22.18	0.75	11.0	76	2.7	171	562	-34 ± 35
12011836	14 18 16.05	52 31 48.06	0.92707	-19.90	0.57	10.2	14	2.8	14	55	-128 ± 21
12012500	14 17 21.28	52 34 01.05	0.86494	-20.28	0.89	10.6	...	0	34	95	-31 ± 28
12012764	14 17 03.83	52 33 00.36	1.23532	-20.26	0.61	9.7	...	0	-62 ± 47
12012777	14 17 03.22	52 31 42.52	1.27426	-21.06	0.51	10.1	22	1.4	15	55	-217 ± 13
12012817	14 16 59.78	52 31 09.48	1.21583	-20.92	0.89	10.8	...	0	7	23	28 ± 44
12012842	14 16 56.45	52 33 13.77	1.31484	-21.68	0.75	11.0	...	0	5 ± 23
12012871	14 17 00.37	52 33 38.53	1.34433	-20.75	0.55	10.0	14	1.3	-13 ± 39
12013002	14 16 50.03	52 33 46.59	1.21841	-20.22	0.64	9.5	4	0.3	10 ± 42
12013145	14 16 55.46	52 32 15.81	1.34063	-19.66	0.27	9.5	6	0.7	-38 ± 61
12013242	14 16 55.22	52 31 38.98	1.28679	-21.31	0.45	10.1	25	1.2	-73 ± 22
12015177	14 18 55.51	52 37 18.84	0.98609	-20.23	0.48	9.6	11	1.7	-101 ± 18
12015226	14 18 53.61	52 35 48.28	0.91600	-19.30	0.29	9.1	4	0.7	16 ± 18
12015295	14 18 55.92	52 37 07.05	0.49157	-19.52	0.81	10.4	1	1.2
12015313	14 18 50.39	52 36 21.36	0.68009	-20.72	1.21	11.2	...	0
12015320	14 18 51.69	52 36 00.43	0.98573	-22.09	1.05	11.3	40	2.6
12015563	14 18 34.29	52 36 49.30	1.28239	-21.30	0.59	10.3	...	0	7	22	-98 ± 42
12015643	14 18 49.35	52 36 08.38	0.24718	-17.97	0.51	9.3	0	1.6
12015680	14 18 42.71	52 36 35.96	0.75867	-20.47	0.55	10.3	21	2.9	68	279	148 ± 61
12015682	14 18 49.05	52 36 29.65	1.28371	-21.52	0.62	11.2	27	1.4	-99 ± 93
12015775	14 18 18.64	52 36 47.89	1.22428	-19.36	0.22	9.6	4	0.7	4	19	-105 ± 43
12015792 ⁱ	14 18 19.81	52 35 15.88	1.23068	-21.23	0.95	11.0	12	2.2	0	0	-27 ± 85
12015858	14 18 26.49	52 36 08.41	1.23068	-19.87	0.21	9.5	8	0.8	53	202	-54 ± 60
12015908	14 18 08.59	52 36 10.08	0.99924	-20.25	0.64	10.0	21	3	27	82	45 ± 23
12015914	14 18 22.10	52 35 27.04	1.10461	-19.82	0.33	10.1	8	1.1	3	10	51 ± 21
12015933	14 18 25.38	52 37 11.55	1.28514	-20.34	0.66	9.7	...	0	13	57	-22 ± 81
12016019	14 18 07.96	52 36 43.93	1.08467	-20.71	0.62	10.0	18	1.9	44	182	48 ± 14
12016050	14 18 08.67	52 35 13.82	0.97971	-19.71	0.44	9.5	15	2.6	11	48	-15 ± 22
12016054	14 18 06.66	52 35 06.05	0.68377	-20.73	1.08	11.2	16	4.1	43	134	72 ± 185
12016075	14 18 05.98	52 34 08.42	1.11739	-19.67	0.54	9.4	5	1.2	9	41	13 ± 49
12016337	14 18 03.71	52 34 23.42	0.72026	-20.27	1.01	10.9	9	3.3	144	617	...
12016903	14 17 12.78	52 34 28.40	1.15998	-21.46	0.50	10.2	25	1	46	202	2 ± 30
12017063	14 16 57.61	52 34 28.14	0.73912	-19.79	0.51	10.1	5	1.2	-70 ± 30
12019542	14 18 49.94	52 40 22.15	1.27848	-21.68	0.70	10.4	40	2.3	88	243	-183 ± 60
12019674	14 18 56.19	52 38 43.89	0.98491	-21.48	0.96	11.1	15	2.2	135	443	130 ± 86
12019697	14 18 49.69	52 37 42.18	0.26481	-17.25	0.54	9.0	0	1.8	27	111	...
12019709	14 18 47.13	52 37 52.21	0.75792	-19.90	0.48	9.7	...	0	10	23	-77 ± 151
12019916	14 18 36.51	52 40 20.89	0.72849	-20.26	0.83	10.7	11	3.3	48	156	49 ± 32
12019923	14 18 35.21	52 39 42.89	0.72674	-20.19	0.76	10.4	5	1.6	47	160	56 ± 37
12019962	14 18 36.59	52 37 43.63	0.64444	-19.22	0.45	9.7	1	0.8	32	144	104 ± 31
12019973	14 18 28.61	52 40 53.43	0.81886	-19.80	0.53	10.1	10	2.3	41	123	-58 ± 27
12019995	14 18 47.09	52 37 54.47	0.24888	-19.06	0.52	9.8	...	0	42	150	...
12019996	14 18 36.64	52 37 54.62	1.28128	-21.71	0.63	10.6	43	1.8	164	499	117 ± 24
12020031	14 18 41.23	52 39 34.32	0.82072	-22.00	0.97	11.2	36	2.4	427	1391	64 ± 108
12020064	14 18 46.56	52 38 13.78	1.31479	-21.12	0.59	10.3	26	2	58	138	-62 ± 56
12020075	14 18 48.94	52 37 30.01	0.80829	-20.52	0.64	10.6	12	1.9	77	279	-52 ± 17
12024014	14 18 50.28	52 42 05.78	1.29775	-20.51	0.49	9.9	...	0	6	17	...
12024045	14 18 51.65	52 40 56.08	0.24698	-18.91	0.61	9.9	5	4.5	61	424	...
12024133	14 18 51.82	52 41 11.85	1.12415	-21.14	0.81	10.5	36	3	49	202	-57 ± 43
12024181	14 18 49.60	52 42 36.79	1.08692	-21.00	0.80	10.5	35	3.3	96	479	-57 ± 32
12024409	14 18 33.91	52 41 28.32	1.03579	-20.59	0.84	9.9	11	1.7	48	138	-104 ± 42
12024524	14 18 33.28	52 41 10.89	0.90300	-20.93	0.71	10.4	32	2.7	119	393	-31 ± 23
12100420	14 16 57.97	52 31 58.63	1.19952	-20.63	0.60	10.0	9	1	3	10	71 ± 18

TABLE 1 — *Continued*

ID	RA ^b (J2000)	Dec ^c (J2000)	z_{sys}	M_B	$U-B$	M_* ($\log M_\odot$)	SFR ^d ($M_\odot \text{ yr}^{-1}$)	A_{UV} ^e	A_{74} ^f (kpc^2)	πR_P^2 ^g (kpc^2)	$V_1 \pm \delta V_1$ ^h (km s^{-1})
----	----------------------------	-----------------------------	-----------	-------	-------	-----------------------------	---	-----------------------	---	--	---

^a “...” indicates no data.

^b Units of right ascension are hours, minutes, and seconds.

^c Units of declination are degrees, arcminutes, and arcseconds.

^d Dust-corrected UV star-formation rate estimated from *GALEX* observations.

^e Dust attenuation estimated from UV colors.

^f Galaxy “clump area” (Section 3.2).

^g Galaxy Petrosian area.

^h V_1 outflow velocity measured from the simultaneous fit to five resonance Fe II absorption lines (Section 4.2).

ⁱ Objects with *HST* imaging, although the S/N was too low to make robust area measurements.

TABLE 2
CORRELATIONS BETWEEN V_1 OUTFLOW VELOCITY AND GALAXY PROPERTIES

Property	Correlation with V_1^a
SFR	1.2, -0.17 (47)
sSFR	2.3, -0.33 (47)
$\Sigma_{\text{SFR}}(\text{RP})$	2.4, -0.40 (36)
	3.1, -0.54 ^b (34)
$\Sigma_{\text{SFR}}(\text{A}_{74})$	2.4, -0.40 (36)
	3.1, -0.54 ^b (34)
i	0.9, -0.14 (46)
RP	-1.4, 0.20 (47)
$(\text{A}_{74}/\pi)^{1/2}$	-0.9, 0.14 (47)

^a The first number indicates the number of standard deviations from the null hypothesis that the quantities are uncorrelated, according to the Spearman ρ correlation test. A larger number of standard deviations means a higher likelihood that the data are correlated; negative values refer to inverse correlations. The second number is the correlation coefficient, r_S . The quantity in parentheses indicates the number of objects in the sample.

^b Correlations calculated omitting two outliers (12015914 and 12100420) whose extremely compact morphologies translated into large size uncertainties.

TABLE 3
COMPOSITE SPECTRA

Composite	Average Value	V_1^a (km s ⁻¹)	$V_{max}(\text{Mg II})^b$ (km s ⁻¹)	$V_{max}(\text{Fe II})^c$ (km s ⁻¹)
EGS	...	-5 ± 6	-730 ± 93	-564 ± 87
SFR - <i>high</i>	32 ± 4 M _⊙ yr ⁻¹	-24 ± 9	-748 ± 94	-514 ± 84
SFR - <i>low</i>	7 ± 1 M _⊙ yr ⁻¹	29 ± 11	-614 ± 83	-453 ± 104
sSFR - <i>high</i>	1.9 ± 0.2 × 10 ⁻⁹ yr ⁻¹	-34 ± 9	-605 ± 80	-556 ± 94
sSFR - <i>low</i>	4.1 ± 0.6 × 10 ⁻¹⁰ yr ⁻¹	27 ± 11	-834 ± 148	-456 ± 86
$\Sigma_{\text{SFR}}(\text{RP})$ - <i>high</i>	0.29 ± 0.05 M _⊙ yr ⁻¹ kpc ⁻²	-25 ± 6	-862 ± 69	-614 ± 97
$\Sigma_{\text{SFR}}(\text{RP})$ - <i>low</i>	0.05 ± 0.007 M _⊙ yr ⁻¹ kpc ⁻²	33 ± 13	-668 ± 105	-444 ± 87
$\Sigma_{\text{SFR}}(\text{A}_{74})$ - <i>high</i>	0.93 ± 0.15 M _⊙ yr ⁻¹ kpc ⁻²	-31 ± 7	-855 ± 66	-611 ± 103
$\Sigma_{\text{SFR}}(\text{A}_{74})$ - <i>low</i>	0.18 ± 0.02 M _⊙ yr ⁻¹ kpc ⁻²	44 ± 15	-640 ± 117	-451 ± 86
A_{UV} - <i>high</i>	2.7 ± 0.13	-3 ± 10	-732 ± 71	-497 ± 88
A_{UV} - <i>low</i>	1.1 ± 0.078	-10 ± 9	-652 ± 89	-522 ± 91
i - <i>high</i>	58° ± 1°	28 ± 11	-692 ± 95	-464 ± 77
i - <i>low</i>	38° ± 1°	-19 ± 9	-811 ± 140	-557 ± 101

^a Outflow velocity measured from the simultaneous fit to five resonance Fe II absorption lines, as described in Section 4.2 and Martin et al. (2012).

^b Maximal outflow velocity measured from the 2796 Å Mg II line (Section 5.3).

^c Maximal outflow velocity measured from the 2374 Å Fe II line (Section 5.3).